12 Die Forming

Dies, as used in polymer processing, are metal flow channels or restrictions that serve the purpose of imparting a specific *cross-sectional shape* to a stream of polymer melt that flows through them. They are primarily used in the extrusion process to *continuously* form polymer products such as tubes, films, sheets, fibers, and ''profiles'' of complex cross-sectional shapes. Dies are positioned at the exit end of the melt-generating or -conveying equipment and, generally speaking, consist of three functional and geometrical regions:

1. The *die manifold*, which serves to distribute the incoming polymer melt stream over a cross-sectional area similar to that of the final product but different from that of the exit of the melt conveying equipment.
2. The *approach channel*, which streamlines the melt into the final die opening.
3. The die *lip*, or final die opening area, which is designed to give the proper cross-sectional shape to the product and to allow the melt to ''forget'' the generally nonuniform flow experience in regions 1 and 2.

Figure 12.1 shows these regions schematically for a sheet-forming die. The shape of both the manifold and approach channels may vary in the cross-die *x* direction, to permit achievement of the design goals just outlined, that is, melt distribution and delivery to the die lips area at uniform pressure. Minor adjustments of the die-lip opening are often required to correct for temperature gradients along the die, as well as bending of the die under the applied pressure.

The engineering objectives of die design are to achieve the desired shape within set limits of dimensional *uniformity* and at the *highest* possible *production rate*. This chapter discusses both objectives, but the question of die-formed product uniformity deserves immediate amplification. To understand the problem, we must distinguish between two types of die-formed product nonuniformity: (a) nonuniformity of product in the machine direction, direction *z* [Fig. 12.2(a)], and (b) nonuniformity of product in the cross-machine direction, direction *x* [Fig. 12.2(b)]. These dimensional nonuniformities generally originate from entirely different sources. The main source of the former is the variation
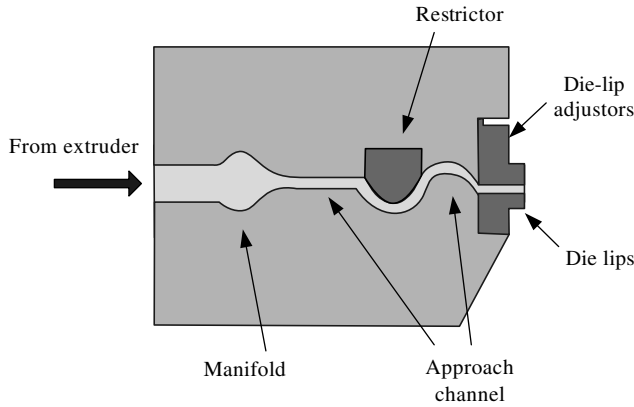
Fig. 12.1 Schematic representation of a sheet die, including manifold, approach channel, and die lip regions. The restrictor bar is incorporated so that the die can be used with different polymers of varying viscosities.

over time of the inlet stream temperature, pressure, and composition (when mixtures are extruded through the die). The latter is generally due to improper die design. From the discussion on residence time distribution (RTD) in Chapter 7 it is evident that the capability of eliminating inlet concentration variations depends on the RTD function. A
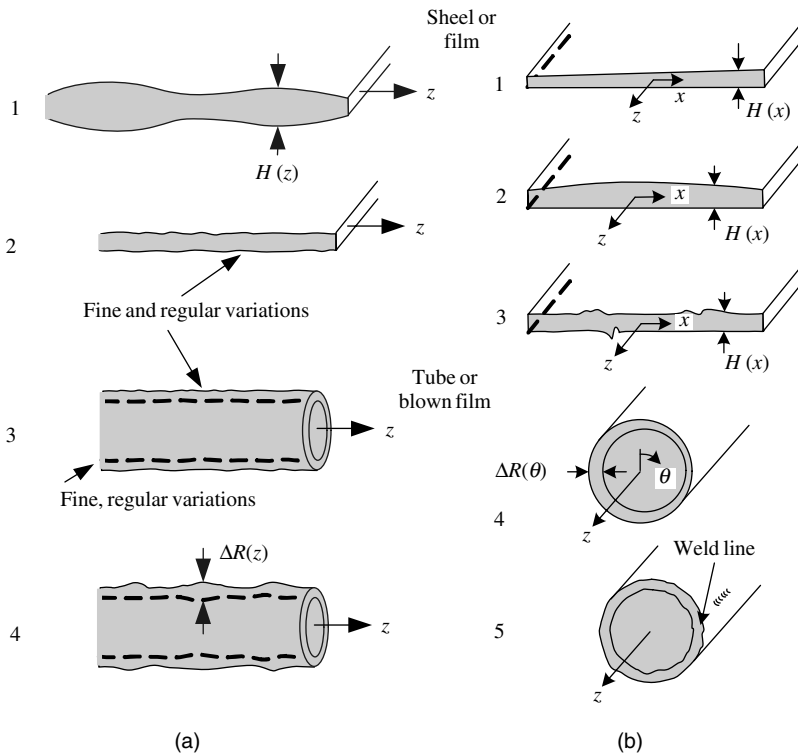

Fig. 12.2 Die-formed product nonuniformities in (a) the machine direction, and (b) the cross-machine direction.

step change in inlet concentration in the plug-flow system will be reflected unchanged at the exit. Back-mixing will reduce outlet concentration variation. Therefore, narrow RTD functions, as in pressure-type flow dies, cannot be expected to eliminate concentration or temperature variation by mixing. Hence, we must ensure adequate inlet uniformity in time, of both temperature and pressure. These depend on the melt generating and conveying equipment preceding the die. In terms of the extrusion operation, improper solids conveying, solid bed breakup, incomplete melting, inefficient mixing due to deep metering channels (all for set extrusion conditions), or the absence of a mixing or barrier device, may result in a *time variation* of the pressure and temperature of the melt being delivered to the die; this will certainly cause machine direction non-uniformities. Figure 12.3 gives examples of acceptable and unacceptable temperature and die inlet pressure variations for a melt stream of low density polyethlene (LDPE). The level of variations that can be tolerated depends on both the product specifications and the temperature sensitivity of the viscous and elastic responses of the melt.

It is also worth noting in Fig. 12.3 that the two engineering objectives of die forming—namely, uniformity of product and maximum throughput rate—are competing ones. That is, a high throughput rate can be achieved at the expense, in general, of machine direction product uniformity, at set processing conditions. Additionally, there exists an intrinsic upper limit in the throughput rate set by the phenomenon of melt fracture, observed with all polymer melts and discussed in Section 12.2.

Machine direction product nonuniformities always accompany melt fracture, and this is why the phenomenon marks the throughput upper limit to die forming. These nonuniformities can be intense or mild, depending on the die *streamlining*, but they are always high frequency disturbances in the product thickness. Other causes for machine
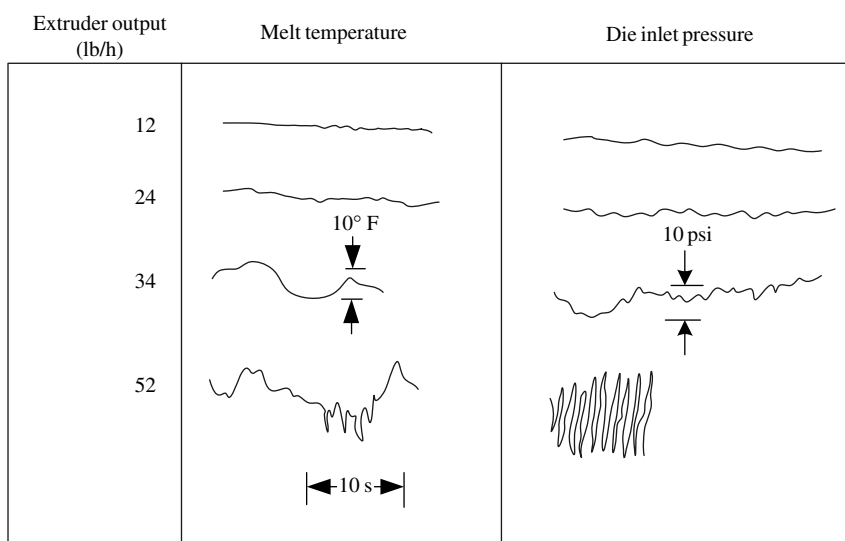

Fig. 12.3   Types of actual melt temperature and die inlet pressure variations obtained with LDPE. The last two would result in product nonuniformities in the machine direction. [Reprinted by permission from H. B. Kessler, R. M. Bonner, P. H. Squires, and C. F. Wolf, *Soc. Plast. Eng. J.*, **16**, 267 (1960).]

direction nonuniformities can be found in the die design that creates stagnation areas where the melt gets trapped and periodically surges forward, and in the post–die forming, cooling, and stretching operations, which may vary with time or may be subject to periodic instabilities.

Product nonuniformities in the cross-machine direction are, as just pointed out, due to *poor die design* or are intrinsic to particular types of dies. Any number of die-related causes can be responsible for the types of nonuniformities in Fig. 12.2(b): inappropriate design of any one of the three die regions [Fig. 12.2(b) 1–4], inadequate temperature control of the die walls [Fig. 12.2(b), 1, 2, 4]; bending of the die walls by the flow pressure [Fig. 12.2(b), 2], and finally the presence of obstacles in the flow channels for die-support purposes [Fig. 12.2(b), 5].

In principle, all types of cross-machine direction nonuniformities can be remedied by proper die design, which can be achieved in part through the development of *die design equations*, which form the mathematical model of the die flow. This chapter discusses the origin, form, and limitations of such models as they apply to dies of various types.

Before getting to that, however, we examine in detail the flow of polymer melts in capillaries. There are two reasons for revisiting capillary flow, after having discussed it in Chapter 3. First, capillary flow is characterized by all the essential problems found in any die forming flow: flow in the entrance, fully developed, and exit regions; therefore, the conclusions reached from the study of capillary flow can, and will be, generalized for all pressure flows. Second, capillary flow has been more widely studied by both rheologists and engineers than any other flow configuration. We pay particular attention to the problems of entrance pressure drop, viscous heat generation, extrudate swelling, and extrudate melt fracture.

Finally, in discussing die flow models, we take into account the results presented in connection with capillary flow, but we also look at the details of the flow in each particular die. Die flow models should provide quantitative answers to questions of the following type: (a) if a tube of given dimensions, uniform in the cross-machine direction, is to be extruded at a given rate and with a specific polymer, what should the die design (or designs) be, and what would the resulting pressure drop be? (b) How do the design and pressure drop depend on the processing variables and melt rheology?

12.1   CAPILLARY FLOW

Figure 12.4 depicts schematically the experimental setup used in capillary flow studies. The primary application of the discussion that follows is in capillary viscometry, which is useful to die design. The ratio R_r/R should be greater than 10, so that the pressure drop due to the flow in the reservoir can be neglected.[1] The reservoir radius cannot be too large, though, because the time required for uniform heating of the solid polymer load would be too long (see Fig. 5.6). Long heating cannot be used for sensitive polymers such as polyvinyl chloride (PVC), which readily degrade thermally.

It is useful at this point to consider the ''polymer melt experience'' as it flows from the reservoir into, through, and out of the capillary tube. In the entrance region shown in

---

1. In careful viscometric studies, this pressure drop is never neglected; the pressure reading at zero reservoir height, as found by extrapolation, is used for the value of P_0.
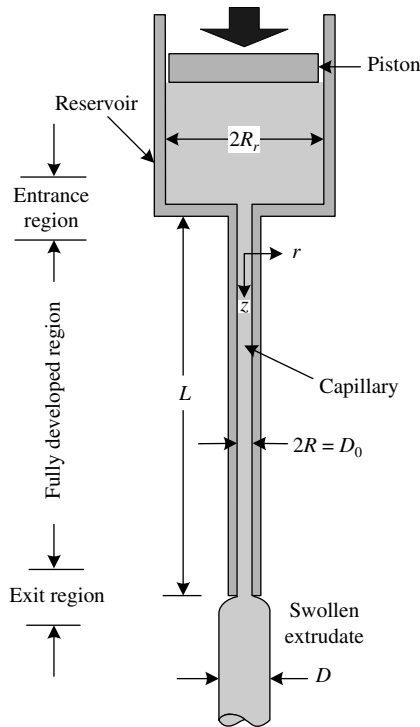
Fig. 12.4 Experimental setup for capillary flow showing reservoir, entrance, fully developed, and exit regions.

Fig. 12.4, the melt is forced into a converging flow pattern and undergoes a large axial acceleration, that is, it stretches. As the flow rate is increased, the axial acceleration also increases, and as a result the polymer melt exhibits stronger elastic response, with the possibility of rupturing, much like "silly putty" would, when stretched fast. Barring any such instability phenomena, a fully developed velocity profile is reached a few diameters after the geometrical entrance to the capillary.

The flow in the capillary, which for pseudoplastic fluids is characterized by a rather "flat" velocity profile, imparts a shear strain on the melt near the capillary walls. The core of the melt, if the capillary L/R is large and the flow rate is small, can undergo a partial strain recovery process *during* its residence in the capillary. At the exit region, the melt finds itself under the influence of no externally applied stresses. It can thus undergo delayed strain recovery, which, together with the velocity profile rearrangement to one that is pluglike in the exit region, results in the phenomenon of extrudate swelling.

The "polymer melt experience" briefly described above is complex and varied; it involves steady, accelerating, fully developed, and exit flows and strain recovery. It is not surprising, then, that this apparently simple experiment is used to study not only the viscous but also the elastic nature of polymer melts.

Entrance and Exit Capillary Pressure Losses; the Bagley Correction

In the fully developed flow region, the assumptions of steady and isothermal flow, constant fluid density, and independence of the pressure from the radius, resulted in the conclusion
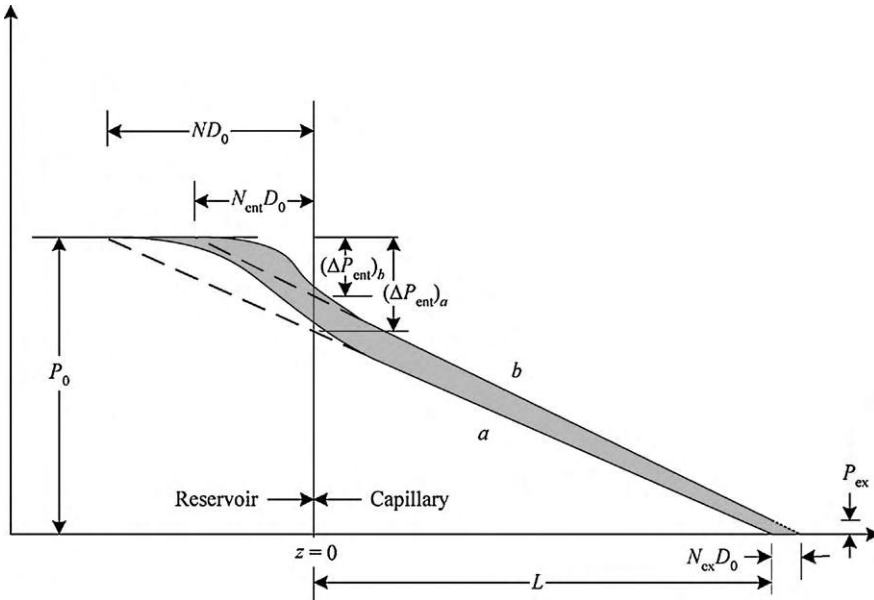
Fig. 12.5 Schematic representation of the capillary pressure along its axis: Curve a, without P_{ex}; Curve b, in the presence of P_{ex}.

that $-dP/dz = \Delta P/L$. This conclusion is obviously not correct near the capillary entrance where, because of the converging flow, extra velocities (v_r) and velocity gradients (dv_z/dz, dv_r/dr, etc.) are present. Although the flow pattern is not known precisely, we know that a higher pressure drop is needed to support the additional velocity gradients for any viscous or viscoelastic fluid. Schematically, then, the pressure profile can be represented as in Fig. 12.5 (Curve a). Thus, $-dP/dz = \Delta P/L^* = \Delta P/(L + ND_0)$, where $N > 0$ is the entrance loss correction factor that must be evaluated experimentally. The entrance, or Bagley correction (1), N must be considered in the calculation of the shear stress at the wall

$$\tau_w^* = \frac{(P_0 - P_L)D_0}{4L^*} = \frac{D_0}{4}\left(\frac{\Delta P}{L + ND_0}\right) \tag{12.1-1}$$

where τ_w^* is the corrected shear stress at the wall for fully developed flow. The stress at the capillary wall is given by

$$\tau_w^* = -\eta\dot{\gamma}_{12}(R) = \eta\dot{\gamma}_w^* \tag{12.1-2}$$

From the Rabinowitsch equation E3.1-10, $\dot{\gamma}_w^*$ is given by

$$\dot{\gamma}_w^* = \frac{3}{4}\Gamma + \frac{\tau_w^*}{4}\frac{d\Gamma}{d\tau_w^*} \tag{12.1-3}$$

where $\Gamma = 32Q/\pi D_0^3$. Combining the equations for $\dot{\gamma}_w^*$ and τ_w^*, we see that $\tau_w^* = g(\Gamma)$.
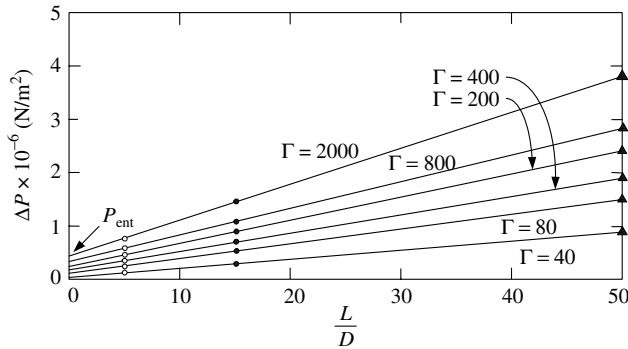
Fig. 12.6 Bagley plots for a polystyrene (PS) melt at 200°C, from which $N(\Gamma)$ can be evaluated; ΔP at $L/D_0 \to 0$ is the entrance pressure drop ΔP. [Reprinted by permission from J. L. White, *Appl. Polym. Symp.*, No. 20, 155 (1973).]

Equation 12.1-1 can be rearranged as follows:

$$\frac{L}{D_0} = -N + \frac{\Delta P}{4g(\Gamma)} \tag{12.1-4}$$

where $g(\Gamma)$ is a function of the Newtonian shear rate at the wall. Equation 12.1-4 forms the basis of the so-called Bagley plots (1) (Fig. 12.6) through which $N(\Gamma)$ is evaluated graphically and the corrected wall shear stresses are determined using Eq. 12.1-1. Experimental evidence indicates that the P versus L/D_0 curves at constant Γ are not straight, but curve upward at high L/D_0 values. This phenomenon has been attributed in the literature both to the relaxation of normal stresses (2), and probably, to a large extent, to the effect of the hydrostatic pressure on melt viscosity (3–5), which can be expressed as

$$\mu(P) = \mu(P_0) \exp[\beta(P - P_0)] \tag{12.1-5}$$

where β is related to polymer melt compressibility and is of the order of 5×10^{-9} $(N/m^2)^{-1}$. It should be emphasized that, although the preceding treatment may give better values for the fully developed region, the same is not true for its entrance region, where the actual τ_w^* values are large. Despite the previously mentioned experimental facts, the Bagley correction $N(\Gamma)$ is *functionally useful* in that it eliminates the effect of L/D_0 from the capillary flow curves. Problem 12.1(b) indicates the error involved in neglecting ΔP_{ent} with various L/D_0 capillaries.

Also worth noting in connection with the foregoing discussion is the experimental observation of a nonzero gauge pressure at the capillary exit P_{ex} (Curve *b* of Fig. 12.5). Thus one must take into consideration end corrections, both entrance and exit, and not only entrance corrections alone, as was done by Bagley. Sakiades (6) was the first to report the existence of P_{ex} for polymer solutions, and Han and his co-workers have studied it extensively using polymer melts (7–9). It has been found that $P_{ex}/\Delta P_{ent}$ is between 0.15 and 0.20, and that, although ΔP_{ent} does not depend on L/D_0, P_{ex} decreases up to $L/D_0 = 10$, then remains constant (9).

With these observations in mind (see Curve b, Fig. 12.5), we can rewrite Eq. 12.1-1

$$\tau_w^* = \frac{\Delta P D_0}{4L^*} = \frac{D_0}{4}\left(\frac{\Delta P}{L + N_{ent}D_0 + N_{ex}D_0}\right) \tag{12.1-6}$$

where N_{ent} is the entrance capillary length correction and N_{ex} the exit capillary length correction. If $(P_{ex}/\Delta P_{ent}) \ll 1$, then $N = N_{ent}$; if P_{ex} is included, it is found that $N_{ent} < N$. Problem 12.2 indicates that, for high density polyethlene (HDPE) the data improvements obtained with the inclusion of P_{ex} are slight; ΔP_e is the sum of P_{ex} and ΔP_{ent}.[2]

Viscous Heat Generation

One of the assumptions made in solving the flow in the fully developed region of the capillary was that of constant fluid temperature throughout the flow region. This is not a valid assumption for the flow of very viscous fluids at high rates of shear in which a nonuniform temperature field is created. As we have already mentioned in connection with the thermal-energy balance (Section 2.2), the rate of viscous heating per unit volume e_v is

$$e_v = -(\boldsymbol{\tau} : \nabla\mathbf{v}) = -\frac{1}{2}(\boldsymbol{\tau} : \dot{\boldsymbol{\gamma}} + \boldsymbol{\tau} : \boldsymbol{\omega}) \tag{12.1-7}$$

with $\boldsymbol{\tau} : \boldsymbol{\omega} = 0$ as a scalar product of a symmetric and antisymmetric matrix. Thus, for a Newtonian fluid

$$e_{v,N} = \frac{\mu}{2}\dot{\boldsymbol{\gamma}} : \dot{\boldsymbol{\gamma}} \equiv \mu\Phi_v \tag{12.1-8}$$

while for a Power Law fluid

$$e_{v,PL} = \frac{m}{2}\left[\sqrt{\frac{1}{2}(\dot{\boldsymbol{\gamma}} : \dot{\boldsymbol{\gamma}})}\right]^{n-1}(\dot{\boldsymbol{\gamma}} : \dot{\boldsymbol{\gamma}}) \equiv m\Phi_v^{(n+1)/2} \tag{12.1-9}$$

In the fully developed region of the capillary, the flow is described by

$$\dot{\boldsymbol{\gamma}} = \begin{pmatrix} 0 & 0 & \dfrac{dv_z}{dr} \\ 0 & 0 & 0 \\ \dfrac{dv_z}{dr} & 0 & 0 \end{pmatrix} \tag{12.1-10}$$

2. The Rosand Viscometer [Malvern Instruments Ltd., Enigma Business Park, United Kingdom] consists of two identical parallel barrels and two equal-length plungers that are driven by the same constant velocity drive. Each of the plungers has its own pressure transducers. One of the barrels is fitted with a zero-length (knife-edge) capillary and the other with one of $10 < L/D < 20$. When all the melt has been emptied from the barrel, the pressure registered by the plunger with the knife-edge capillary, represents a direct experimental value of ΔP_{ent}.

Thus, Eqs. 12.1-8 and 12.1-9 become, respectively,

$$e_{v,\text{N}} = \mu \left(\frac{dv_z}{dr} \right)^2 \tag{12.1-11}$$

$$e_{v,\text{PL}} = m \left[\left(\frac{dv_z}{dr} \right)^2 \right]^{(n+1)/2} \tag{12.1-12}$$

where

$$\mu = \mu_0 e^{\Delta E/RT} \tag{12.1-13}$$

and

$$m = m_0 e^{\Delta E/RT} \tag{12.1-14}$$

Figure 12.7 gives the velocity gradients of a Newtonian and a Power Law fluid with $\mu = m$; isothermal flow is assumed. It is clear that, for Power Law fluids, viscous heating may be intense near the capillary wall, whereas the central portion of the fluid is relatively free of this effect.

The mathematical solution of the nonisothermal flow problem in the fully developed region of the capillary, even with the simplifying assumption of constant fluid density, involves the simultaneous solution of the momentum and energy balances, which have the general forms discussed in Section 2.2, subject to the appropriate boundary conditions. The two equations must be solved simultaneously, because they are coupled through the temperature-dependent viscosity (Eq. 12.1-13). Nahme (10) was the first investigator to look into this coupled-transport problem. Brinkman (11) made the first significant contributions to the understanding of the problem (the Brinkman number), although his solution is limited by the assumption of constant viscosity.

The problem of viscous heat generation of a Newtonian fluid with temperature-dependent transport properties was solved by Turian and Bird (12), and the first numerical solution is credited to Gerrard, Steidler, and Appeldoorn (13). Using a perturbation procedure, Turian solved the problem of a Power Law fluid with temperature-dependent viscosity and conductivity, flowing in Couette and cone and plate flows (14). Morrette and Gogos (15), using a numerical solution, examined the flow of PVC compounds that are subject to thermal degradation, and viscosity changes because of it. For this system, the coupled momentum and energy balances are

$$-\frac{dP}{dz} + \frac{1}{r} \frac{d}{dr} \left[r m_0 e^{\Delta E/RT} \left| \frac{dv_z}{dr} \right|^{n-1} \frac{dv_z}{dr} \right] = 0 \tag{12.1-15}$$

$$\rho C_p v_z \frac{dT}{dz} = \frac{1}{r} \frac{\partial}{\partial r} \left(r k \frac{\partial T}{\partial r} \right) + m_0 e^{\Delta E/RT} \left| \frac{dv_z}{dr} \right|^{n-1} \left(\frac{dv_z}{dr} \right)^2 \tag{12.1-16}$$

Results obtained by the latter investigators indeed show what is expected from Eqs. 12.1-15 and 12.1-16: temperature rises are intense and significant for the layer of the PVC melt near the capillary wall, where $e_{v,\text{PL}}$ has high values. As Fig. 12.8 indicates,
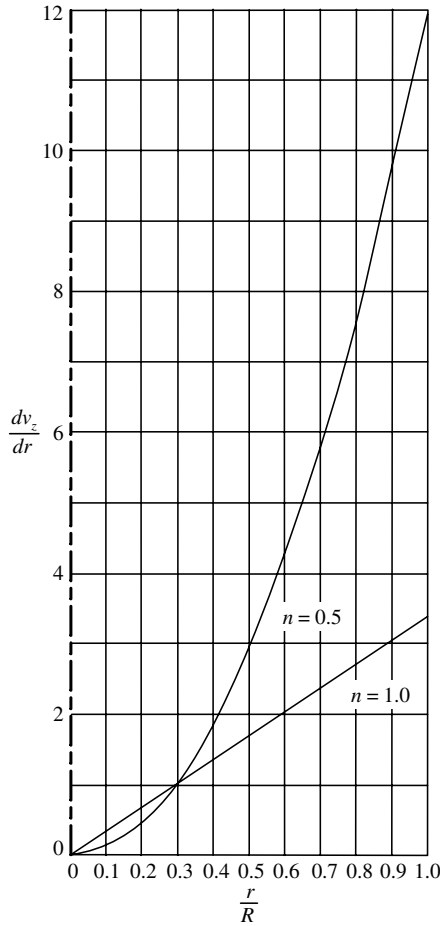
Fig. 12.7   Velocity gradients in a capillary for incompressible Newtonian and Power Law fluids: $\mu = m = 10^5$ N $\cdot$ s/m^2; $\Delta P = 5000$ psi $= 3.45 \times 10^7$ N/m^2; $R = 0.1$ cm; $L = 5$ cm.

about 50 % of the temperature rise occurs in the first tenth of the capillary length when m has a high value, since the temperature of the entering melt is low. Two cases were considered, those of isothermal and adiabatic capillary walls, because actual flows lie between these two extremes.

A good experimental method has yet to be devised to measure the temperature of highly viscous fluids flowing at high flow rates. Thermocouple measurements (16–18) have not been successful because they disrupt the flow field and become heated by the viscous fluid flowing past their surface.

Cox and Macosko (19) have reported experimental results on measurements of the melt-surface temperature upon exit from the capillary using infrared pyrometry, which senses the radiation emitted by the hot polymer melt surface. Their work also included the numerical simulation of viscous heating in a capillary, a slit, and an annular die, using a method resembling that of Gerrard et al. (13). They used a boundary condition at the die wall in between the isothermal and adiabatic case, $-k(\partial T/\partial r) = h(T - T_0)$ at the wall, where T_0 is the die temperature "far" from the melt–die interface as well as the inlet melt
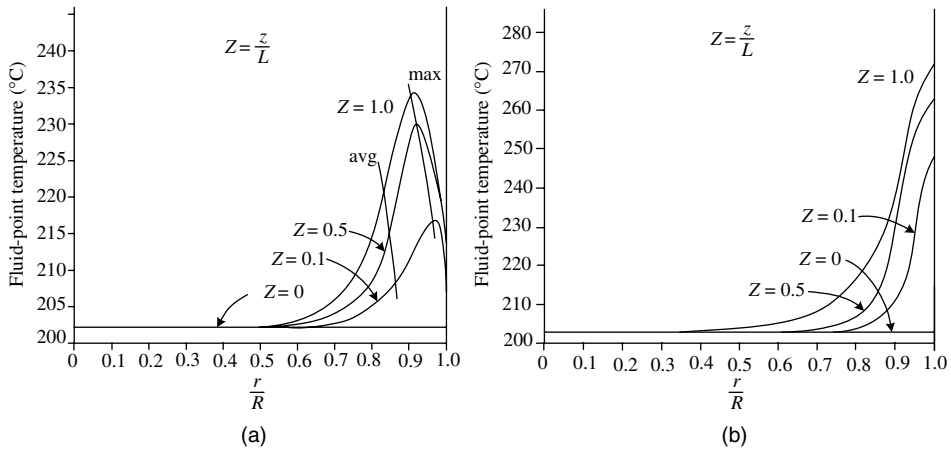
Fig. 12.8 Computed temperature profiles for a PVC melt. (a) Isothermal capillary wall. (b) Adiabatic wall. [Reprinted by permission from R. A. Morrette and C. G. Gogos, "Viscous Dissipation in Capillary Fow of Rigid PVC and PVC Degradation," *Polym. Eng. Sci.*, **8**, 272 (1968).]

temperature. Some of their results for ABS Cycolac T appear in Figs. 12.9–12.11. The data and numerical results depicted in these figures suggest the following:

1. Large temperature rises due to viscous heating do indeed occur in melt capillary flow at moderate and high shear rates. These must be estimated and taken into account whenever temperature sensitive polymers are extruded and whenever the extrudate surface quality and extrudate properties are of critical importance.
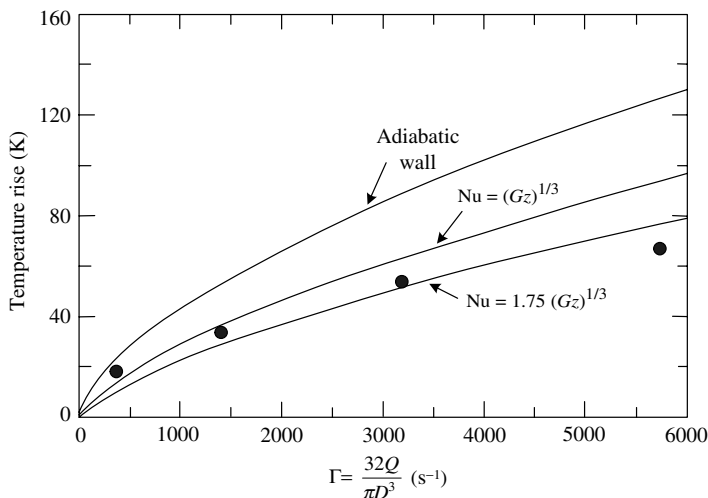

Fig. 12.9 Melt surface temperature rise at the capillary exit, calculated for ABS Cycolac T and measured (●) with an infrared pyrometer: $T_0 = 505\,\text{K}$, $D_0 = 0.319\,\text{cm}$, $L/D_0 = 30$. The relationships $\text{Nu} = C(G_z)^{1/3}$ are used to estimate h. [Reprinted by permission from H. W. Cox and C. W. Macosko, "Viscous Dissipation in Die Flow," *AIChE J.*, **20**, 785 (1974).]
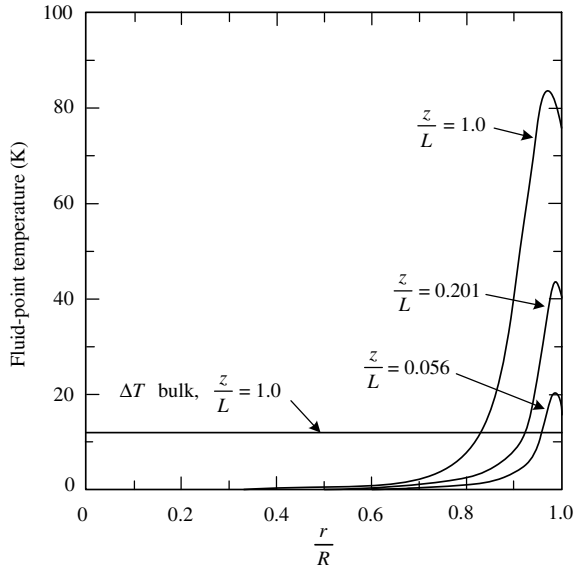
Fig. 12.10 Temperature profiles (calculated) for ABS Cycolac T in tube flow using $Nu = 1.75(Gz)^{1/3}$ to estimate h; $D_0 = 0.319$ cm; $L/D_0 = 30$; $T_0 = 505$ K; $\Gamma = 5730$ s^{-1}. [Reprinted by permission from H. W. Cox and C. W. Macosko, "Viscous Dissipation in Die Flow," *AIChE J.*, **20**, 785 (1974).]

2. At least as far as estimating the surface-temperature rise, the simple dimensionless relationship concerning heat transfer at the wall suffices:

$$Nu = C(Gz)^{1/3} \qquad (12.1\text{-}17)$$

where $Nu = hD_0/k$, $G_z = \dot{m}C_p/kL$, $\dot{m}$ is the mass flow rate, and $C = 1.75$ for satisfactory fit with the data. The temperature at the capillary wall is never the
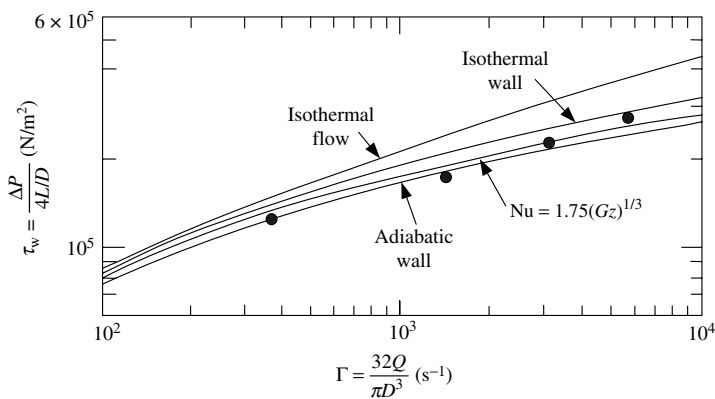

Fig. 12.11 Uncorrected shear stress versus Newtonian wall shear rate for ABS Cycolac T; measured and calculated using various thermal boundary conditions. $D_0 = 0.319$ cm; $L/D_0 = 30$; $T_0 = 505$ K. [Reprinted by permission from H. W. Cox and C. W. Macosko, "Viscous Dissipation in Die Flow," *AIChE J.*, **20**, 785 (1974).]

maximum; this occurs at about 9/10 the capillary radius. The temperature field at the exit, $T(r, L)$ will influence the swelling and drawing behavior of the extrudate.

3. About 50 % of the temperature rise occurs near the capillary entrance, $z \leq 0.2L$. Thus, shortening the capillary length does not decrease the temperature rise due to viscous heating, proportionally.

4. The bulk temperature rise, ΔT_b (Fig.12.10), does not seem to serve any useful purpose in that it is much smaller than the maximum and is heavily influenced by the central core of the fluid, which does not significantly heat up; ΔT_b is a quantity often calculated and presented as the reason for not having to worry about viscous heating. A simple estimate of ΔT_b is obtained by assuming that the entire mechanical energy degenerates to heating the melt. It seems, therefore, that one must consider and deal with the nonisothermal nature of any type of pressure flow when the calculated value of ΔT_b exceeds 4–5 °C.

Galili and Takserman-Krozer (20) have proposed a simple criterion that signifies when nonisothermal effects must be taken into account. The criterion is based on a perturbation solution of the coupled heat transfer and pressure flow isothermal wall problem of an incompressible Newtonian fluid.

The pressure drop calculated assuming the relationship $\mathrm{Nu} = 1.75(Gz)^{1/3}$ for estimating h is smaller than the calculated ΔP, assuming isothermal flow. For the conditions depicted in Fig. 12.11, at $\Gamma = 10^3 \, \mathrm{s}^{-1}$ the isothermal pressure drop is about 30 % higher than the measured value. This fact must be taken into account in the design of extrusion dies, so that gross die overdesign can be avoided, as well as in capillary viscometry.

12.2   ELASTIC EFFECTS IN CAPILLARY FLOWS

So far in this chapter we have looked into the viscous phenomena associated with the flow of polymer melts in capillaries. We now turn to the phenomena that are related to melt elasticity, namely: (a) swelling of polymer melt extrudates; (b) large pressure drops at the capillary entrance, compared to those encountered in the flow of Newtonian fluids; and (c) capillary flow instabilities accompanied by extrudate defects, commonly referred to as "melt fracture."

These phenomena have been the subject of intensive study during the last 50 years and still represent major problems in polymer rheology. From a processing point of view they are very important, since melt fracture represents an upper limit to the rate of extrusion, and swelling and the large pressure drops must be accounted for in product considerations and in the design of the die and processing equipment.

Extrudate Swelling

Extrudate swelling refers to the phenomenon observed with polymer melts and solutions that, when extruded, emerge with cross-sectional dimensions appreciably larger than those of the flow conduit. The ratio of the final jet diameter to that of the capillary D/D_0, for Newtonian fluids varies only from 1.12 at low shear rates to 0.87 at high rates. Polymer
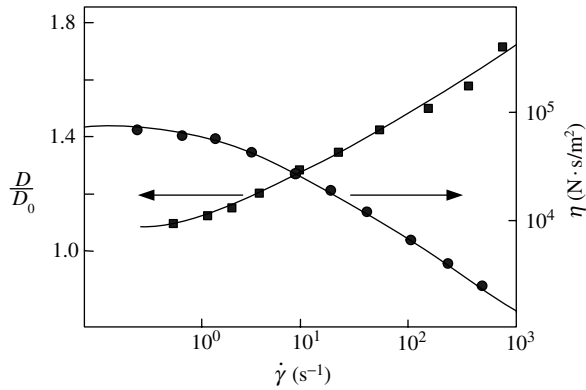
Fig. 12.12 Comparison of the viscosity and swelling ratio dependence on shear rate for a polystyrene melt of $\bar{M}_w = 2.2 \times 10^5$ and $\bar{M}_w/\bar{M}_n = 3.1$. [Reprinted by permission from W. W. Graessley, S. D. Glasscock, and R. L. Crawley, "Die Swell in Molten Polymers," *Trans. Soc. Rheol.*, **14**, 519 (1970).]

melts exhibit the same low shear rate D/D_0 value in the Newtonian plateau region, but swell 2–4 times the extrudate diameter at higher shear rates (21,22). Figure 12.12 gives the shear-rate dependent D/D_0 for melts, together with $\eta(\dot{\gamma})$. Extrudate swelling increases are accompanied by $\eta(\dot{\gamma})$ decreases.

Experimentally, as indicated in Fig. 12.13, we find that D/D_0 depends on the shear stress at the wall τ_w (a flow variable) and the molecular weight distribution (MWD) (a structural variable) (22). The length-to-diameter ratio of the capillary (a geometric variable) also influences D/D_0. The swelling ratio at constant τ_w decreases exponentially with increasing L/D_0 and becomes constant for $L/D_0 > 30$. The reason for this decrease can be explained qualitatively as follows. Extrudate swelling is related to the ability of polymer melts and solutions to undergo delayed elastic strain recovery, as discussed in
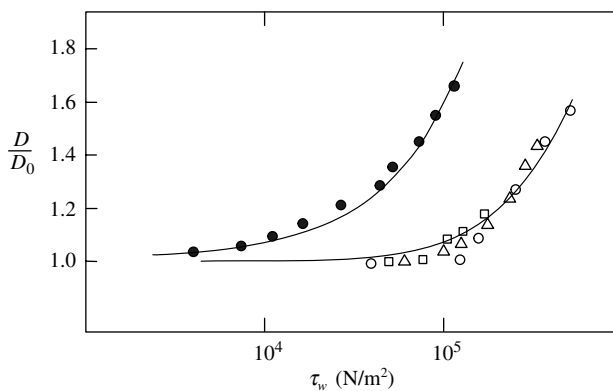

Fig. 12.13 Extrudate swelling data for polystyrene melts: ●, broad molecular weight sample; ○, □, △, narrow distribution sample data at various temperatures. [Reprinted by permission from W. W. Graessley, S. D. Glasscock, and R. L. Crawley, "Die Swell in Molten Polymers," *Trans. Soc. Rheol.*, **14**, 519 (1970).]

Section 3.1. The more strained and the more entangled the melt is at the capillary exit, the more it will swell.[3]

From this point of view, the decrease of swelling with increasing L/D_0 is due to two causes. First, along the capillary, the melt recovers from the tensile deformations suffered at the capillary inlet, which is due to the axial acceleration in that region. Second, the shear strain imposed on the melt while in the capillary may bring about disentanglements. Polymer melts and solutions are entangled and, under quiescent conditions, are characterized by a high entanglement density value. In this sense they possess a "structure." During shear flow, the entanglement density is reduced, and so is the ability of the fluid to undergo strain recovery. Thus the value of D/D_0 at very long L/D_0 values reflects the ability of the viscoelastic liquid to recover from shear strains only. The melt exiting from a very short capillary is much more entangled and recovers better from both shear and tensile strains.

In view of the foregoing discussion, it is not surprising that the magnitude of the first normal stress difference, which measures the extra tension in the flow direction during the flow in a long capillary, reflects the magnitude of extrudate swelling. Such a relationship has indeed been suggested by Tanner (23), who applied Lodge's theory of free recovery following steady shearing flows (24). For long capillaries, Tanner obtains

$$\frac{D}{D_0} = 0.1 + (1 + S_R^2)^{1/6} \tag{12.2-1}$$

The constant 0.1 is empirical; S_R, the recoverable shear strain, is

$$S_R = \frac{\tau_{11} - \tau_{22}}{2\tau_{12}} = \frac{\Psi_1 \dot{\gamma}_w}{2\eta} \tag{12.2-2}$$

where the stresses are evaluated at the wall shear rate $\dot{\gamma}_w$. The shear stress and normal stress differences can be measured experimentally or they can be calculated with the aid of indirect experimental measurements and either continuum or molecular theories. For example, Tanner used the Bernstein–Kearsler–Zappas (BKZ) theory and Bird et al. (25) the Goddard–Miller theory. When the Rouse molecular theory is used, the steady-state shear compliance J_R is (26)

$$J_R = 0.4 \frac{\bar{M}_w}{\rho RT} \cdot \frac{\bar{M}_z \bar{M}_{z+1}}{\bar{M}_w^2} \tag{12.2-3a}$$

for PS, Graessley et al. (22) found

$$J_0 = \frac{2.2 J_R}{1 + 2.1 \times 10^{-5} \rho \bar{M}_w} = \frac{S_R}{\tau_w^*} \tag{12.2-3b}$$

---

3. Solutions of rigid polymer molecules (e.g., poly-*p*-phenylene terephthalate) may also exhibit extrudate swelling because they too are *entropy elastic*: molecules exit the capillary in a fairly oriented state and become randomly oriented downstream.

where ρ is in g/cm^3. Thus, for high $\bar{M}_w$

$$J_0 = \frac{0.4 \times 10^5}{\rho^2 RT} \cdot \frac{\bar{M}_z \bar{M}_{z+1}}{\bar{M}_w^2} \qquad (12.2\text{-}3c)$$

These relationships indicate that S_R and, according to Eq.12.2-1, D/D_0, depend on the MWD. We recall that this was also observed by Graessley.

Equation 12.2-1 has been semiquantitatively successful in predicting extrudate swelling (25). However, White and Roman (27) have shown experimentally with a number of polymers that D/D_0 is not a function of S_R only. Furthermore, they demonstrated that the success of the Tanner equation depends on the method of measurement of D/D_0.

As Fig.12.14 reveals, extrudate swelling values can differ by as much as 30 %, depending on the measurement method. The Tanner equation compares best with the results obtained on extrudates frozen in air. The work of White and Roman is important to processing because, in such operations, extrudate swelling occurs under postextrusion conditions that are poorly specified and always nonequilibrium. The solution of the extrudate swelling problem can, in principle, be found by using macroscopic mass and momentum balances over a control volume bound by the capillary exit plane and another at a downstream position where the velocity profile is flat (28). This method has been successfully applied to the solution of extrudate swelling in Newtonian jets (Problem 12.3). The results obtained by such balances in polymers do *not* agree with experiments.

A detailed analysis of extrudate swell by macroscopic balances was carried out by Bird et al. (29), who distinguished between two regimes: a low Reynolds number regime and a high Reynolds number regime. In the latter regime, good analysis can be done using only macroscopic mass and momentum balances, but in the former regime (which includes polymer swelling), the macroscopic mechanical energy balance has to be included in the analysis because of the significant effect of the viscous dissipation term. This renders
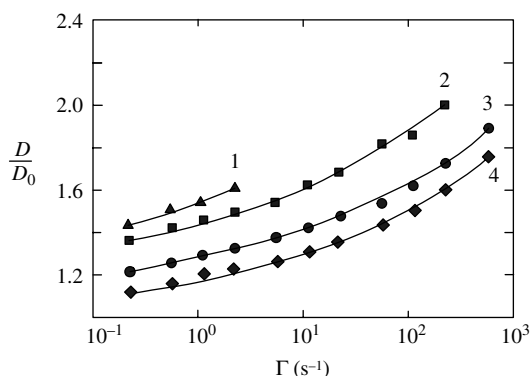

Fig. 12.14 Effect of the method of measurement on the value of D/D_0 for HDPE. Curve 1, frozen extrudates; Curve 2, extrudates annealed at 160°C in hot silicon oil; Curve 3, photographs of extrudates emerging from capillary; Curve 4, photographs of extrudates in hot silicon oil. [Reprinted by permission from J. L. White and J. F. Roman, "Extrudate Swell During the Melt Spinning of Fibers-Influence of Rheological Properties and Take-up Force," *J. Appl. Polym. Sci.*, **20**, 1005 (1976).]

the analysis more difficult, as it requires detailed knowledge of the jet free-surface shape, the distance downstream to fully developed flow, the velocity rearrangement in the die, the Reynolds number, and a new dimensionless group, including the primary normal-stress difference function Ψ_1.

Whipple's careful experimental study of the velocity profile in the region before and after the capillary exit is an initial step in answering some of these needs. He found that polymer melts "anticipate" the swelling phenomenon, in that, just before the exit, axial decelerations and radial velocity components are observed. Thus the exit velocity profile is not the same as in the fully developed region and the flow there is not viscometric.[4]

> **Example 12.1 Recoverable Strain**   Graessley et al. (22) found that, with polystyrene extrudate velocities of 1–3 mm/s in the temperature range of 160°–180°C, about 90% of the final D/D_0 value was reached at an axial distance of 0.1 cm past the capillary exit. The rest of the swelling was completed in the next three centimeters. We wish to calculate the "recoverable strain" at 0.1 cm.
>
> Recoverable strain can also be defined as the tensile strain needed to pull a fully swollen extrudate until its diameter is that of the capillary (22).[5] Assuming constant density $\pi D_2 L/4 = \pi D_0 L_0/4$, or $L_0/L = S_R = (D/D_0)^2$. At 0.1 cm past the capillary exit $S_R = 0.81(D/D_0)^2$, and at 3 cm, it is $(D/D_0)^2$. Therefore, at 0.1 cm, 19 % of the recoverable tensile strain that the extrudate is capable of undergoing is still present. In other words, if no further swelling were allowed, $0.19(D/D_0)^2$ would be the value of the average "frozen-in" strain in the extrudate.

Entrance Flow Patterns

Earlier in this chapter, in discussing the Bagley correction in capillary viscometry, we pointed out the necessity of eliminating entrance pressure drops to get the correct value of the wall shear stress τ_w^*. As Fig. 12.6 indicates, the level of entrance pressure drops is large for polymer melts and solutions. Figure 12.15 gives specific evidence of the magnitude of the ratio of entrance pressure drop to the shear stress at the wall; this is shown for a number of materials. According to Eq. 12.1-1, we obtain that $\Delta P_{en}/\Delta P_{cap} = (D_0/4L^*)$ $(\Delta P_{ent}/\tau_w^*)$. Thus, for LDPE flowing in an $L/D_0 = 2.4$ capillary, $\Delta P_{en}/\Delta P_{cap} = 1$ at a value of $\Gamma = 2\,\mathrm{s}^{-1}$, according to Fig. l2.15. The value of the entrance pressure drop becomes larger than the total capillary pressure drop at higher shear rates. It follows then that, in polymer processing, where the length-to-opening ratios are small and shear rates are high, entrance pressure drops must be included in calculations of the die pressure in die design equations. Entrance pressure drops are, of course, observed with all fluids in regions of conduit cross-sectional changes. This is because the conduit shape and the rheological response of the fluid create extra velocity gradients that, to be sustained, need to be "fed" by stress terms, which give rise to extra pressure drops (i.e., $[\nabla \cdot \tau] = -\nabla P$ in the equation of motion). Newtonian fluids in laminar flow in contracting regions exhibit streamlines that radiate in waves in the entire entrance region, as has been shown by Giesekus (31). This simple flow pattern, together with the simple rheological response of

---

4. The experimental fact that nonviscometric flow prevails at the capillary exit must be taken into account in the discussion of P_{ex} (9) mentioned earlier.

5. Here we use the "engineering strain," $\varepsilon = l(t)/l_0$, and not the "true strain" used in Eq. 3.1-3.
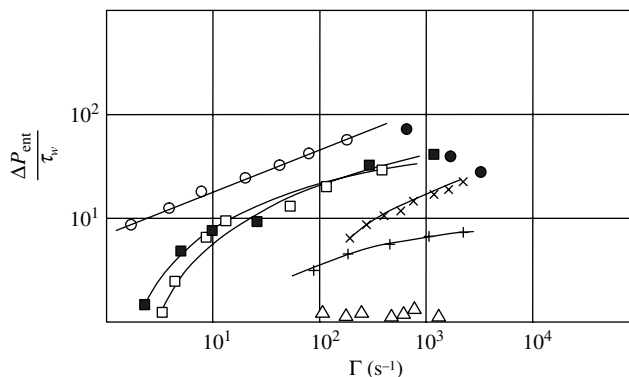
Fig. 12.15 The ratio of entrance pressure drop to shear stress at the capillary wall versus Newtonian wall shear rate, Γ. ■, PP; □, PS; ○, LDPE; +, HDPE; ●, 2.5% polyisobutylene (PIB) in mineral oil; ×, 10% PIB in decalin; △, NBS-OB oil. [Reprinted by permission from J. L. White, "Critique on Flow Patterns in Polymer Fluids at the Entrance of a Die and Instabilities Leading to Extrudate Distortion," *Appl. Polym. Symp.*, No. 20, 155 (1973).]

Newtonian fluids, gives rise to relatively small entrance pressure losses that have been calculated by Weissberg (32) to be

$$\Delta P_{e,N} = \frac{3\mu Q}{2R^3} \tag{12.2-4}$$

where Q is the volumetric flow rate and R is the capillary radius.

Polymer melts and solutions, on the other hand, are rheologically more complex fluids and, even under simple radiating flows in the entrance region, would need more stress components to sustain them; thus there are larger entrance pressure drops. Additionally, the entrance flow patterns with polymer melts and solutions are typically more complex.[6]

Entrance vortices are observed (Fig. 12.16) with the viscoelastic fluid flowing into the capillary from a "wine glass" region (33). Not all polymers exhibit vortices—HDPE and isotactic polypropylene (PP) do not—and all polymer melts and solutions behave like Newtonian fluids at very low shear rates where the viscosity has reached the "Newtonian plateau." As the flow rate is increased, vortices are formed, leading to the conclusion that radiating flow is not compatible with the equation of motion and the constitutive equation describing these fluids. Furthermore, increasing the flow rate results in increasing the vortex size (34).

The large entrance pressure losses are a consequence of the large vortices, which effectively increase the capillary length. Large vortices imply small entrance angles α, as Fig. 12.16 suggests.[7] In turn, small entrance angles give rise to a small elongational extension rate in the region of the wine glass stem. This apparently has led Lamb and Cogswell (35) to relate the entrance angle α to the elongational viscosity $\bar{\eta}$, arguing that

---

6. The viscous contribution to the total entrance pressure loss is very small. [C. D. Han, "Influence of the Die Entry Angle in the Entrance Pressure Drop, Recoverable Elastic Energy and Onset of Flow Instability in Polymer Melt Flow," *AIChE. J.*, **17**, 1480 (1970).]

7. It follows then that the capillary entrance angle affects the value of ΔP_{ent}. Han (37) has shown that, for HDPE, ΔP_{ent} decreases with increasing entrance angle, up to 60°, then remains constant from 60° to 180°.
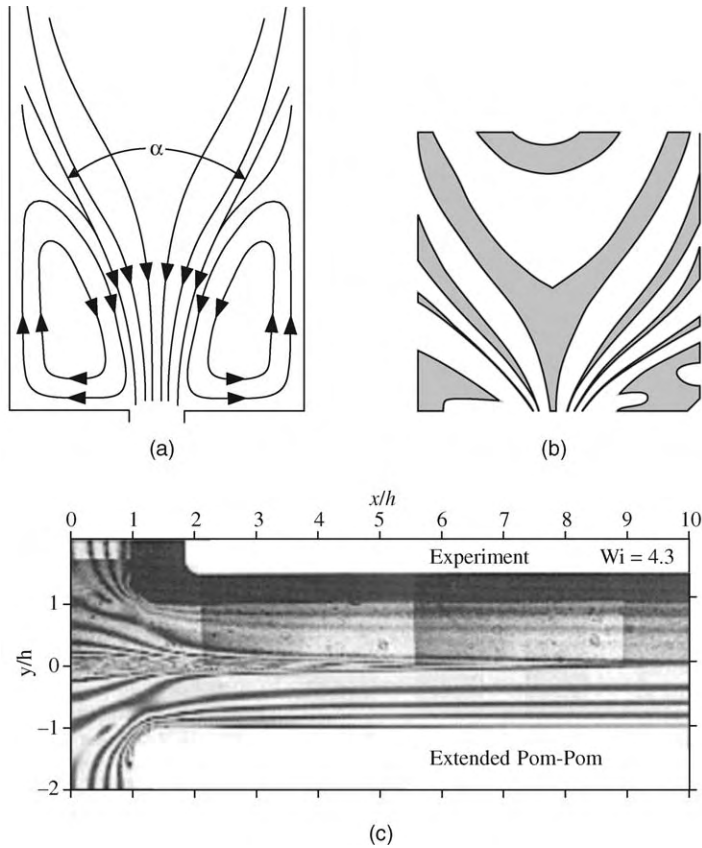
Fig. 12.16 Entrance flow patterns in molten polymers. (a) Schematic representation of the "wine glass" and entrance vortex regions with the entrance angle. [Reprinted by permission from J. L. White, "Critique on Flow Patterns in Polymer Fluids at the Entrance of a Die and Instabilities Leading to Extrudate Distortion,"*Appl. Polym. Symp.*, No. 20, 155 (1973).] (b) Birefringence entrance flow pattern for a PS melt. [Reprinted by permission from J. F. Agassant, et al., "The Matching of Experimental Polymer Processing Flows to Viscoelastic Numerical Simulation," *Int. Polym. Process.*, **17**, 3 (2002).]

melts with high elongational viscosity would favor small elongational rates, and thus small entrance angles. The relationship proposed is

$$\alpha = \tan^{-1} \frac{2\eta}{\bar{\eta}} \qquad (12.2\text{-}5)$$

The ratio of shear to elongational viscosities becomes smaller with increasing deformation rates, giving rise to smaller entrance angles and, consequently, larger entrance vortices, as observed experimentally.

   Ballenger and White (34) relate the entrance angle α in degrees to the ratio of the entrance pressure loss to the capillary wall-shear stress, $\Delta P_{\text{ent}}/\tau_w^*$

$$\alpha = 178.5(0.9644)^{\Delta P_{\text{ent}}/\tau_w^*} \qquad (12.2\text{-}6)$$

The relationship is experimental. LaNieve and Bogue (36) have related the entrance pressure losses of polymer solutions to the viscosity and primary normal stress difference coefficient. Thus, the works of Ballenger and LaNieve, taken together, seem to imply that the entrance angle (thus the size of the entrance vortices) depends on both the viscosity and the first normal stress difference coefficient. White and Kondo (38) have shown experimentally that, for LDPE and PS

$$\alpha = f\left[\frac{(\tau_{11} - \tau_{22})_w}{(\tau_{12})_w}\right] \tag{12.2-7}$$

Equations 12.2-6 and 12.2-7 seem to imply that the entrance (or "ends") pressure losses are simply related to the first normal stress difference function at the capillary wall. Indeed they find that

$$\frac{\Delta P_e}{(\tau_{11} - \tau_{22})_w} \cong 2 \tag{12.2-8}$$

A better understanding of the exact origins of the entrance pressure loss in polymer melts requires the experimental determination of the precise flow field in that region. Until such work and the subsequent analysis have been completed, it suffices to state that entrance pressure losses with polymer melts are large, since these fluids are viscoelastic and exhibit large extensional viscosity values. For die design purposes, we must have experimentally available data, such as those obtained with zero-length capillaries, or with a number of different L/D_0 capillaries by extrapolations to $L/D_0 = 0$.

Extrude Melt Fracture

In the flow of molten polymers through capillaries and other dies, a striking phenomenon is observed of shear stresses at the wall of the order of 10^5 N/m^2. As the flow rate is increased, there is a *critical stress* level at and above which the emerging polymer stream exhibits irregular distortion. This distortion contributes evidence for some irregularity or resistability in flow.

The preceding observations originated with Tordella (39), who not only investigated the field of unstable polymer melt pressure flow but has written lucidly on it, coining the term "melt fracture" for the just-described phenomena. The phenomenon was first studied by Spencer and Dillon (40), who found that the critical wall shear stress is independent of the melt temperature, and inversely proportional to the weight average molecular weight. These conclusions have remained essentially valid to date. Aside from the review by Tordella (39), two more review papers should be mentioned: one general article on polymer processing instabilities by Petrie and Denn (41), and more recently, a thorough review of the many facets of melt fracture by Denn (42).

Looking at the melt fracture of specific polymers, we see many similarities and a few differences. Polystyrene extrudates begin to spiral from smooth at $\tau_w^* \approx 10^5$ N/m^2, and at higher shear stresses, they are grossly distorted. Visual observations show a wine glass entrance pattern with vortices that are stable at low stress values and spiral into the capillary and subsequently break down, as τ_w^* is increased. Clearly, melt fracture is an entrance instability phenomenon for this polymer.

Similar observations have been made with polypropylene, with two qualitative differences. The flow entrance angle is very large, almost 180°, and the observed spiraling of the extrudate is very regular. LDPE extrudates transit from smooth to dull or matte at subcritical values of τ_w^*. With increasing shear stress, they begin to spiral over a narrow range of τ_w^*, and subsequently become grossly distorted.

Corresponding to smooth and matte extrudates, very small entrance angles but stable patterns are observed at the capillary entrance. This flow pattern spirals in the capillary at high stresses, and at the critical shear stress, the wine glass stem flow lines are grossly disrupted. With the exception of the appearance of the matte extrudate surface, which is an exit fracture phenomenon as has been demonstrated by Cogswell and Lamb (43) and Vinogradov (44), and which will be further discussed below, LDPE behaves in the melt fracture region similarly to PS and PP.

In the three polymers just named, two more observations are worth mentioning. First, at the melt fracture onset, there is no discontinuity in the flow curve (τ_w^* vs. $\dot{\gamma}_w^*$). Second, as expected, because the entrance is the site of the instability, increasing L/D_0 decreases the severity of extrudate distortions.

HDPE exhibits extrudates that are smooth at low τ_w^* values, and display "sharkskin" (a severe form of matte) and regular, helical screw thread surface patterns in the subcritical stress region (Fig. 12.17), followed by grossly distorted shapes, which are accompanied by large pressure fluctuations at constant flow rates. That is, in the distorted extrudate region, there is a discontinuity in the flow curve. At higher stresses (flow rates), the extrudate surface becomes smooth again, a fact that may be utilized in fast shaping operations such as wire coating and blow molding of HDPE. The distortions either are not affected or become amplified with increasing L/D_0 (45).

Fig. 12.17   Scanning electron micrograph of HDPE extruded at a shear rate slightly lower than the oscillation region, showing "sharkskin." [Reprinted by permission from N. Bergem, "Visualization Studies of Polymer Melt Flow Anomalies in Extruders," *Proceedings of the Seventh International Congress on Rheology*, Gothenberg, Sweden, 1976, p. 50.]
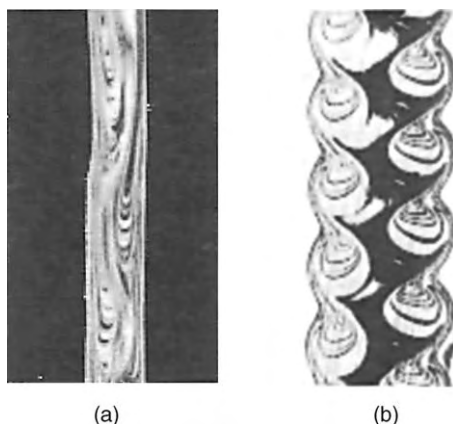
Fig. 12.18   Flow patterns above the oscillating region of HDPE. (a) Microtome cut along the cylinder axis of HDPE solidified inside a capillary die showing that the flow patterns are formed at the die entrance. (b) Microtome cut of the HDPE extrudate resulting under the same conditions as in (a). [Reprinted by permission from N. Bergem, "Visualization Studies of Polymer Melt Flow Anomalies in Extruders," *Proceedings of the Seventh International Congress on Rheology*, Gothenberg, Sweden, 1976, p. 50.]

The entrance flow pattern at low flow rates corresponding to the matte or smooth extrudates is stable with a very wide wine glass entrance angle ($\alpha \sim 180°$). Bagley and Birks (33) have observed only high-frequency oscillations into the capillary at the critical shear stress region, whereas White (34), Oyanagi (46), and Bergem (47) have reported spiraling flow patterns into the die, well into the distorted extrudate regions.

The site of the sharkskin distortion is again the die exit, and so is the screw thread pattern. The site of, and the mechanism for the gross extrudate distortion are problems that have no clear answers. The work of White and Ballenger, Oyanagi, den Otter, and Bergem clearly demonstrates that some instability in the entrance flow patterns is involved in HDPE melt fracture. Clear evidence for this can be found in Fig. 12.18. Slip at the capillary wall, to quote den Otter, "does not appear to be essential for the instability region, although it may occasionally accompany it."

The idea of slip at the wall was first proposed by Tordella and later gained popularity because it can be used to explain the discontinuity in the HDPE flow curve (48) and the fact that, at shear stresses above the discontinuity, the extrudate becomes smooth again (the melt is continuously slipping at the wall). Den Otter (45) has found evidence of slip in the flow of linear elastomers. Thus, it is possible that, through molecular disentanglement at a certain stress level, a low viscosity layer is formed at the die entrance which, if it is at the periphery, would result in the flow patterns of Fig. 12.18. If disentanglement is involved for the entrance region, there is no reason to exclude it in the capillary where a surface layer of low viscosity film would be formed, acting as an effective lubricant (see section 2.11).

With the discovery and development of metallocene-based LLDPEs with narrow MWD and high molecular weight, there has been a flurry of investigations with these polymers, because they exhibit sharkskin melt fracture at quite low and industrially limiting production rates. The objective of such studies is to increase the rate of production with
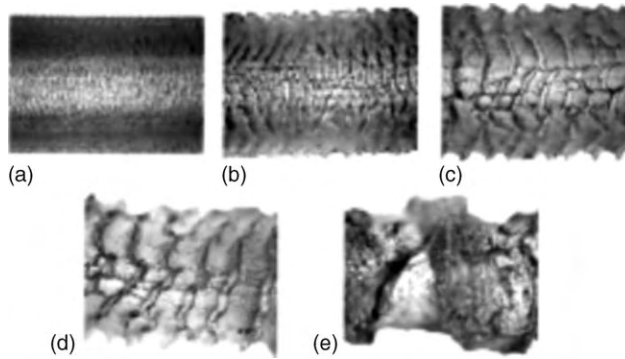
Fig. 12.19 Cold postextrusion micrographs as a function of the flow rate. The processing conditions were $T = 177°C$ and no PPA. Each image is actually a composite of two micrographs in which the side and top are focused. The relative errors in throughputs are 0.05 Q = (a) 1.0, (b) 2.2, (c) 3.8, (d) 6.3, and (e) 11 g/min. The width of each image corresponds to 3 mm. [Reprinted by permission from K. B. Migler, "Extensional Deformation, Cohesive Failure, and Boundary Conditions during Sharkskin Melt Fracture," *J. Rheol.*, **46**, 383–400 (2002).]

sharkskin-free extrudates. The incorporation of two processing additives, fluoroelastomers (49) and boron nitride (50) achieves this, but at the expense of adulterating the base polymers. Thus, the studies continue to probe two basic questions relating sharkskin in LLDPE extrudates: first, where is the location of origin of this flow instability and, second, what is the cause with LLDPEs.

Migler et al. (49) observe that (a) the fracture phenomena progress with increasing flow rate from smooth, to sharkskin, to grossly deformed extrudates, as shown in Fig. 12.19; (b) the onset of sharkskin is *not associated with slip* at the capillary wall just upstream of the exit, as shown by the velocity profiles on Fig. 12.20 measured with
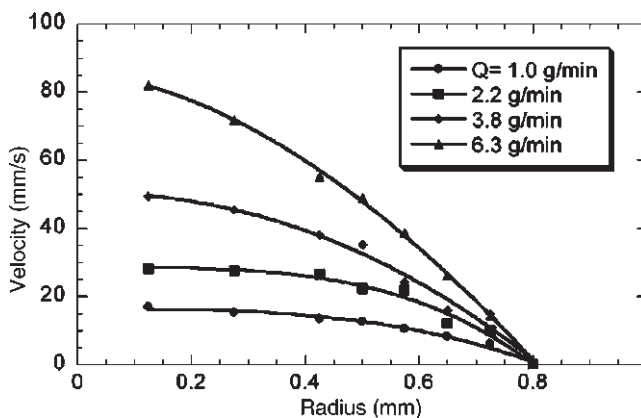

Fig. 12.20 Flow velocimetry as a function of the radial position of the polyethylene *inside* the capillary die for a series of flow rates. Measurements were taken at $x = -0.2$ mm (no PPA). [Reprinted by permission from K. B. Migler, "Extensional Deformation, Cohesive Failure, and Boundary Conditions during Sharkskin Melt Fracture," *J. Rheol.*, **46**, 383–400 (2002).]
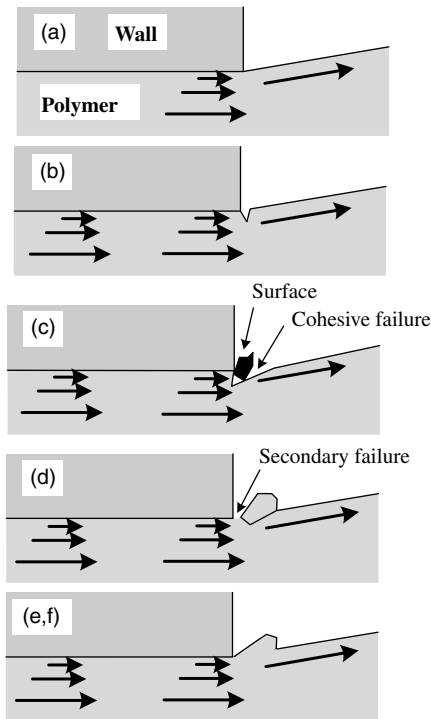
Fig. 12.21   Sketch of the kinetics of the sharkskin instability, side view. [Reprinted by permission from K. B. Migler, "Extensional Deformation, Cohesive Failure, and Boundary Conditions during Sharkskin Melt Fracture," *J. Rheol.*, **46**, 383–400 (2002).]

particle-tracking velocimetry through a quartz capillary. Thus, the phenomenon originates at the capillary exit, as was first presented in clear physical terms by Cogswell (51); (c) the cause appears to be *cohesive failure* of the polymer melt at the capillary exit corner, as shown schematically in Fig. 12.21(b); this splits the extrudate into a core and a surface layer, as shown in Fig. 12.21(c).

As the extrudate proceeds downstream, there is a secondary failure that creates the sharkskin ridge [Fig. 12.21(d)]. Following the *ridge creation*, whose amplitude increases with flow rate (Fig. 12.19), there is an axial movement of the core downstream, till the repetition of the cycle [Fig. 12.21(e,f)]; the period of the ridge-core repetition is also flow rate dependent.

The cohesive failure is brought about by the sudden and large axial acceleration of the melt layer next to the capillary wall, as shown by Migler et al. (49) in Fig. 12.22(a). Figure 12.22(b) shows that the addition of a flouroelastomer (PPA) additive allows the formation of a slip that is larger upstream from the exit, as shown on Fig. 12.23, which reduces the axial acceleration and the level of extensional deformation and rate.

Recently, Muliawan et al. (52), who have been studying melt fracture, and in particular sharkskin extrudate instabilities over the last decade, have presented interesting experimental results relating the extensional stress–Hencky strain behavior of polymer melts to their sharkskin (exit) and gross (capillary entrance) melt fracture behavior. For the purposes of this discussion, results obtained with two Nova Chemicals
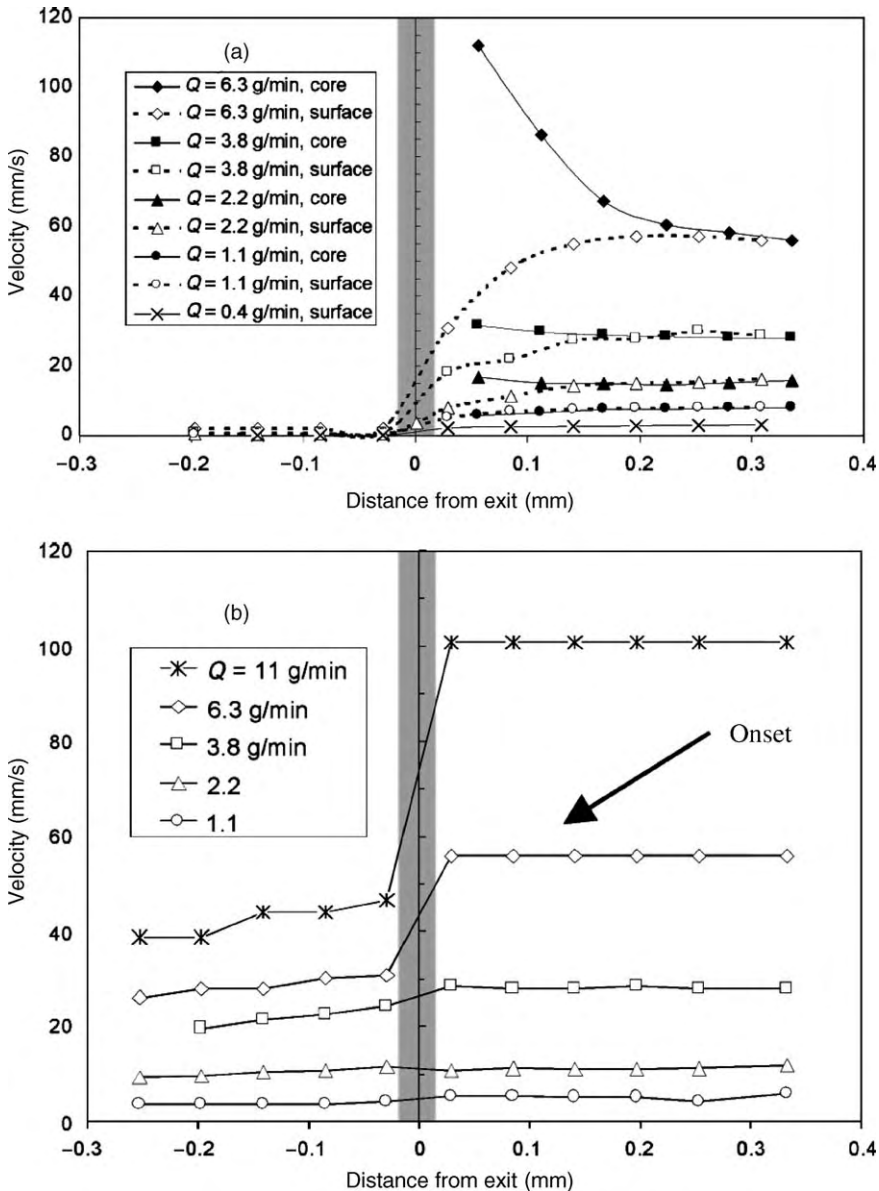
Fig. 12.22 Velocity of the polymer in the vicinity of the wall as it makes the transition from inside to outside the capillary die. For $x < 0$ (inside the die), measurements were made of slow-moving particles, that is, those nearest the wall. For $x > 0$ (outside the die), the measurements were made at the air–polymer interface. The flow rate at which the onset of sharkskin is observed is noted. (a) Without the polymer process additive. For the higher flow rates, we show the velocity of both the core and the surface regions. (b) With the polymer process additive. [Reprinted by permission from K. B. Migler, "Extensional Deformation, Cohesive Failure, and Boundary Conditions during Sharkskin Melt Fracture," *J. Rheol.*, **46**, 383–400 (2002).]
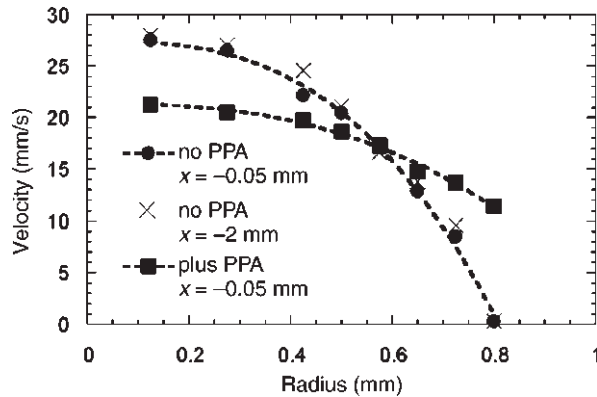
Fig. 12.23 Flow velocimetry as a function of the radial position of the polyethylene *inside* the capillary die for a $Q = 2.2$ g/min [the same as in Fig. 12.19(b)]. The measurements were taken at $x = -0.05$ and -2 mm upstream of the exit. Also shown is the case with PPA. [Reprinted by permission from K. B. Migler, "Extensional Deformation, Cohesive Failure, and Boundary Conditions during Sharkskin Melt Fracture," *J. Rheol.*, **46**, 383–400 (2002).]

Corporation film-grade Ziegler-Natta linear low density polyethylenes will be presented. They are Resin E, Nova FP-015-A, MFI = 0.55, $\rho = 0.9175$ g/cc, and Resin C, Nova PF-120-F, MFI = 1.00, $\rho = 0.9170$ g/cc. Their capillary-flow behavior in terms of apparent shear stress vs. apparent shear rate are shown on Fig. 12.24. The melt fracture onset is also noted in Figure 12.24 and the data presented in the table below, indicate that resin E undergoes both sharkskin and gross melt fracture at lower apparent shear rates and stresses.

Critical Shear Rates and Stresses for All Resins in Capillary Die Extrusion at 170°C

Sample I.D.		Critical Shear Rate (s^{-1}) and Stress (MPa) for the Onset of	
		Sharkskin	Gross melt
C (LLDPE FP-120-F)	Apparent shear rate	100	1100
	Apparent shear stress	0.24	0.42
E (LLDPE FP-015-A)	Apparent shear rate	40	700
	Apparent shear stress	0.20	0.39

The extensional melt behavior was assessed with the new SER Universal Testing Platform from X-pansion Instruments, described by Sentmanat (53,54) and shown in Fig. 12. 25. The obtained tensile stress of the two resins at 170°C and extensional rate of 20 s^{-1} are shown on Fig. 12.26. It is evident that Resin E has a higher modulus and higher tensile stress values, at a given strain below yield, than Resin C. From this, and the experimental data discussed previously, we see that the values of the critical shear rate and shear stress for the onset of sharkskin fracture are inversely proportional to the magnitude of the tensile stress of the resins. This suggests that the rapid increase
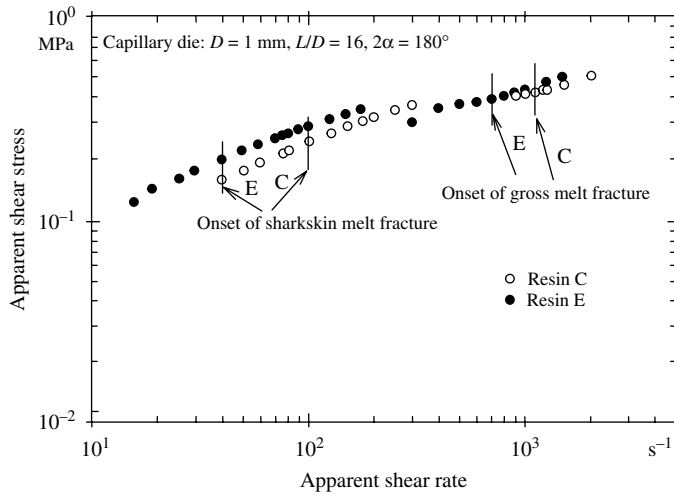
Fig. 12.24 Flow curves of LLDPE resins E and C, indicating the onset of sharkskin and gross melt fracture for each resin. $T = 170°C$, capillary: $D = 1$ mm, $L/D = 16$, with entrance angle $2\alpha = 180°$. [Reprinted by permission from E. G. Muliawan, S. G. Hatzikiriakos, and M. Sentmanat, "Melt Fracture of Linear Polyethylene," *Int. Polym. Process.*, **20**, 60 (2005).]

in extensional stresses leads to an earlier "rupture" of the melt at the capillary exit wall circumference, where *elongational stresses and strains* are the highest, with subsequent rupture propagation toward the center, where they are the lowest. Extensional rheological data on branched low density polyethylene by Sentmanat and Hatzikirakos (55) indicate that the presence of long chain branches retards tensile stress growth to much higher strains, due to the dissipative interaction of the polymer branch entanglements prior to the main chain stretch. This, they claim, is the reason that sharkskin melt fracture is not observed with LDPEs.
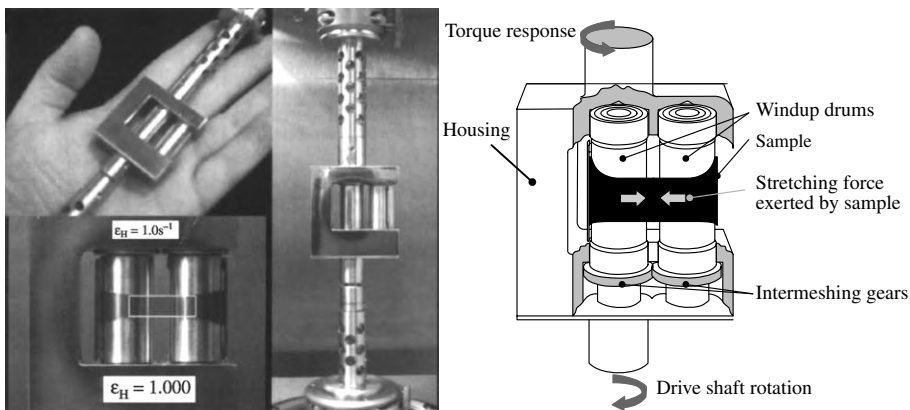

Fig. 12.25 The Universal testing platform fitted on a rotational Rheometrics RDA II rheometer host station. The two counterrotating cylinders where the film is mounted cause the application of the extensional strain. [Reprinted by permission from E. G. Muliawan, S. G. Hatzikiriakos, and M. Sentmanat, "Melt Fracture of Linear Polyethylene," *Int. Polym. Process.*, **20**, 60 (2005).]

Fig. 12.26   True tensile stress–Hencky strain curves for resins C and E at Hencky strain rate of 20 s^{-1} and temperature of 170°C. [Reprinted by permission from E. G. Muliawan, S. G. Hatzikiriakos, and M. Sentmanat, "Melt Fracture of Linear Polyethylene," *Int. Polym. Process.*, **20**, 60 (2005).]
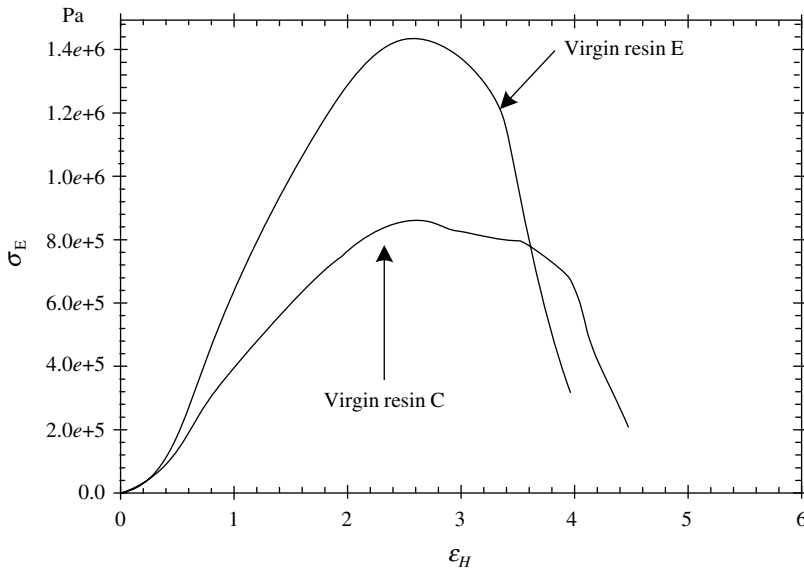
Gogos et al. (56) conducted extensive studies on the morphological features of the surface melt fractured extrudates of metallocene catalyzed LLDPE in pelletizing dies. They concluded that the morphological evidence, Fig. 12.27, suggested strongly that surface melt fracture of LLDPE is due to cohesive ("peel") strength failure of the melt layer *next to the wall at the die exit* of the pelletizing die, under the burden of local high shear *and* extensional stresses, as Cogswell (51) suggested in 1977. The objective of their study was to develop pelletizing dies that *extend* the shear rate range of surface melt fracture-free extrudates, *without the use of processing aids.* They were able to meet this objective by developing "integrally heated" die plates, which heat the die exit corner region to unusually high temperatures (up to 200°C higher than the melt bulk temperature) (57). Thus, while the bulk melt temperature is unaffected, a very low viscosity melt layer is formed next to the wall of the die exit-corner region, forming a melt slip layer and rendering the exiting extrudate "immune" to cohesive failure. With such integrally heated pelletizing dies, they were able to obtain smooth extrudates at nominal calculated shear stress levels of 0.65 MPa, well above the critical sharkskin surface melt fracture levels with LLDPE (see Fig. 12.24). Smooth, sharkskin-free extrudates were obtained at flow rates as high as three times those with conventional conductively heated pelletizing dies, both in air and under water, as shown on Fig. 12.28. Similarly, beneficial effects were observed with Ziegler catalyzed LLDPE resins, LLDPE with and without processing aids, and with dies made of stainless steel and brass. Such integrally heated dies hold the promise of substantially increasing the current operating rates in postreactor finishing operations, which are limited by the onset of sharkskin melt fracture.

We now turn to the gross melt fracture behavior. Estimates of the prevailing extensional rates at the capillary entrance indicate that their value corresponding to the critical gross melt fracture conditions is larger that the 20 s^{-1} used in this work. Nevertheless, since
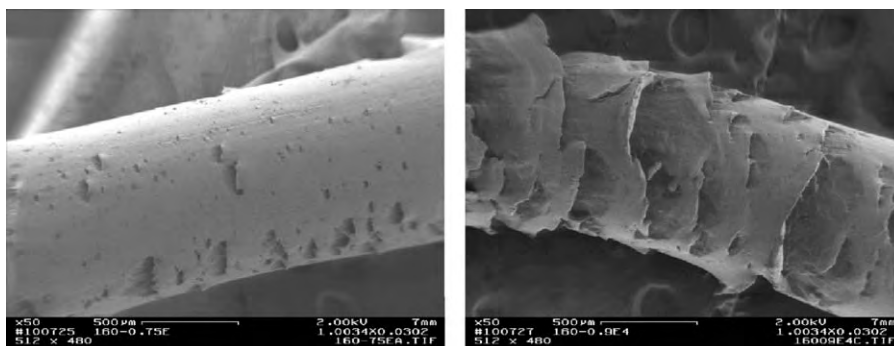
Fig. 12.27 Surface morphological features of mLLDPE (ExxonMobil Exceed^{TM} 350D60) extrudates obtained at 160 °C with a tungsten carbide die: $D = 0.767$ and $L = 25.5$ mm just above and in the sharkskin melt fracture flow-rate region. [Reprinted by permission from C. G. Gogos, B. Qian, D. B. Todd, and T. R. Veariel, "Melt Flow Instability Studies of Metallocene Catalyzed LLDPE in Pelletizing Dies," *SPE ANTEC Tech. Papers*, **48**, 112–116 (2002).]

20 s^{-1} is the highest attainable value with this instrument at present, the tensile stress versus Hencky strain at this rate is used to explain the inverse relation between the modulus and the tensile stress values and the critical shear rate for the onset of gross melt fracture, as previously shown. Resin E has the higher tensile modulus, thus the higher increase in extensional stress, with this polymer reaching its critical gross melt fracture stress at an earlier (lower) rate. Thus, for exit and entrance melt fracture phenomena, the strain dependent, high strain rate, extensional stress behavior appears to be an indicator, if not a predictor, of the early shear-rate and shear-stress susceptibility of LLDPEs to such instabilities.

12.3 SHEET FORMING AND FILM CASTING

Polymer flat film sheets are formed continuously by extruding a polymer through a more or less rectangular sheeting die, which is quite wide with a small opening. Because the extruder outlet is by necessity circular, and the die rectangular, two fluid particles feeding
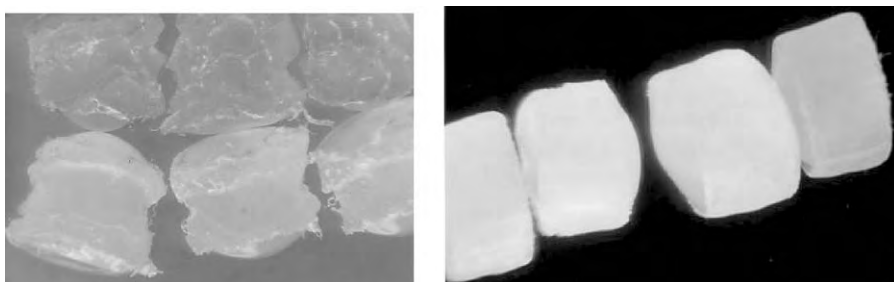

Fig. 12.28 Melt-fractured pellets extruded at 8 kg/h per die hole (3.2 mm in diameter) from a conventional underwater pelletizing die (left) and smooth pellets extruded under the same conditions at 24 kg/h per die hole from the same underwater pelletizing die when locally heated to high temperature (right) (57).

two arbitrarily chosen die positions will have gone through different flow histories, and this may result in a nonuniform flow rate through the die, dependent on the position along the die width. As seen in Fig. 12.29(b), the triangular region exists for that purpose, providing width-dependent flow resistance.

Additionally, the role of the relaxation region is to help erase the width-dependent upstream flow history. Thus the design and the choice of the flow passages from the extruder to the die per se are of great importance. A number of sheeting-die designs representing different practical as well as theoretical solutions are currently in use.

Upon exiting the die, the sheet extrudate will swell to a level determined by the polymer, the melt temperature, the die length-to-opening ratio, and the shear stress at the die walls. Additionally, flow instabilities will occur at values of the corrected shear stress at the wall, of the order of, but higher than 10^5 N/m^2, as found by Vlachopoulos and Chan (58), who also concluded that, for PS, HDPE, and LDPE, the critical S_R in slits is 1.4 times higher than in tubes of circular cross section. Aside from these differences, the information presented in Section 12.1 and 12.2 applies to slit flow.

Polymer sheets are cooled without stretching by convected cold air (or an inert gas), by immersion into a fluid bath, or by passage over chilled rolls. Flat films are usually stretched and oriented uniaxially and cooled by either of the methods previously mentioned. Films are also cast and cooled on rolls for optimal clarity purposes.
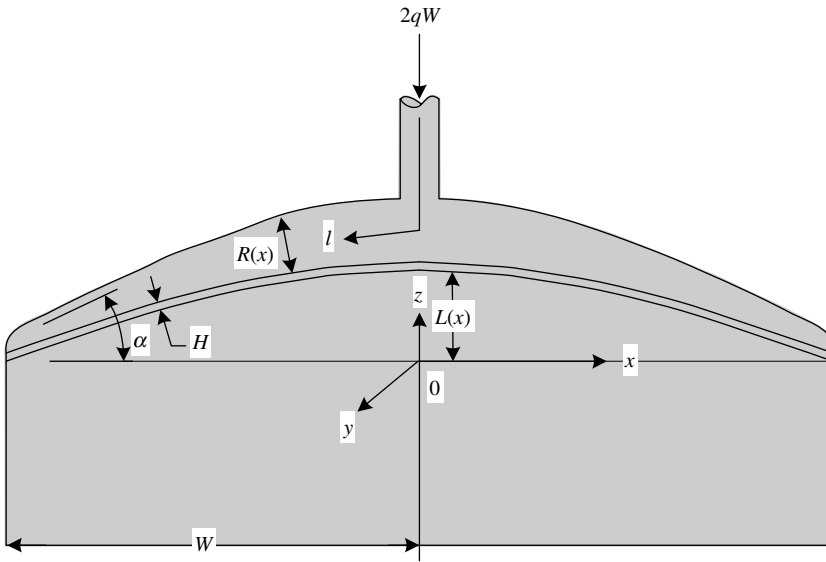
Die Design Equations

The most common mechanical sheet die designs are the center-fed "T" and the "coat hanger." In both cases, the melt is fed into the center of the manifold, which has a circular or bead-shaped cross section. The manifold distributes the melt into the approach channel through a slit opening running along its entire length. The names T and coat hanger refer to the angle the manifold makes with the flow direction (Fig. 12.29).

Sheet die design equations were first developed by Carley (59) for T-shaped dies using Newtonian fluids. Pearson (60), whose basic approach we now elucidate, extended the design equations to Power Law fluids. The proper die design delivers a given polymer melt under specified conditions through a constant die opening at a constant rate and temperature (cross-machine direction uniformity). Here, we trace the development of a die design equation that has this design objective.[8]

Figure 12.29 presents the geometrical features of the coat-hanger die, on which the design equation will be developed. The manifold is a tubular, variable radius channel of curved axis l. The slit opening H is constant. The only geometric restriction is that the manifold be of a small curvature, so that the lubrication approximation can be applied in the manifold region. Also, for the same reason, $dR(x)/dx \ll 1$.

Assuming that the pressure at the manifold entrance is constant and that the problem is isothermal, we have a constant flow rate entering the die (machine direction uniformity). Our objective is to ensure cross-machine direction uniformity, that is, constant flow rate at

---

8. In practice, die design does not concern itself simply with the design of the flow passages to control the flow and produce a uniform extrudate—the only aspect we deal with—but also with mechanical design to ensure rigidity of the die under the operating temperatures and pressures, and with chemical and abrasion resistance to the polymers being formed. It also involves the design of an adequate temperature control system, especially in sheeting dies where the surface-to-volume ratio is very large.
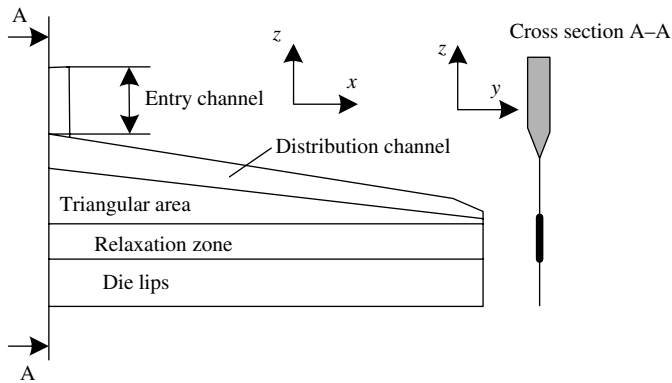
Fig. 12.29   Schematic representations of the coat-hanger die design.

$z = 0$. But since the slit opening is constant,

$$\frac{dP}{dz} = a = \text{constant} \tag{12.3-1}$$

This holds everywhere in the parallel-plate flow region formed by the slit, where z-constant lines are isobars as a consequence. Integrating Eq.12.3-1 yields

$$[L(0) - L(x)]a = P_0 - P'(l) \tag{12.3-2}$$

where $P'(l)$ is the manifold pressure at position l, and P_0 is the manifold entrance (delivery) pressure; x and l are related geometrically through the shape of the manifold.

Differentiating Eq. 12.3-2 with respect to l results in the following relationship between the pressure gradient in the manifold, its shape, and the pressure gradient in the slit region:

$$\frac{dP'}{dl} = a\frac{dL}{dl} \tag{12.3-3}$$

The preceding relation is the general design equation satisfying the objective set in the beginning of this section. It holds for any fluid. Thus, let us give it a usable form by considering a Power Law fluid flowing in this die. Turning first to the parallel plate region formed by the slit, the z-component momentum equation reduces to

$$-\frac{dP}{dz} - \frac{d\tau_{yz}}{dy} = 0 \tag{12.3-4}$$

For a Power Law fluid, $\tau_{yz} = -m|dv_z/dy|^{n-1}dv_z/dy$, and using the appropriate boundary conditions in this assumed fully developed flow, we obtain, after integration (note that flow is in the negative z direction)

$$v_z(y) = \frac{n}{n+1}\left(\frac{1}{m}\frac{dP}{dz}\right)^{1/n}\left(\frac{H}{2}\right)^{(n+1)/n}\left[\left(\frac{2|y|}{H}\right)^{(n+1)/n}-1\right] \tag{12.3-5}$$

or

$$v_z(y) = \left(\frac{1}{1+s}\right)\left(\frac{1}{m}\frac{dP}{dz}\right)^{s}\left(\frac{H}{2}\right)^{1+s}\left[|\xi|^{1+s}-1\right] \tag{12.3-6}$$

where $s = 1/n$ and $\xi = 2y/H$. Integrating over the gap opening, we obtain the following relationship between the pressure drop and the flow rate per unit width, q, taken to be positive in the negative z direction:

$$a = \frac{dP}{dz} = 2^{n+1}(2+s)^n m\frac{q^n}{H^{2n+1}} \tag{12.3-7}$$

For the flow inside the manifold of a circular cross-section[9] channel, we assume that, locally, we have fully developed tube (capillary) flow. That is, we disregard the channel curvature, the channel tapering off, and the effects of the leak flow into the slit region. The following relationship was derived previously (see Table 12.3):

$$-\frac{dP'}{dl} = \left(\frac{3+s}{\pi}\right)^n 2m\frac{Q^n(l)}{R(x)^{3n+1}} \tag{12.3-8}$$

---

9. As Fig. 12.1 indicates, the manifold cross section may be bead shaped and not circular. Thus, pressure flow in an elliptical cross-section channel may be more appropriate for the solution of the manifold flow. Such a problem, for Newtonian incompressible fluids, has been solved analytically. (J. G. Knudsen and D. L. Katz, *Fluid Dynamics and Heat Transfer*, McGraw-Hill, New York, 1958). See also, Table 12.4 and Fig. 12.51.

From a mass balance point of view, the flow rate in the manifold at any point $Q(l)$ provides for the melt that flows in the slit region from that point on to the end of the manifold. Specifically,

$$Q(l) = Q(x) = q(W - x) \qquad (12.3\text{-}9)$$

Combining Eqs. 12.3-8 and 12.3-9 gives

$$-\frac{dP'}{dl} = \left(\frac{3+s}{\pi}\right)^n 2m \frac{[q(W-x)]^n}{R(x)^{3n+1}} \qquad (12.3\text{-}10)$$

Inserting Eqs. 12.3-7 and 12.3-10 into the general design equation 12.3-3, we obtain the specific design equation for Power Law fluids:

$$\frac{2^n(2+s)^n}{H^{2n+1}}\left(\frac{dL}{dl}\right) + \left(\frac{3+s}{\pi}\right)^n 2m \frac{[q(W-x)]^n}{R(x)^{3n+1}} = 0 \qquad (12.3\text{-}11)$$

Given the product width $2W$ and the rheological parameter n, there are two geometric (die design) parameters available: for a given manifold axis curvature, dL/dl or dL/dx, there exists a manifold radial taper profile $R(x)$ that results in a uniform pressure at any $z = $ constant line. In particular, $P(0) \neq f(x)$; this, together with the fact that $H \neq f(x)$, guarantees the design objectives. Conversely, for a given $R(x)$ there exists an $L(l)$ or $L(x)$ that ensures the die design objectives. Generally, for simplicity of construction, constant dL/dl is used. Note that the preceding expression provides the value of the radius at the center $R(0)$, which is necessary for designing a die.

It is worth noting that *not* all $R(x)$ and $L(l)$ or $L(x)$ are acceptable solutions. Any solution that proposes a steeply curving manifold axis or a steeply tapering manifold radius would interfere with the lubrication approximation made during the solution. Furthermore, some solutions may be unacceptable from a machining point of view or because of die-strength considerations. Finally, some designs may be preferable over others, either because the die design equation applies to them more rigorously (the design is such that the assumptions made are reasonable), or because construction is easier. In the first case, more confidence can be placed in the design, and in the second, the die can be made more economically.

Figure 12.29 shows that the die does not end at the plane $z = 0$. Because polymer melts are viscoelastic fluids, it extends to downstream to the end of the die lip region so that a uniform "recent" flow history can be applied on all fluid elements. In deriving the die design equation, we disregarded the viscoelasticity of the melts, taking into account only their shear thinning character.

Example 12.2   Coat Hanger Die Design   We specify the coat hanger die manifold radius along the entire width of the die, if the manifold axis is straight and makes an angle $\alpha = 5°$ with the x coordinate (see Fig. 12.29). The slit opening is set at $H = 0.05$ cm, the half-width $W = 100$ cm, and the Power Law index of the polymer melt $n = 0.5$.

From Eq. 12.3-11 the following expression for $R(x)$ is obtained

$$R(x)^{3n+1} = -\frac{[(3+s)/\pi]^n H^{2n+1}(W-x)^n}{2^n(2+s)^n(dL/dl)}$$

where $dL/dl = -\sin \alpha = -0.0872$. Thus, for $n = 0.5$ the preceding equation reduces to

$$R(x) = 0.175(W - x)^{0.2}$$

Thus, the manifold radius at the center is $R(0) = (0.175)(2.51) = 0.44$ cm, and the value close to the edge at 90 cm is $R(90) = (0.175)(1.58) = 0.277$ cm. The manifold tapered tube is open to form the slit opening over an angle β such that $\sin[\beta(x)/2] = (H/2)/R(x)$. Thus at $x = 0$ $\beta(0) = 13°$ and at $x = 90$ cm $\beta(90) = 21°$. This design results in a very slight taper of the radius of the manifold, about 2×10^{-3}. Also worth noting is that the maximum value of the manifold radius is only about nine times the slit opening. Finally the taper decreases slightly with decreasing n, while the dependence of the manifold radius on H increases with decreasing n. The manifold radius becomes infinite at $\alpha = 0$ and is very sensitive to α when it has small values. Note that the solution is independent of m.

Other flat film die design equations have been proposed in the literature. The one advanced by McKelvey and Ito (61) has as a design objective the flow rate uniformity along the die width. This is achieved by varying the final die lip opening. Thus, although the resulting flow rate is independent of the width direction, the film or sheet thickness is *not*. Additionally, the wall shear rate for a Power Law fluid

$$\dot{\gamma}_w = \frac{2(s+2)q}{H^2(x)} \tag{12.3-12}$$

will be width dependent, allowing extrudate swelling to vary.

The die design equation proposed by Pearson (60) utilizes a constant die lip opening, but an approach-channel-taper that varies with the die width. Thus, in the region between the manifold and the die lip opening both the pressure and flow fields are two-dimensional. This may affect the flow in the die lip region, since the fluid is viscoelastic with memory of this recent upstream flow experience.

The following criticisms apply to all the die design equations for sheet forming that have been proposed so far:

1. The manifold and slit flows are treated independently, disregarding the disturbances in both flow fields as a result of the transition flow from the manifold to the slit, including "entrance" losses. To reduce the latter, tapered, wedge-shaped manifolds are used.

2. The flow is assumed to be isothermal. In any real sheet forming operation, some temperature gradients, both in the melt and along the die, will be present (19).

3. The die lip deflection under the pressure applied by the flow is neglected. This could be accounted for, at least approximately, by rather straightforward beam calculations and iterative procedures, as suggested by Pearson (60).

4. The die designs developed or mentioned previously are for a specific polymer and specific processing conditions. Nonuniform sheets of another polymer would result if substitutions were made. The same holds true for the same polymer extruded at a different temperature.

For these reasons, die lip opening adjustor bolts are provided with every sheeting die to make fine adjustments. Usually these adjustments are made manually. Because the die flows are

often quite fast and manual corrections of sheet thickness nonuniformities result in material waste, feedback systems have been devised to adjust lip openings automatically. Multiple extruders can be used for very wide dies, or a screw may be placed in the manifold of a T die.

If ''machine direction'' thickness uniformity is a problem, it can best be remedied with the use of a gauge detector (beta gauge) that is part of a control system adjusting the speed of the take-up device, to correct for thickness nonuniformities. Small period variations are very difficult to remedy in this fashion.

It can generally be said that the approach to developing die design equations, irrespective of the basic die type, is the following:

1. Simplify the actual flow by assuming that it is a series of well-identified viscometric flows.
2. By applying one or more mass balances, relate the volumetric flow rates in each of the viscometric flows.
3. Allowing for one or more die geometric parameters to be variable, state one or more ''extrudate uniformity conditions'' that, when satisfied (solved for), will determine the geometric variables given previously as functions of other geometric, process, material constants.

Obviously, this method of developing die design equations implies that there is no unique die design to achieve product uniformity in the cross-machine direction. Multiple alternative designs—and thus die design equations—exist because one has an a priori choice of what geometric variables will be allowed to ''float.'' Sun and Gupta (62) examined computationally the effect of including the extensional viscosity in the coat-hanger die flow of Dow LDPE 132i. They used the Sarkar–Gupta model (63), whose four rheological parameters were evaluated from entrance pressure measurements. They found that the inclusion of the elongational viscosity has only a minor influence on the velocity field at the die exit, but that it increased the die lip pressure drop by 10–15%, with subsequent increases in the viscous energy dissipation and flow nonisothermicities.

Multilayer flat films and sheets can be formed by coextrusion, consisting of two layers (AB), three (such as ABA), five (such as ABCBA), and up to eleven layers. Each layer and particular multilayer configuration is selected for its contribution to one or more film/sheet product properties, such as gas barrier, adhesion, abrasion, and chemical resistance.

There are two basic methods of producing multilayer films and sheets, both using more than one extruder. The first uses a *multimanifold die*, where the different layers are separately distributed along the full width before being merged to form the multilayer just upstream from the die lips; although expensive, such coextrusion systems can accommodate polymers with very different rheological behaviors. The second uses a *single manifold* being fed by a *feed-port* system, as shown schematically in Fig. 12.30. The specific multilayer assembling is created by the feed block.

There are two important multilayer flow instability phenomena. The first is an interface that changes, migrating spatially and progressively downstream in both the x and y directions, as shown in Fig. 12.31. It has been established that this instability becomes more pronounced with increasing viscosity ratios (64). The second manifests itself with the onset of wavelike irregularities at the interface, which, because of the prevailing periodicity of below 1 μm, result in loss of see-through optical clarity (65).

Schrenk et al. (66) were among the first to report and study this interfacial instability, which they attributed to exceeding a critical value of interfacial shear stress. This criterion
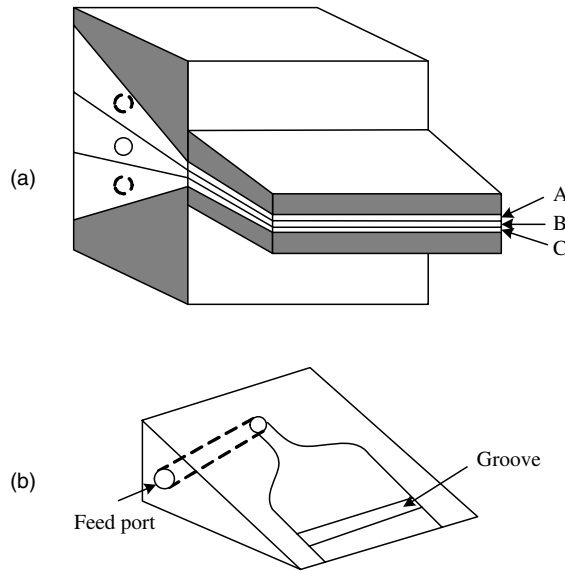
Fig. 12.30 Schematic showing the velocity profile in the three-layer coextrusion through a rectangular channel. [Reprinted by permission from C. D. Han, *Multiphase Flow in Polymer Processing*, Academic Press, New York, 1981.]

is akin to the critical wall shear stress at the onset of melt fracture. Mavridis and Shroff (65) on the other hand have shown that the adjacent layers' *difference* of the ''recoverable shear'' (67), that is, a difference in their elasticity, is also important and, quite possibly, controlling. Thus, this instability is a concern in the *die lip region* of multilayer flow, where the shear stress and elasticity levels are very high at the prevailing production rates.

We present briefly the two polymer melt coextrusion flow in the die lip region, following Han (64), without any of the instabilities just discussed. This flow region is
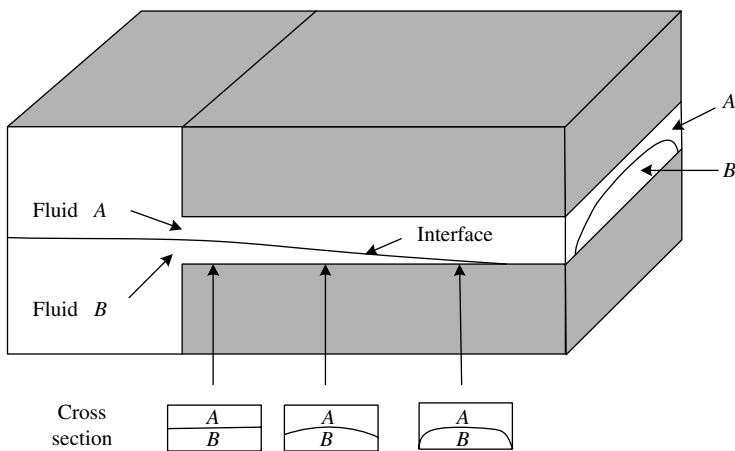

Fig. 12.31 Schematic showing the phase interface, which changes progressively as two polymer melts flow, side by side, through a rectangular channel. [Reprinted by permission from C. D. Han, *Multiphase Flow in Polymer Processing*, Academic Press, New York, 1981.]
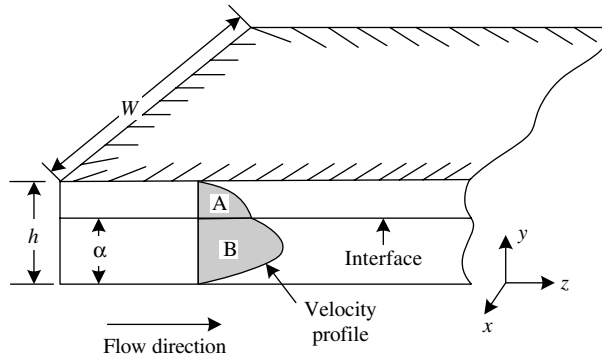
Fig. 12.32 Schematic showing the velocity profile in the two-layer coextrusion through a rectangular channel. [Reprinted by permission from C. D. Han, *Multiphase Flow in Polymer Processing*, Academic Press, New York, [1981.]

shown in Fig. 12.32. For a steady, isothermal flow of two Power Law fluids, A and B, floating in the die-lip region, where $h \ll W$, also known as a Hele–Shaw flow, there is only one velocity component $v_z = f(y)$, thus,

$$-\partial P/\partial z + \partial \tau_{yz}/\partial y = 0 \qquad (12.3\text{-}13)$$

Integrating gives for phase A

$$\tau_{yz,A} = -\zeta(y - \lambda), \quad 0 \le y \le \alpha \qquad (12.3\text{-}14)$$

and, for phase B

$$\tau_{yz,B} = -\zeta(y - \lambda), \quad \alpha \le y \le h \qquad (12.3\text{-}15)$$

in which ζ is the pressure gradient defined by

$$\zeta = -\partial P_A/\partial z = -\partial P_B/\partial z = \text{const.} \qquad (12.3\text{-}16)$$

Note that Eq. 12.3-14 implies that the pressure gradients in both phases are the same. This was verified experimentally by Yu and Han (68). Note further that λ is an integration constant, which corresponds to the position at which the maximum in velocity (and hence, the minimum in shear stress) occurs.

In order to obtain the velocity profile and then to calculate the volumetric flow rate, we use

$$\tau_{yz,\,A} = m_A \dot{\gamma}^{n_A} \qquad (12.3\text{-}17)$$

where m_A and n_A are the Power Law constants for phase A, and $\dot{\gamma}$ is the velocity gradient defined as

$$\dot{\gamma} = \left| \frac{dv_{z,A}}{dy} \right| \quad 0 \le y \le \alpha \qquad (12.3\text{-}18)$$

Similarly, for phase B we have

$$\tau_{yz,B} = m_B \dot{\gamma}^{n_B} \qquad (12.3\text{-}19)$$

where m_B and n_B are the Power Law constants for phase B, and $\dot{\gamma}$ is the velocity gradient defined by

$$\dot{\gamma} = \left| \frac{dv_{z,B}}{dy} \right| \qquad \alpha \le y \le h \qquad (12.3\text{-}20)$$

Now, combining Eqs. 12.3-14 and 12.3-17 and integrating the resulting expression, we obtain

$$v_{z,A} = \left(\frac{\zeta}{m_A} \right)^{s_A} \left(\frac{1}{s_A + 1} \right) \left\{ \lambda^{s_A+1} - |\lambda - y|^{s_A+1} \right\} \qquad 0 \le y \le \alpha \qquad (12.3\text{-}21)$$

Similarly, combining Eqs. 12.3-15 and 12.3-19 and integrating the resulting expression, we obtain

$$v_{z,B} = \left(\frac{\zeta}{m_B} \right)^{s_B} \left(\frac{1}{s_B + 1} \right) \left\{ (h - \lambda)^{s_B+1} - (y - \lambda)^{s_B+1} \right\} \qquad \alpha \le y \le h \qquad (12.3\text{-}22)$$

where

$$s_A = 1/n_A \quad s_B = 1/n_B \qquad (12.3\text{-}23)$$

It should be noted that Eqs. 12.3-21 and 12.3-22 contain a constant λ, yet to be determined with the aid of the boundary condition:

$$\text{at } y = \alpha, \quad \tau_{yz,A} = \tau_{yz,B} \qquad (12.3\text{-}24)$$

That is, the equation

$$
\begin{aligned}
\left(\frac{\zeta}{m_A} \right)^{s_A} & \left(\frac{1}{s_A + 1} \right) \left\{ \lambda^{s_A+1} - |\lambda - \alpha| s^{\alpha_A+1} \right\} \\
&= \left(\frac{\zeta}{m_B} \right)^{s_B} \left(\frac{1}{s_B + 1} \right) \left\{ (h - \lambda)^{s_B+1} - (\alpha - \lambda)^{s_B+1} \right\}
\end{aligned}
\qquad (12.3\text{-}25)
$$

must be solved for λ. The solution of Eq. 12.3-25 requires a trial-and-error procedure, using some kind of successive iteration scheme. Note, however, that in determining the parameter λ from Eq. 12.3-25, the interface position (see Fig. 12.32) has to be specified.

The volumetric flow rates, Q_A and Q_B, can be obtained from:

$$Q_A = w \left(\frac{\zeta}{m_A} \right)^{s_A} \left(\frac{1}{s_A + 1} \right) \left\{ \lambda^{s_A+1} \alpha - \frac{\lambda^{s_A+2}}{s_A + 2} - \frac{(\alpha - \lambda)^{s_A+2}}{s_A + 2} \right\} \qquad (12.3\text{-}26)$$

$$Q_B = w \left(\frac{\zeta}{m_B} \right)^{s_B} \left(\frac{1}{s_B + 1} \right) \left\{ (h - \lambda)^{s_B+1} (h - \alpha) - \frac{(h - \lambda)^{s_B+2}}{s_B + 2} + \frac{(\alpha - \lambda)^{s_B+2}}{s_B + 2} \right\} \qquad (12.3\text{-}27)$$
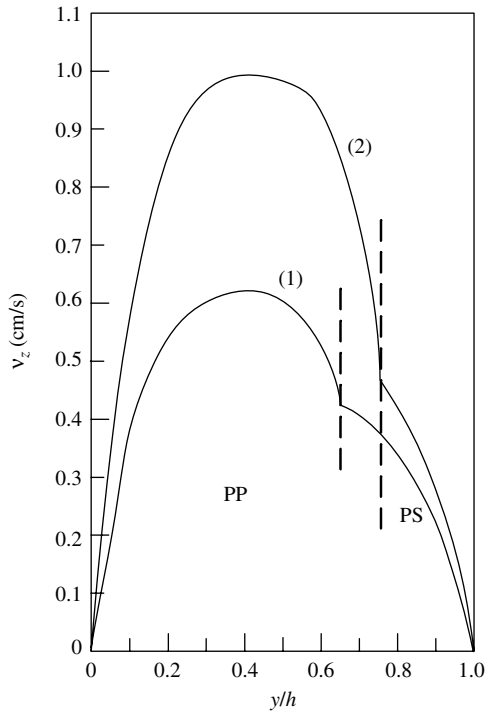
Fig. 12.33 Theoretically predicted velocity profiles in the two-layer (PP/PS) coextrusion through a rectangular channel: (1) $-\partial P/\partial z = 2.46 \times 10^7$ N/m^3; $Q = 19.8$ cm^3/min; (2) $-\partial P/\partial z = 2.74 \times 10^7$ N/m^3; $Q = 26.9$ cm^3/min; The Power Law constants used are, for PP: $m = 0.724 \times 10^4$ N s^n/ m^2, $n = 0.451$; and, for PS: $m = 2.127 \times 10^4$ N s^n/m^2, $n = 0.301$. [Reprinted by permission from C. D. Han, *Multiphase Flow in Polymer Processing*, Academic Press, New York, 1981.]

Figure 12.33 gives velocity profiles for the PP/PS system, which were obtained with the aid of Eqs. 12.3-21 and 12.3-22, using volumetric flow rates and pressure gradients determined experimentally in a rectangular channel. Figure 12.34 gives plots of viscosity versus shear stress for the PP and PS employed. It is seen that the polymer melts obey a Power Law model for $\dot{\gamma} > 10$ s^{-1}.

It should be pointed out that, in computing velocity profiles such as those given in Fig. 12.30, one needs information about the position of interface α (i.e., the relative layer thickness) in the die. Yu and Han (68) used computed values of the volumetric flow ratio, Q_A/Q_B, as a guide for determining the values of α by comparing them with the experimentally determined values of Q_A/Q_B. Note that Eqs. 12.3-26 and 12.3-27 yield.

$$\frac{Q_A}{Q_B} = \frac{(\zeta/m_A)^{s_A}}{(\zeta/m_B)^{s_B}} \left(\frac{s_B + 1}{s_A + 1}\right)$$
$$\left\{ \frac{\lambda^{s_A+1}\alpha - \left[\lambda^{s_A+2}/(s_A + 2)\right] - \left[(\alpha - \lambda)^{s_A+2}/(s_A + 2)\right]}{(h - \lambda)^{s_B+1}(h - \alpha) - \left[(h - \lambda)^{s_B+2}/(s_B + 2)\right] + \left[(\alpha - \lambda)^{s_B+2}/(s_B + 2)\right]} \right\} \tag{12.3-28}$$

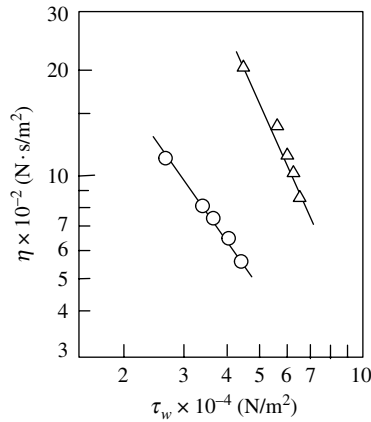**Fig. 12.34** Viscosity versus shear stress for the polymers ($T = 200°C$) used in the computations that yielded the velocity profiles given in Fig. 12.30: ($\triangle$) PS; ($\bigcirc$) PP. [Reprinted by permission from C. D. Han, *Multiphase Flow in Polymer Processing*, Academic Press, New York, 1981.]

It is seen that the volumetric flow ratio Q_A/Q_B is not equal to the layer thickness ratio $\alpha/(h - \alpha)$ as one might expect. Q_A/Q_B is a complicated function that depends on the pressure gradient ζ, the Power Law constants of each phase (n_A, m_A, n_B, and m_B), and the parameters α and λ. Therefore, for a given fluid system and flow conditions, where the pressure gradient ζ and flow rates (Q_A and Q_B) are specified, the interface position α can be determined from Eq. 12.3-28, when the predicted value of Q_A/Q_B agrees with the experimentally determined one, provided Eq. 12.3-25 is satisfied. In other words, Eqs. 12.3-25 and 12.3-28 can be used for determining values of α and λ.

We now turn to the treatment of the die lip coextrusion analysis of Mavridis and Shroff (65). Their analysis treats the flow of an arbitrary number of layers of melts that are viscoelastic, flowing in a one-dimensional nonisothermal flow, shown in Fig. 12.35 and
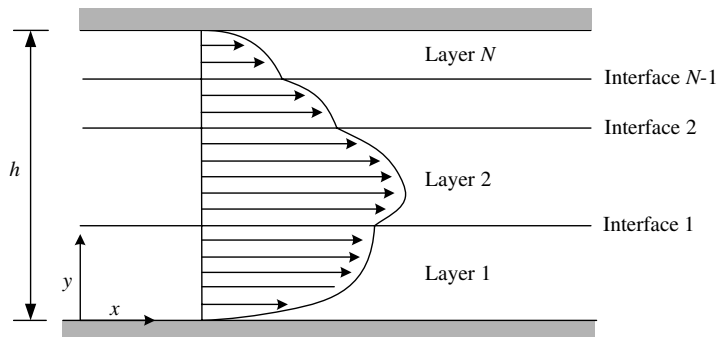

Fig. 12.35 Schematic of flow geometry in *N*-layer coextrusion.

described as follows:

$$Q_i = \int_{l_{i-1}}^{l_1} v_z\, dy \qquad i = 1, \cdots, N \tag{12.3-29}$$

$$\tau_{zy} = \left(-\frac{\partial P}{\partial z}\right)(y - y_{\max}) \tag{12.3-30}$$

$$\rho C_p v_z \frac{\partial T}{\partial z} = k\frac{\partial^2 T}{\partial y^2} + \eta \dot{\gamma}^2 \tag{12.3-31}$$

These equations are solved numerically under the assumptions of velocity, shear stress, and temperature continuity at all interfaces. They use the Sabia 4-parameter viscosity model (69), because of its ability to include the Newtonian plateau viscosity, which is important for multilayer extrusion, because of the existence of low shear-rate viscosities at the interfaces.

$$\ln\left(\frac{\eta}{\eta_0}\right) = \left(\frac{\eta}{\eta_0} - A\right)\ln\left[1 + \left(\frac{\dot{\gamma}}{\dot{\gamma}_0}\right)^B\right] \tag{12.3-32}$$

where the parameters η and η_0 are both temperature dependent. Furthermore, in order to explore the role of the melt elasticity of adjacent layers to the wavelike interfacial disturbances, they evaluated the discreet relaxation spectra, back-calculated from dynamic measurements. They then used the Leonov Model (70) to obtain the shear stress

$$\tau_{12}(\dot{\gamma}) = 2\sum_i G_i \frac{\lambda_i \dot{\gamma}}{1 + X_i} \tag{12.3-33}$$

and first normal stress difference

$$\tau_{11} - \tau_{22} = \sqrt{2}\sum_i G_i \frac{X_i - 1}{(1 + X_i)^{1/2}} \tag{12.3-34}$$

where

$$X_i = \left(1 + 4\lambda_i^2 \dot{\gamma}^2\right)^{1/2} \tag{12.3-35}$$

Finally, they calculated the recoverable strain of each of the polymers used, and the difference between two adjacent layers, ΔS_R, that is, the difference in their elasticity

$$\Delta S_R = S_{R,A} - S_{R,B} = \left(\frac{\tau_{11} - \tau_{22}}{2\tau_{12}}\right)_A - \left(\frac{\tau_{11} - \tau_{22}}{2\tau_{12}}\right)_B \tag{12.3-36}$$

Three polymers were used: one grade of polyester and two grades of EVA. Furthermore, two three-layer systems were investigated: 5% polyester–90% EVA$_1$–5% Polyester, and 5% polyester–90% EVA$_2$–5% polyester. The viscosity $\eta(\dot{\gamma})$ and first normal stress
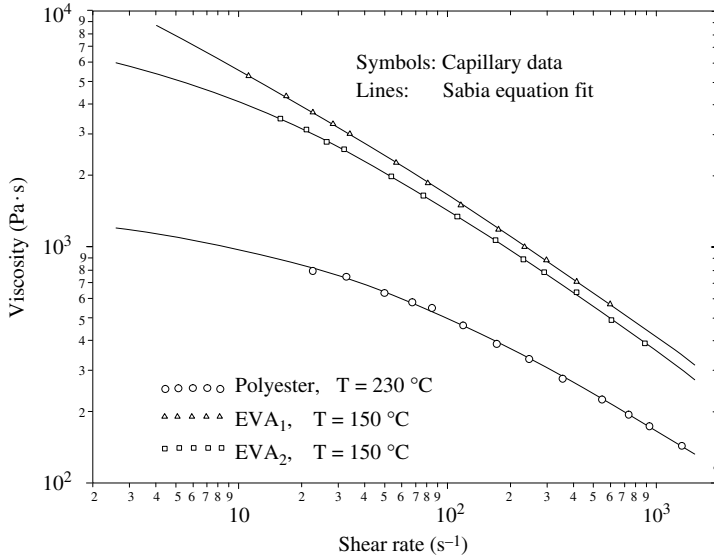
Fig. 12.36 Capillary viscosity data and Sabia equation fit. [Reprinted by permission from H. Mavridis and R. N. Shroff, ''Multilayer Extrusion: Experiments and Computer Simulation,'' *Polym. Eng. Sci.*, **34**, 559 (1994).]

difference $(\tau_{11} - \tau_{22})(\dot{\gamma}^2)$ of the three polymers are shown in Fig. 12.36 and Fig. 12.37. The polyester is the least viscous and least elastic of the three polymers used, and EVA_1 is more viscous and elastic than EVA_2. Three experiments were conducted with EVA_1 and three with EVA_2 at conditions that result in different interfacial stresses, with their
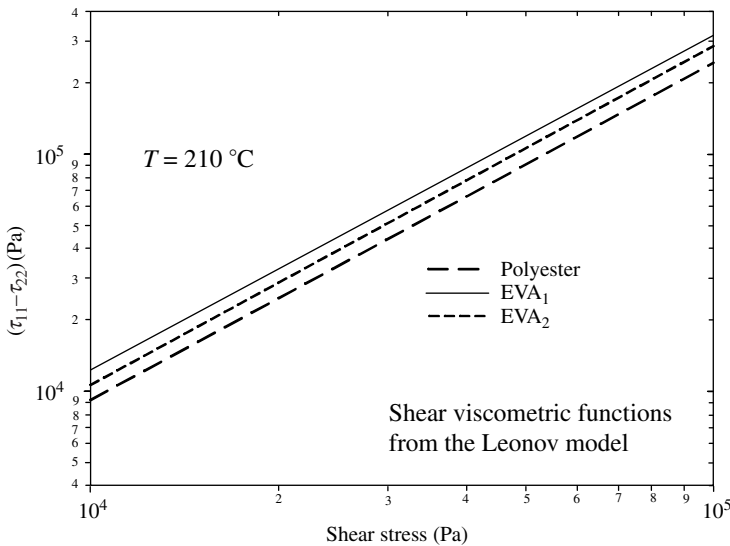

Fig. 12.37 First normal stress difference vs. shear stress, as predicted by the Leonov model. [Reprinted by permission from H. Mavridis and R. N. Shroff, ''Multilayer Extrusion: Experiments and Computer Simulation,'' *Polym. Eng. Sci.*, **34**, 559 (1994).]

Shear stress (KPa)

Fig. 12.38 Predicted interfacial shear stress at the polyester/EVA interface. [Reprinted by permission from H. Mavridis and R. N. Shroff, ''Multilayer Extrusion: Experiments and Computer Simulation,'' *Polym. Eng. Sci.*, **34**, 559 (1994).]
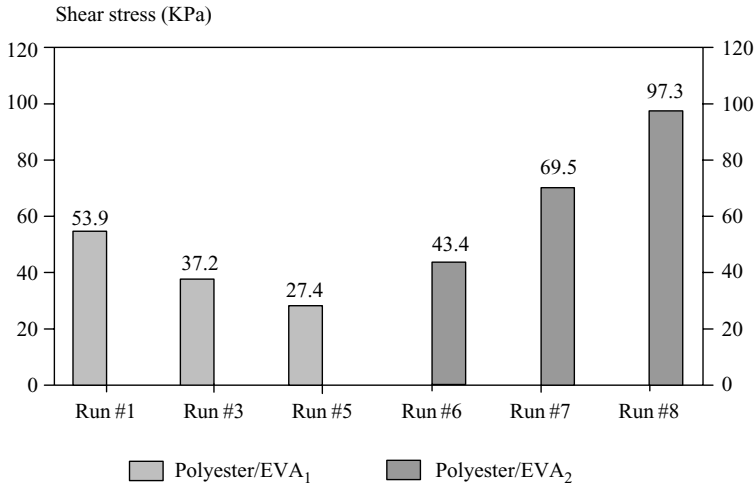
calculated values shown in Fig. 12.38. Also, Fig. 12.39 shows the ΔS_R values at the interface for all experiments.

As mentioned previously, the ''see-through'' clarity of the coextruded films deteriorates with the presence and extent of the wavelike interfacial instability. Quantitative
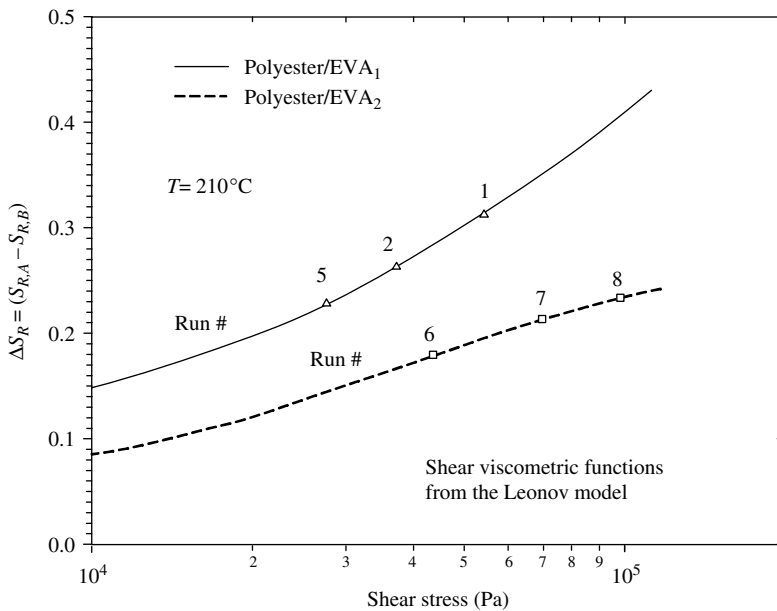

Fig. 12.39 Difference in stress ratio vs. interfacial shear stress, for polyester/EVA$_1$ (solid line) and polyester/EVA$_2$ (dashed line). [Reprinted by permission from H. Mavridis and R. N. Shroff, ''Multilayer Extrusion: Experiments and Computer Simulation,'' *Polym. Eng. Sci.*, **34**, 559 (1994).]

NALS (polyester/EVA$_1$)　　　　　　　NALS (polyester/EVA$_2$)

Fig. 12.40 Narrow angle scattering measurements of the coextruded films. [Reprinted by permission from H. Mavridis and R. N. Shroff, "Multilayer Extrusion: Experiments and Computer Simulation," *Polym. Eng. Sci.*, **34**, 559 (1994).]
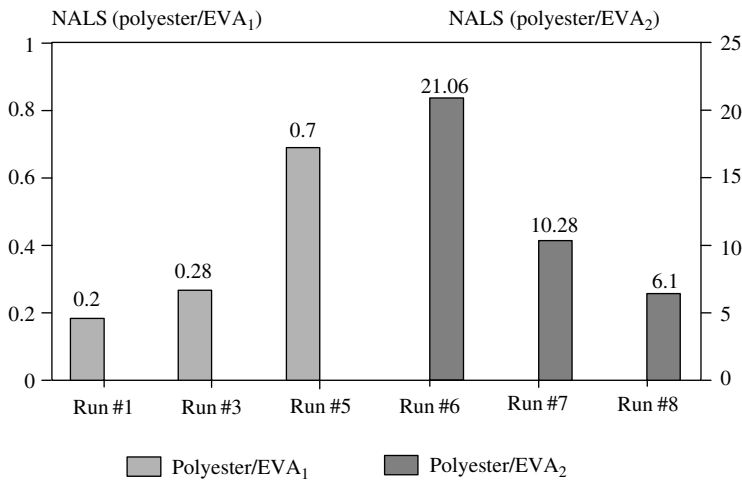
measures for see-through clarity are obtained with narrow-angle light-scattering (NALS) measurements of the transmittance of light through the film (ASTM D-1746). NALS values for all the experiments are shown in Fig. 12.40, with 100 denoting perfect clarity.

The NALS ratings of all the EVA$_1$ films are an order of magnitude lower than those with EVA$_2$. This cannot be explained by the Schrenk (66) criterion of a critical interfacial shear stress, as we see in Fig. 12.38. On the other hand, the differences of the recoverable strain values at the interface between polyester/EVA$_1$ and polyester/EVA$_2$ shown in Fig. 12.39 correlate better with the obtained NALS results: the higher the ΔS_R, that is, the larger the melt elasticity difference between polyester and EVA, the more severe the interfacial instability. In other words, the work of Maviridis and Shroff suggests that the instability is elastic in nature. Such insight would allow for the reduction of the instability through the in-line reactive extrusion long chain branching modification of the polyester melt, which will increase its elasticity, S_R.

The flat film and sheet coextrusion analyses mentioned earlier can be easily extended to the treatments of the wire coating and film blowing coextrusion processes.

12.4 TUBE, BLOWN FILM, AND PARISON FORMING

Plastic tube and tubular films are formed continuously by extruding a polymer through an annular die. The annular flow channel is formed by the outer die body and the die mandrel. A number of annular die designs are currently employed. In the first, the mandrel is supported mechanically onto the outer die body by a number of "fins" called "spider legs"; Fig. 12.41 illustrates this type of die. The flow is axisymmetric, and the only serious problem encountered in the cross-machine direction uniformity of the extruded product is that of "weld" lines and streaks caused by the presence of the spider legs, which split the flow.
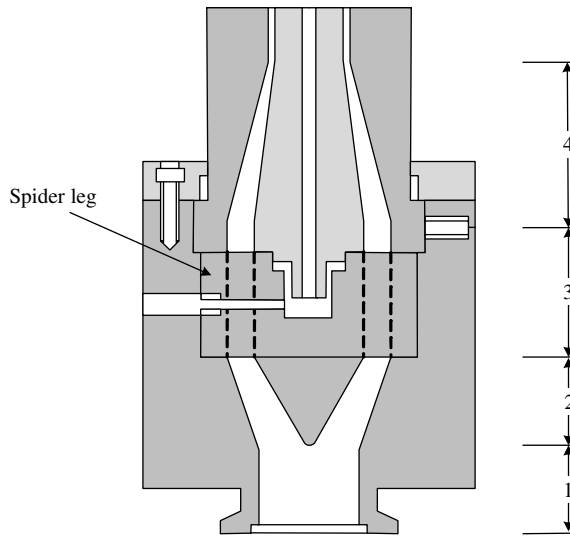
Fig. 12.41   Typical spider-type tube or blown film die.

Even though these obstacles are far away from the die lip region, the polymer melt, at normal extrusion speeds, is unable to "heal" completely. That is, the macromolecules comprising the two layers that were split by the spider legs do not establish the entanglement level characteristic of the bulk at the prevailing shear rate and temperature.

This is another ramification of incomplete response of polymers, because the "experimental time" is smaller than the relaxation time of the system of macromolecules. As expected, weld lines are mechanically weak and have optical properties that differ from those of the bulk, making them visible. Furthermore, they result in film or tube gauge nonuniformities, probably because of the different degree of swelling of the melt in the neighborhood of the weld line. They also induce cross-machine pressure nonuniformities. To overcome these problems, basic cross-head die designs (Fig. 12.42) have been devised in which the mandrel is mechanically attached to the die body in such a way that obstacles are not presented to the flow in the annular region.

Unlike the coat hanger flat film dies, no simple final film adjustment is possible by lip flexing. Consequently, the order of magnitude of thickness accuracy in tubular dies is $\pm 10\%$ as compared to $\pm 5\%$ in flat sheet and film dies. This larger margin of accuracy in blown film dies is compensated by die rotation, which permits the distribution of the thickness variation across the entire width of the product.

For flow simulation in spiral mandrel dies, software simulation packages (e.g., SPIRALCAD$^{(TM)}$ by Polydynamics, Inc.) are used. The molten polymer flow is simulated from the die ports as it moves along and leaks from the spiral channels in the gap between the body and the mandrel. It predicts the flow, pressure, and temperature distributions throughout the die and the thickness variation in the final annular extruded film. Regions of heavy or light gauge film can easily be identified and design modifications made accordingly.

In the cross-head type of dies, the melt is split at the inlet to the manifold and recombines 180° from the inlet. Moreover, the flow is not axisymmetric, and fluid particles flowing around the mandrel have a longer distance to travel than those that do not.
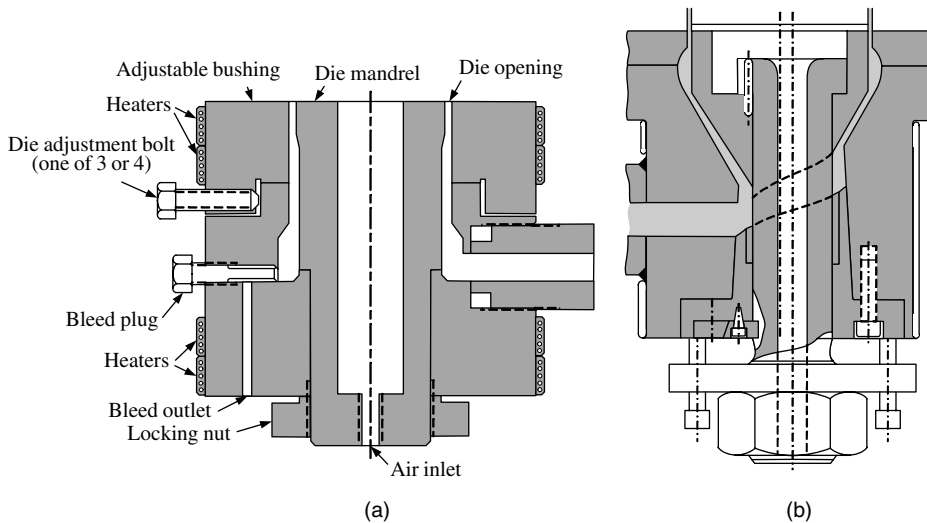
Fig. 12.42 Schematic representation of tubular dies. (a) Side-fed manifold die. (b) Blown-film die.

Consequently, if the die gap were uniform, the flow rate 180° away from the die entrance would be smaller, resulting in nonuniform thickness.

There are a number of ways to reduce this nonuniformity. The mandrel can be placed eccentrically in the die, allowing for a wider gap at the remote end from the lead port. Such a design can, in principle, provide uniform flow rate, but shear rate and temperature histories will remain nonuniform. In another solution [Fig. l2.42(b)], an insert directs the flow at the far end upward, reducing the flow length around the mandrel and eliminating slow flow (stagnant) regions. In addition, the mandrel is also eccentric.

Finally, Fig. 12.43 shows a spiral mandrel die, currently in common use for film blowing, which allows greater design flexibility in obtaining a uniform flow rate, uniform shear rate and temperature histories, and elimination of weld lines. The feed is distributed into separate flow tubes called *feed ports*. Each of these ports feeds the polymer in a spiral groove cut into the mandrel. The spiral decreases in cross-sectional area, whereas the gap between the mandrel and the die increases toward the exit. The result is a mixing or ''layering'' of melt originating from the various ports.

Tubes and blown films can be produced as multilayer structures by employing multiple extruders and coextrusion manifolds and dies. Figure 12.44 is a schematic representative of a conventional and new spiral coextrusion die. The designs can be used for both blown-film and blown-molding parison dies. In the extrusion of tubes, such as rigid PVC or PE pipe, the extrudate passes over a water-cooled mandrel and enters a cold-water bath whose length depends on the tube thickness; the tube leaves the bath well below its T_m (if it is crystalline) or T_g (if it is amorphous) and is sectioned to the desired lengths.

Next we discuss the problem of estimating the total pressure drop in tubular dies, and we trace the development of the die design equation.

Estimation of Pressure Drop in Tubular Dies

We know that the tubular die flow channel is composed of a series of more or less annular flow regions, which are straight, tapering, of almost uniform cross section, or interrupted
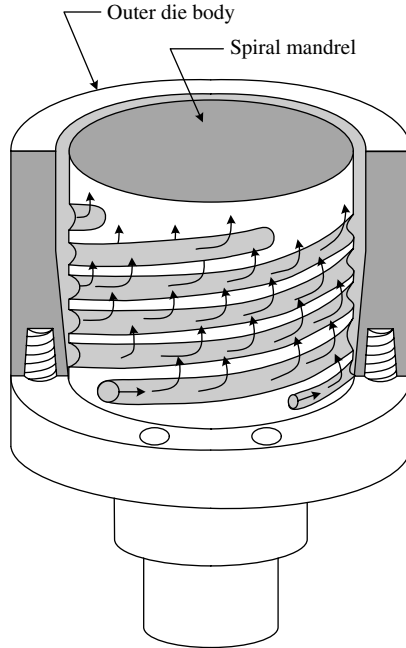
Fig. 12.43   Schematic representation of a spiral mandrel die.

by obstacles. Thus, although exact solutions of the flow in them may require numerical methods, we can arrive at a number of useful and simple engineering expressions by examining the steady isothermal flow between two straight concentric cylinders of constant radii R_o and R_i.
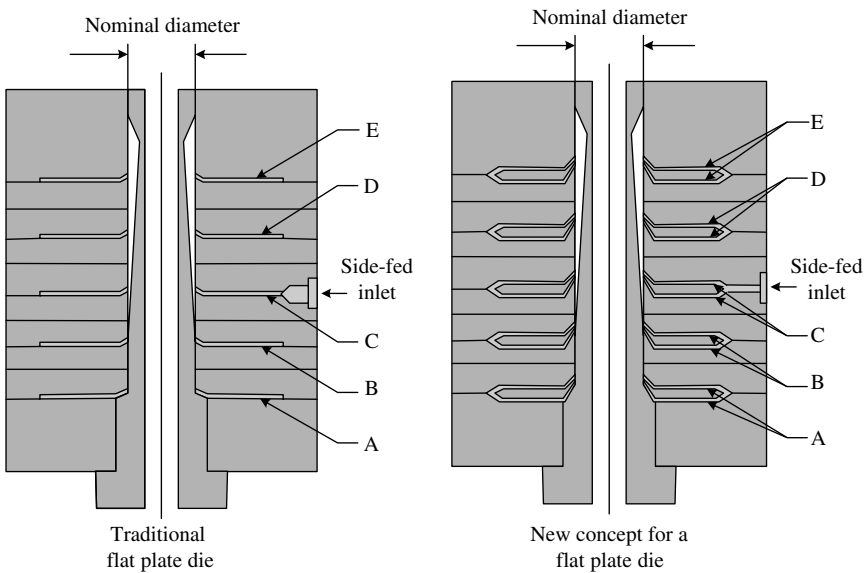

Fig. 12.44   Schematic representation of multilayer extrusion dies.

Consider the annular flow region $R_i \leq r \leq R_o$, $0 \leq z \leq L$, and $0 \leq \theta \leq 2\pi$. An incompressible Power Law fluid is flowing under steady and isothermal conditions because of the pressure drop $\Delta P = P_0 - P_L$. The flow is assumed to be fully developed. Under these assumptions the z-component momentum equation becomes

$$\frac{dP}{dz} = -\frac{1}{r}\frac{d}{dr}(r\tau_{rz}) \tag{12.4-1}$$

When Eq. 12.4-1 is coupled with the Power Law constitutive equation for this flow

$$\tau_{rz} = -m\left|\frac{dv_z}{dr}\right|^{n-1}\left(\frac{\partial v_z}{\partial r}\right) \tag{12.4-2}$$

the following expression is obtained

$$\left(\frac{r}{m}\right)\frac{dP}{dz} = \frac{d}{dr}\left(r\left|\frac{dv_z}{dr}\right|^{n-1}\frac{dv_z}{dr}\right) \tag{12.4-3}$$

Let $r*$ be the radial position where the velocity is maximum; that is, $dv_z/dr = 0$. Then in region I, $R_i \leq r \leq r^*$, $dv_z^{I}/dr \geq 0$, and Eq. 12.4-3 becomes

$$\left(\frac{r}{m}\right)\frac{dP}{dz} = \frac{d}{dr}\left[r\left(\frac{dv_z^{I}}{dr}\right)^n\right] \tag{12.4-4}$$

where $v_z^{I}(r)$ is the velocity in this region. The accompanying boundary conditions are $v_z^{I}(R_i) = 0$ and $dv_z^{I}/dr = 0$ at $r = r^*$. Similarly, in region II, $r^* \leq r \leq R_O$, $dv_z^{II}/dr \leq 0$, and Eq. 12.4-3 becomes

$$\left(\frac{r}{m}\right)\frac{dP}{dz} = -\frac{d}{dr}\left[r\left(-\frac{dv_z^{II}}{dr}\right)^n\right] \tag{12.4-5}$$

having the following boundary conditions: $v_z^{II}(R_o) = 0$ and $dv_z^{II}/dr = 0$ at $r = r^*$. Equations 12.4-4 and 12.4-5 can be directly integrated with the foregoing boundary conditions, and the location r^* can be obtained by setting $v_z^{I}(r^*) = v_z^{II}(r^*)$. This problem was solved by Fredrickson and Bird (71), and the resulting flow rate–pressure drop relationship is

$$Q = \left(\frac{\pi R_o^3}{s+2}\right)\left[\frac{R_o\Delta P}{2mL}\right]^s\left(\frac{\beta-1}{\beta}\right)^{2+s}F(n,\beta) \tag{12.4-6}$$

where $\beta = R_o/R_i$ and $F(n,\beta)$ is the shear dependency and geometry-dependent function appearing in Fig. 12.45.

For values of $0.4 \leq R_i/R_o \leq 1.0$, which represent relatively narrow annuli, the function F becomes independent of the degree of shear thinning of the melt. At the limit $\beta \to 1.0$, Table 12.2 can be used to relate the volumetric flow rate to the axial pressure drop, since the geometrical situation corresponds to the flow between parallel plates.
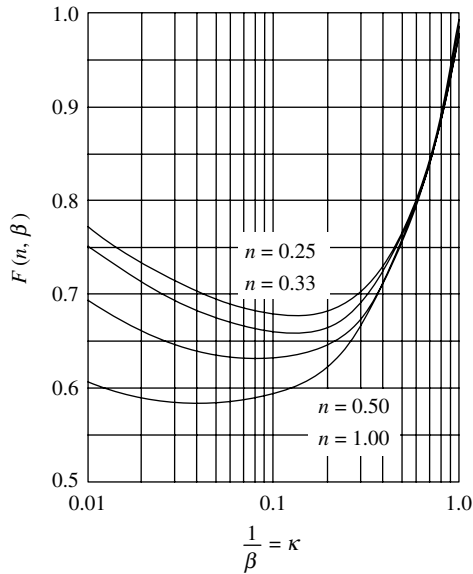
Fig. 12.45 The function $F(n, \beta)$ for the flow of Power Law fluids in an annular region. [Reprinted by permission from A. G. Fredrickson and R. B. Bird, "Non Newtonian Flow in Annuli," *Ind. Eng. Chem.*, **50**, 347(1958).]

In this case

$$Q = \left(\frac{\pi R_o^3}{s+2}\right)\left[\frac{R_o \Delta P}{2mL}\right]^s \left(\frac{\beta-1}{\beta}\right)^{2+s}\left(\frac{1+\beta}{2\beta}\right) \tag{12.4-7}$$

where in Table 12.2 $W = \pi(R_i + R_o)$. Thus, the pressure drop in straight concentric annular sections of tubular dies can be obtained fairly easily using Eq. 12.4-6 with the help of Fig. 12.40, or with Eq. 12.4-7 for very narrow annuli.

It should be recalled that, in annular pressure flows, as in all pressure flows, an error is introduced by using the Power Law model fluid because of inaccuracies in the low shear rate regions. Moreover, the assumption of isothermicity also introduces errors and can lead to an overestimation of $P_0 - P_L$.

Cox and Macosko (19) have measured increases in melt surface temperature of the order of $10°$–$20°$C with LDPE flowing in an $L = 0.1$ m, $R_i/R_o = 0.5$ annulus at 190°C, and Newtonian wall shear rates of about $200\,\mathrm{s}^{-1}$. Such temperature increases would reduce the melt viscosity, especially near the exit of the annulus.

For tapering annular flow channels (regions 2 and 4 of the spider-type die in Fig. 12.41), we can calculate the pressure drop by making the lubrication approximation and using either Eq. 12.4-6 or Eq. 12.4-7, depending on the width of the annulus. In both cases, $\beta = \beta(z)$ and $H = H(z)$. We can use values of β and H that are averaged over the entire length, or we can solve Eq. 12.4-6 or Eq. 12.4-7 over small axial length increments ΔL_i, with corresponding β_i or H_i, then summing up the partial pressure drops. For thin tapered annuli, which can be represented by two almost parallel plates, one can use the Reynolds lubrication equation (Eq. 2.11-11).

In converging or diverging sections of annular dies, the fluid elements are subjected to axial and radial accelerations. Neglecting the radial special accelerations (for small tapers), the z-component equation of motion reduces to

$$\rho v_z \frac{\partial v_z}{\partial z} = -\frac{dP}{dz} - \left[\frac{1}{r}\frac{\partial}{\partial r}(r\tau_{rz}) + \frac{\partial \tau_{zz}}{\partial z}\right] \qquad (12.4\text{-}8)$$

For very viscous fluids the inertial term $\rho v_z(\partial v_z/\partial z)$ is negligible, thus

$$\frac{dP}{dz} = -\frac{1}{r}\frac{\partial}{\partial r}(r\tau_{rz}) - \frac{\partial \tau_{zz}}{\partial z} \qquad (12.4\text{-}9)$$

For converging channels the first term on the right-hand side of Eq. 12.4-9 increases with increasing axial distance, and because of this, dP/dz is not a constant but is z-dependent. For a viscous fluid, the value of $\partial \tau_{zz}/\partial z$ is given by the relation

$$\tau_{zz} = -\bar{\eta}\frac{\partial v_z}{\partial z} \qquad (12.4\text{-}10)$$

A value for $\partial v_z/\partial z$ averaged over the spacing H can be used for approximate calculations. This quantity, since $q = \bar{v}_z(z)H(z)$, is

$$\frac{\partial \bar{v}_z}{\partial z} \cong \frac{\partial}{\partial z}\left(\frac{q}{H(z)}\right) = \frac{\partial}{\partial z}\left(\frac{q}{H_0 - Az}\right) = -\frac{Aq}{(H_0 - Az)^2} \qquad (12.4\text{-}11)$$

where A is the taper. Considering the result of the preceding equation, as well as Eq. 12.4-10, we conclude that the contribution of the second term of the right-hand side of Eq. 12.4-9 is never zero for tapered channels. For more exact calculations, the dependence of $\partial v_z/\partial z$ on the thickness direction must be taken into account.

Worth and Parnaby (72) have considered the contribution of the elasticity of the polymer melt G to the term τ_{zz}. Using a Maxwell-type constitutive equation (Eq. 3.3-9), they find

$$\tau_{zz} - \tau_{rr} \cong \tau_{zz} = \frac{\tau_{rz}^2}{G} \qquad (12.4\text{-}12)$$

Since $\tau_{zz} = f(z)$ for tapered dies, $\partial \tau_{zz}/\partial z$ is nonzero. For reasonable taper values, they find these elastic forces to contribute less than 10% of the viscous pressure drop. They have also calculated the drag and pressure forces on the mandrel.

Turning to the cross-fed tubular dies, we note that, to develop die design expressions, we must model the two-dimensional flow in the z- and θ-directions. This is a task of considerable difficulty. Pearson (73) was the first to model the flow for narrow dies. The flow region was "flattened," and the two-dimensional flow in rectangular coordinates between two plates was considered. The plate separation was allowed to vary in the approach channel so that the resulting output is constant. The final die lip opening is constant, formed by the concentric cylinders.

The resulting design equations are complicated, and their solution is computationally demanding. Nevertheless, design expressions for both Newtonian and Power Law fluids in

isothermal flow can be obtained. Gutfinger, Broyer, and Tadmor (74) solved this problem using the flow analysis network (FAN) method discussed in Chapter 13. This approximate but relatively simple numerical method is particularly well suited for two-dimensional slow flow problems in narrow gaps. The results obtained with the FAN method are identical to those of Pearson, but they can be achieved with much less computational effort.

As mentioned earlier, there is an additional role that the approach and die lip regions must play. In these regions, the polymer melt must be given an opportunity to lose all its "memory" of the cross-flow, nonuniform strain history. Worth and Parnaby (72) call these regions the "relaxation zone," and by assuming that the melt responds as a simple linear viscoelastic Voigt fluid model, the authors calculate roughly the minimum length for a desired level of relaxation of the strains applied at the entrance.

It is worth noting that, although in principle tube and tubular blown film dies are similar, in practice they are quite different in function, size, and complexity. Blown film dies are much longer, have a very small die lip opening, and are subject to more stringent product uniformity criteria because there is no "sizing" equipment downstream. Furthermore, blown film products are almost exclusively LDPE, and occasionally HDPE and PP. On the other hand, HDPE and rigid and plasticized PVC are the common polymers for pipes and tubes.

12.5   WIRE COATING

Wire and cable coating dies are used in the extrusion process for primary insulation of single conducting wires as well as the jacketing or sheathing of a group of wires already insulated electrically, for mechanical strength and environmental protection purposes.

The bare wire is unwound, sometimes by a controlled tension device, and is preheated to a temperature above the T_g or T_m of the polymer to be extruded; this is done so that the layer next to the bare wire adheres to it, and to drive moisture or oils off the conductor surface. The wire is fed in the back of the cross-heat die and into a "guider tube." Upon exiting the guider, it meets the molten plastic, which covers it circumferentially. Since the wire speed, which is controlled by a capstan at the end of the line, is usually higher than the average melt velocity, a certain amount of "drawdown" is imposed on the melt anywhere from a value slightly greater than unity to 4.

After exiting the die, the coated wire is exposed to an air or gas flame for the purpose of surface annealing and melt relaxation, which also improves the coating gloss. It then enters a cooling trough, where the cooling medium is usually water. The length of the trough depends on the speed of the wire, the diameter of the wire or cable, and the insulation thickness; it increases with increasing level of these parameters. As expected, the cooling trough length is longer for crystalline polymers, since the crystallization process is exothermic. For undersea cables, cooling troughs not only provide for almost 300 ft of linear travel, but are also divided into several compartments containing water of successively cooler temperatures (typically of a total range 80°–100°C), to avoid fast cooling of the jacket surface, which could cause void formation or thermal stresses.[10]

---

10. Cross-linkable LDPE, used in insulating power cables, requires long residence in steam "curing tubes" 100–300 m long.
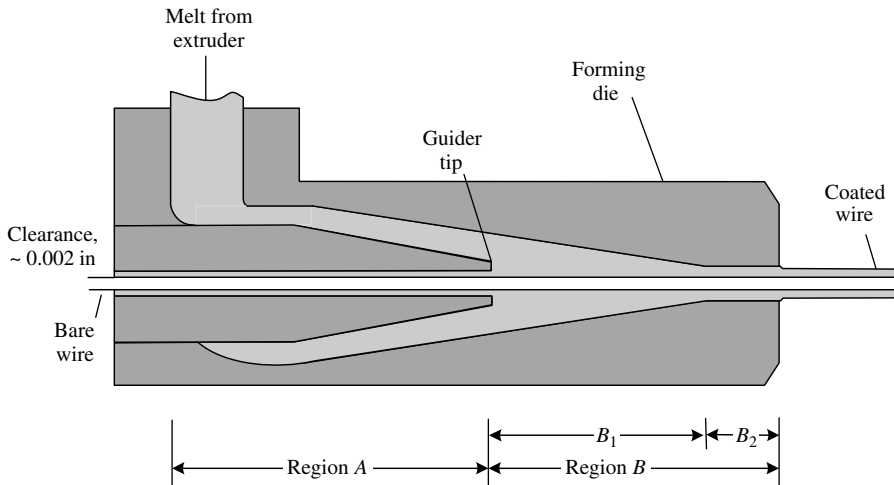
Fig. 12.46 Detailed schematic representation of the pressure type of wire-coating die.

Upon exiting the cooling trough, the wire passes over the capstan, where its tension is controlled and further cooling can be provided. It then passes through a capacitance-measuring device that detects flaws as well as thickness variations. These variations provide information for adjusting the pulling device speeds or the extruder screw speeds. Since defective wire is difficult to reprocess, because the product is a composite, the process is closely monitored. In addition, great care is taken to design the coating die properly.

Two types of cross-head dies are used for wire and cable coating. The first type is an annular flow or tubing die, where a thin-walled tube is extruded and the molten tube drawn onto the conductor by vacuum after it leaves the die. The vacuum is applied through the clearance between the conductor and the guide, which is usually of the order of 0.2 mm. Tubing dies are commonly used for jacketing cables or coating very thin wires with polymer melts that are very viscous.

The second type of cross-head die used is the ''pressure'' type, where the polymer melt contacts the conductor *inside* the die; Fig. 12.46 gives details of such a die. The clearance between the guide and the conductor must be quite small, of the order of 0.05 mm, because at the guide tip, the melt is under some pressure. This type of die is quite commonly used for wire coating. From a flow analysis point of view, the pressure die can be broken down into two regions, as in Fig. 12.46. The flow situation in region A is the same as that in the approach channel of side-fed tubular dies discussed in the previous section. Thus, making the lubrication approximation, the pressure drop in this region can be estimated using Eq. 12.4-6.

In region B, one of the containing walls is the conductor wire, which is moving with a high velocity *V*. Thus, the flow is both drag and pressure induced. In the streamline region B, the flow can be treated locally as a combined drag and pressure flow in an annulus of the local thickness (lubrication approximation). Such a flow truly exists in region B_2. Thus, solving the annular drag and pressure flow will help us in the analysis of the entire region B.

Example 12.3   The Absence of Melt Fracture in Wire Coating   Let us consider the question of why the wire coating process can operate at very high wire speeds and a shear rate of 10^4–10^5 s^{-1}, given the thin coating thicknesses, without the onset of melt fracture. Referring to the die lip region of the wire-coating die shown schematically below, consider the following specific process: $L = 10$ mm, $H = 1$ mm, $R_i = 0.5$ mm, a polymer with melt viscosity (constant) $\mu = 100$ Pa·s, melt density $\rho = 750$ kg/m^3, heat capacity of the melt $C_P = 2.33 \times 10^3$ J/(kg·K), pressure difference between the exit and the entrance $\Delta P = P_{\text{ent}} - P_{\text{atm}} = 0.1$ MPa, initial melt temperature $T_0 = 200\,°$C, activation energy: $\Delta E = 6$ kcal/mol $= 6 \times 4.1868$ kJ/mol, and the wire being pulled with a velocity $V = 1200$ m/min.

What will the resulting polymer coat thickness be, assuming that the solid density is 0.95 g/cc?

Solution   This flow is z-axisymmetric. We, thus, select a cylindrical coordinate system, and make the following simplifying assumptions: Newtonian and incompressible fluid with constant thermophysical properties; no slip at the wall of the orifice die; steady-state fully developed laminar flow; adiabatic boundaries; and negligible of heat conduction.

Thus:

$$q_r|_{r=R_i} = q_r|_{r=R_o} = 0 \quad \text{or} \quad \left.\frac{\partial T}{\partial r}\right|_{r=R_i} = \left.\frac{\partial T}{\partial r}\right|_{r=R_o} = 0 \qquad \text{(E12.3-1)}$$

The equation of continuity with the preceding assumptions gives $\partial v_z/\partial z = 0$.

The equation of motion in the cylindrical coordinates reduces to

$$\frac{\partial P}{\partial z} = -\frac{1}{r}\frac{\partial}{\partial r}\left(r\tau_{rz}\right) \qquad \text{(E12.3-2)}$$

where

$$\tau_{rz} = -\mu\frac{\partial v_z}{\partial r} \qquad \text{(E12.3-3)}$$
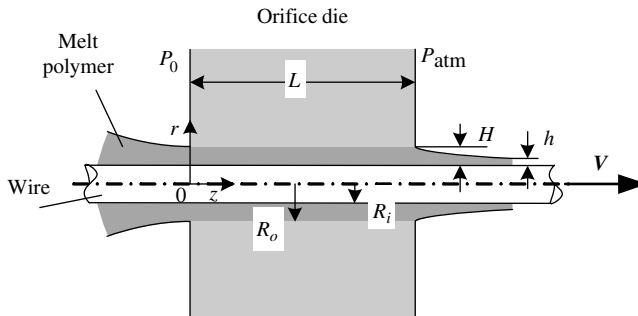

Fig. E12.3   A schematic of the die lip region of a wire coating die.

Equation E12.3-2 can be rewritten with $(\partial P/\partial z) = (\Delta P/L)$ as:

$$\frac{\Delta P}{L} = \frac{\mu}{r}\frac{\partial}{\partial r}\left(r\frac{\partial v_z}{\partial r}\right) \tag{E12.3-4}$$

Integrating Eq. E12.3-4 with respect to r in company with velocity boundary conditions of $v_z|_{r=R_i} = V$ and $v_z|_{r=R_o} = 0$ gives

$$v_z(\rho) = V + \left(\rho^2 - 1\right)\Psi V - \left[V + \left(\alpha^2 - 1\right)\Psi V\right]\frac{\ln\rho}{\ln\alpha} \tag{E12.3-5}$$

where $\rho = r/R_i$, $\alpha = R_o/R_i$ and the dimensionless parameter $\Psi = (R_i^2\Delta P)/(4\mu LV)$
   The equation of energy reduces to

$$\rho C_v \frac{\partial T}{\partial t} = \mu\left(\frac{\partial v_z}{\partial r}\right)^2 \tag{E12.3-6}$$

Making Eq. E12.3-6 dimensionless with new variables, $u = v_z/V$, $\rho = r/R_i$, and operators $\partial/\partial r = (1/R_i)(\partial/\partial\rho)$ results in,

$$\frac{\partial T}{\partial t} = \frac{\mu}{\rho C_v}\left(\frac{V}{R_i}\right)^2\left(\frac{\partial u}{\partial\rho}\right)^2 \tag{E12.3-7}$$

where

$$u(\rho) = 1 + \left(\rho^2 - 1\right)\Psi - \left[1 + \left(\alpha^2 - 1\right)\Psi\right]\frac{\ln\rho}{\ln\alpha} \tag{E12.3-8}$$

$$\frac{\partial u}{\partial\rho} = 2\rho\Psi - \left[1 + \left(\alpha^2 - 1\right)\Psi\right]\frac{1}{\rho\ln\alpha} \tag{E12.3-9}$$

$$\left(\frac{\partial u}{\partial\rho}\right)^2 = \left\{4\Psi^2\rho^2 - \left[\frac{4\Psi + 4(\alpha^2 - 1)\Psi^2}{\ln\alpha}\right] + \left[\frac{1 + (\alpha^2 - 1)\Psi}{\ln\alpha}\right]^2\frac{1}{\rho^2}\right\} \tag{E12.3-10}$$

Integrating Eq. E12.3-7 with respect to t can obtain the melt temperature profile of any point in the die, under the assumptions made

$$T - T_0 = \frac{\mu}{\rho C_v}\left(\frac{V}{R_i}\right)^2\left\{4\Psi^2\rho^2 + \left[\frac{1 + (\alpha^2 - 1)\Psi}{\ln\alpha}\right]^2\frac{1}{\rho^2} - \left[\frac{4\Psi + 4(\alpha^2 - 1)\Psi^2}{\ln\alpha}\right]\right\}t \tag{E12.3-11}$$

The melt residence time of each layer in the die is actually dependent of radius coordinate ρ, that is

$$t(\rho)_{\text{res}} = \frac{L}{u(\rho)V} \tag{E12.3-12}$$

Inserting Eq. E12.3-12 into Eq. E12.3-11 gets the melt temperature increase of each layer of melt fluid throughout the die.

$$(T(\rho) - T_0)_{\text{exit}} = \frac{\mu L}{\rho C_v V u(\rho)} \left(\frac{V}{R_i}\right)^2$$

$$\left\{ 4\Psi^2 \rho^2 + \left[\frac{1 + (\alpha^2 - 1)\Psi}{\ln \alpha}\right]^2 \frac{1}{\rho^2} - \left[\frac{4\Psi + 4(\alpha^2 - 1)\Psi^2}{\ln \alpha}\right] \right\} \quad \text{(E12.3-13)}$$

We now discuss the residence times and temperature increases of layers close to the die wall using the preceding equations: At $r = R_o - 0.1$ mm and $r = R_o - 0.01$ mm, the residence time and the temperature increase of the two layers are, respectively, 0.008 s, 77°C and 0.082 s, 704°C. On the other hand, on the core surface ($r = R_i$), the residence time is 0.0005 s, and the temperature increase only 38°C. It is obvious that the closer the melt layer is to the die wall, the residence time is longer and the melt temperature during transit increases in an exponential fashion. Despite the very high temperature increases, the residence time of the melt layers near the wall is short and much shorter than the degradation induction time $\theta(T)$ (see Fig. E5.1(a), which is for unplasticized PVC). Thus, degradation is not likely to occur, and the wall melt layer has such a small viscosity that it precludes melt fracture.

If the melt viscosity is considered as a function of temperature, then the momentum and energy equations will have to be solved simultaneously. Nevertheless, the results concerning the temperature increase of the melt layers near the wall will be only slightly different from that just given. The resulting polymer coat thickness can be calculated by equating the volumetric flow rates inside and outside the die, namely:

$$Q_{\text{inside}} = \rho_{\text{melt}} \pi R_i^2 V \left\{ \frac{(\alpha^2 - 1)}{2 \ln \alpha} - 1 + \left[\frac{(\alpha^2 - 1)}{\ln \alpha} - (\alpha^2 + 1)\right] \frac{(\alpha^2 - 1)}{2} \Psi \right\} \quad \text{(E12.3-14)}$$

$$Q_{\text{onwire}} = \rho_{\text{solid}} \pi V \left(2 R_i h + h^2\right) \quad \text{(E12.3-15)}$$

Solving for h, the polymer melt-coating thickness, we obtain $h = 0.45$ mm. Thus, taking into account the density increase upon solidification, the solid polymer coat thickness is $h_s = 0.37$ mm.

12.6   PROFILE EXTRUSION

Profiles are all extruded articles having a cross-sectional shape that differs from that of a circle, an annulus, or a very wide and thin rectangle (flat film or sheet). The cross-sectional shapes are usually complex, which, in terms of solving the flow problem in profile dies, means complex boundary conditions. Furthermore, profile dies are of nonuniform thickness, raising the possibility of transverse pressure drops and velocity components, and making the prediction of extrudate swelling for viscoelastic fluids very difficult. For these reasons, profile dies are built today on a trial-and-error basis, and final product shape is achieved with "sizing" devices that act on the extrudate after it leaves the profile die.

The problem of steady, isothermal flow in straight axis channels of noncircular cross section has received considerable theoretical attention. The results of such studies (usually numerical solutions) indicate that, for Newtonian fluids, flow involving the axial velocity component alone satisfies the equations of continuity and motion (75–77).

The same statement can be made about *inelastic* non-Newtonian fluids, such as the Power Law fluid, from a mathematical solution point of view. In reality, most non-Newtonian fluids are viscoelastic and exhibit normal stresses. For fluids such as those (i.e., fluids described by constitutive equations that predict normal stresses for viscometric flows), theoretical analyses have shown that secondary flows are created inside channels of nonuniform cross section (78,79). Specifically it can be shown that a zero second normal stress difference is a necessary (but not sufficient) condition to ensure the absence of secondary flow (79). Of course, the analyses of flows in noncircular channels in terms of constitutive equations—which, strictly speaking, hold only for viscometric flows—are expected to yield qualitative results only. Experimentally low Reynolds number flows in noncircular channels have not been investigated extensively. In particular, only a few studies have been conducted with fluids exhibiting normal stresses (80,81). Secondary flows, such as vortices in rectangular channels, have been observed using dyes in dilute aqueous solutions of polyacrylamide. Interestingly, these secondary flow vortices (if they exist) seem to have very little effect on the flow rate.

Let us examine more closely some of the problems that arise in designing profile extrusion dies whose origin is to be found in the flow patterns. We consider the square-tube flow patterns calculated for a Power Law fluid of $n = 0.5$ (Fig. 12.47). Although the velocity profiles are symmetric, they are still θ-dependent, θ being the angle in the
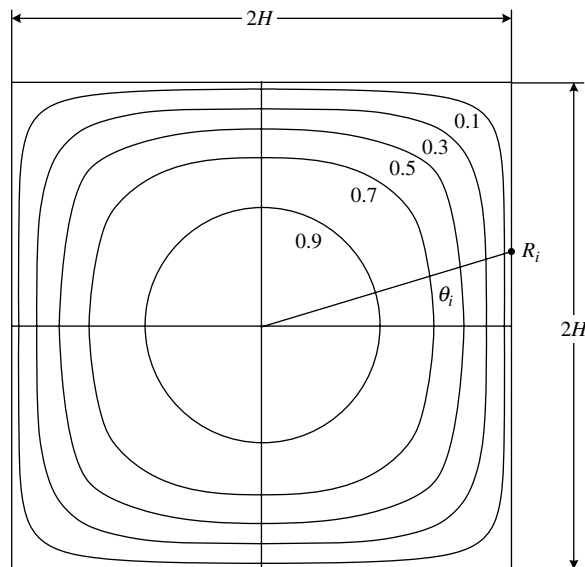

Fig. 12.47   Isovelocity contours v/V_0 of a power law fluid flowing in a square channel, $n = 0.5$. [Reprinted by permission from F. Röthemeyer, *Kunststoffe*, **59**, 333 (1969).]
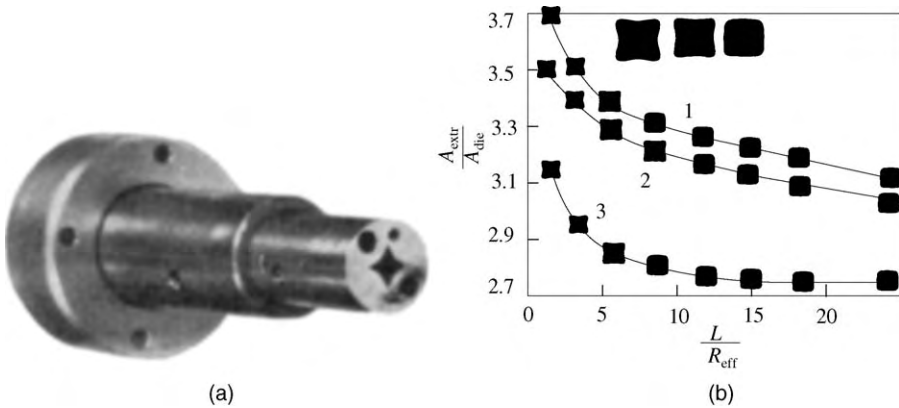
(a)   (b)

Fig. 12.48 (a) Profile die shape used in obtaining the results in (b). (b) Plot of A_{extr}/A_{die} vs. L/R_{eff} for LDPE, $R_{eff} = (2A_{die}/\text{perimeter of die})$. Curve 1, $T = 196°C$, $\Gamma_{eff} = 40/\pi R_{eff}^3 = 79 \text{ s}^{-1}$; Curve 2, $T = 189°C$, $\Gamma_{eff} = 56 \text{ s}^{-1}$; Curve 3, $T = 180°C$, $\Gamma_{eff} = 30 \text{ s}^{-1}$. [Reprinted by permission from F. Röthemeyer, *Kunststoffe*, **59**, 333 (1969).]

cross-sectional plane. Furthermore, it is evident that the velocity gradient dv_z/dr, where r is an "effective radius" coordinate, also depends on the angle θ. Therefore, in each quadrant, for every value of the angle θ, there is a different velocity gradient variation with r. At $\theta = 0$ and $\theta = \pi/2$, the velocity gradients are high, since $r = H$, while at $\theta = \pi/4$, where $r = \sqrt{2}H$, the velocity gradients are small. It follows then that, if a polymer melt were flowing in a channel of square cross section, the extrudate would *swell more* at the vicinity of the center than of its sides, because of the high prevailing shear rates; the resulting extrudate shape would then show a "bulge" outward at the sides.

What is important from a die-designing point of view is that the cross-sectional shapes of the die and the extrudates are *different*. Simply put, to produce a square cross-section extrudate, one needs a die that looks like a four-cornered star [Fig. 12.48(a)], whose sides are concave. The curvature of the walls of the die used depends on the variation of extrudate swelling with shear stress for the polymer used. The differences in the shapes and magnitudes of the cross-sectional areas are primarily due to the θ-dependence of the degree of extrudate swelling.

As Fig. 12.48(b) indicates, the degree of swelling and the shape of the extrudate vary with increasing L/D of the die. First, the ratio of areas of the extrudate and the die decreases with increasing L/R_{eff}; this effect was also observed with circular dies. It is again attributed to the loss of memory by the melt of the entrance deformations.

The second effect is quite interesting and significant. At very short L/R_{eff} values, although the degree of swelling is large, the extrudate shape is closer to that of the die than it is at large L/R_{eff} values. The reason for this phenomenon is the following: at short capillary lengths, the stress field is probably not fully established, at least as far as establishing reasonable shear strains that are independent of the axial distance, thus the effects of the varying velocity gradients and recoverable strains at the various θ_i are not fully felt. Furthermore, at short L/R_{eff} values, entrance tensile strains predominate and mark the effects of the θ-dependent flow and recoverable shear strain fields. From a die design point of view, though, it seems that short profile dies,
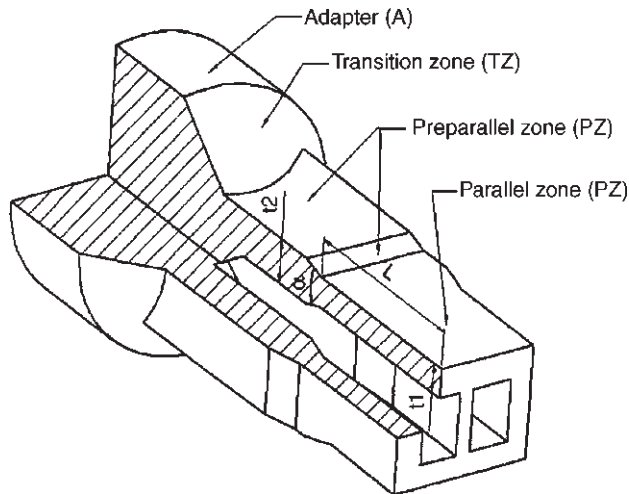
Fig. 12.49   Flow channel of a profile extrusion die: identification of its main zones and geometrical controllable parameters considered in the definition of the preparallel zone (PPZ).

in addition to resulting in small pressure drops, also form extrudates of shapes closer to that of the die.

Streamlining of the complex profile dies is as necessary as with any other die shape, but obviously more difficult. For this reason, plate dies (82) made up of thin plates inserted in a die housing one behind the other, are common. The channel cross-sections in the individual plates differ in such a way as to streamline the polymer melt into the final plate. This construction makes both die modifications and die machining easier. In such complex dies, even approximate design expressions have not been developed yet; in practice, the repeated filing off of metal in the approach plates achieves the desired shape.

The availability of powerful three-dimensional flow computer simulation packages and personal computers capable of handling them is gradually transforming profile die design from an empirical trial-and-error process to one where design optimization benefits from computational results. Sebastian and Rakos (83) were the first to utilize realistic computational fluid-mechanical results in the design of profile dies.

Sienz et al. (84,85), and Nóbrega et al. (86,87) divided a given profile die into distinct axial zones, each having variable and controllable geometric parameters, as shown in Fig. 12.49. Furthermore, after carrying out the three-dimensional nonisothermal flow simulation for a given geometry, the "quality" of the result was assesed through the use of an *objective function*, in which for Nóbrega et al. (86), combines two criteria: the flow balance and the segment length to metal thickness ratio $(L/t)_i$. Two optimization methods are then utilized to arrive at the optimal profile die geometry: the SIMPLEX method and one that starts with a trial geometry, suggested by the mold maker, taking advantage of relevant experience, together with mesh refinement, to arrive at an optimal profile die geometry. Computational results are shown in Fig. 12.50.

Although such numerical die design optimization techniques significantly improve the flow uniformity and reduce the level of internal stresses leading to extrudate distortion,
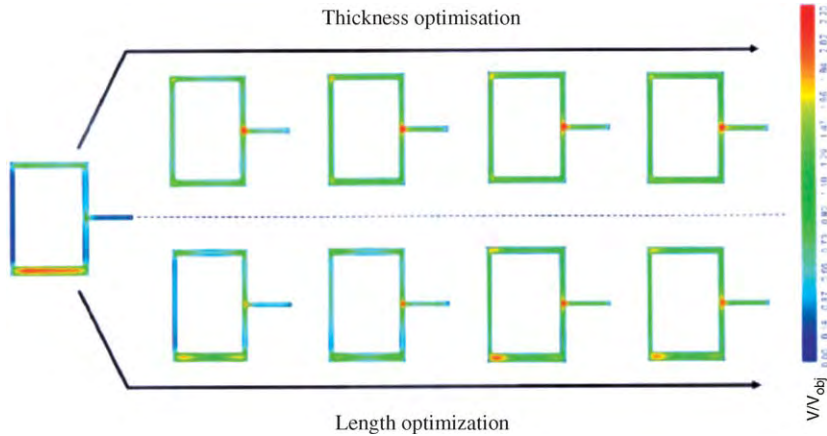
Fig. 12.50   Contours of the ratio V/V_{obj} corresponding to some steps of the optimization procedure employed by Nóbrega et al. (86,87) [Reprinted by permission from J. M. Nóbrega, O. S. Carneiro, P. J. Oliveira, F. T. Pinho, "Flow Balancing in Extrusion Dies for Thermoplastic Profiles, Part III Experimental Extrusion," *Intern. Polym. Process.*, **19**, 225 (2004).]

they still have to be combined with final experimental geometry adjustments. Furthermore, the viscoelastic profile extrudate swelling is not addressed, requiring further geometry adjustments, as discussed earlier. Thus, the net gain in using computational die designs is the elimination of some or many trial-and-error geometries from the initial to the final versions.

Before closing this chapter, we feel that it is useful to list in tabular form some isothermal pressure-flow relationships commonly used in die flow simulations. Tables 12.1 and 12.2 deal with flow relationships for the parallel-plate and circular tube channels using Newtonian (N), Power Law (P), and Ellis (E) model fluids. Table 12.3 covers concentric annular channels using Newtonian and Power Law model fluids. Table 12.4 contains volumetric flow rate–pressure drop (die characteristic) relationships only, which are arrived at by numerical solutions, for Newtonian fluid flow in eccentric annular, elliptical, equilateral, isosceles triangular, semicircular, and circular sector and conical channels. In addition, Q versus ΔP relationships for rectangular and square channels for Newtonian model fluids are given. Finally, Fig. 12.51 presents shape factors for Newtonian fluids flowing in various common shape channels. The shape factor M_0 is based on parallel-plate pressure flow, namely,
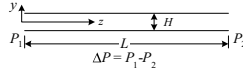
$$Q_{\text{ch}} = Q_{PP}M_0 \tag{12.6-1}$$

where

$$Q_{pp} = \frac{\Delta P B d^3}{12\mu L} \tag{12.6-2}$$

Q_{ch} is the volumetric flow rate in any of the channels appearing in the figure and B and d are specified for each channel in the figure.

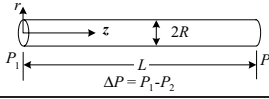**TABLE 12.1   Parallel-Plate Pressure Flow:**

$$y \uparrow \quad \overset{\longrightarrow z \quad \updownarrow H}{\underset{P_1 \vdash\!\!\!-\!\!\!-\!\!\!-L-\!\!\!-\!\!\!-\!\!\!\dashv P_2}{\qquad}} \quad \Delta P = P_1 - P_2$$

$\text{(N)}^a \, \tau_{yz} = -\mu \dfrac{dv_z}{dy}$	$\text{(P)}^a \, \tau_{yz} = -m \left\lvert \dfrac{dv_z}{dy} \right\rvert^{n-1} \dfrac{dv_z}{dy}$
$\tau_{yz}(y) = \left(\dfrac{\Delta P}{L}\right) y$	$\tau_{yz}(y) = \left(\dfrac{\Delta P}{L}\right) y$
$\tau_w = \tau_{yz}\left(\dfrac{H}{2}\right) = \dfrac{H \Delta P}{2L}$	$\tau_w = \tau_{yz}\left(\dfrac{H}{2}\right) = \dfrac{H \Delta P}{2L}$
$-\dot\gamma_{yz}(y) = \left(\dfrac{\Delta P}{\mu L}\right) y$	$-\dot\gamma_{yz}(y) = \left(\dfrac{\Delta P}{m L} y\right)^s \quad y \geq 0$
$\dot\gamma_w = -\dot\gamma_{yz}\left(\dfrac{H}{2}\right) = \dfrac{H \Delta P}{2\mu L}$	$\dot\gamma_w = -\dot\gamma_{yz}\left(\dfrac{H}{2}\right) = \left(\dfrac{H \Delta P}{2m L}\right)^s$
$v_z(y) = \dfrac{H^2 \Delta P}{8\mu L}\left[1 - \left(\dfrac{2y}{H}\right)^2\right]$	$v_z(y) = \dfrac{H}{2(s+1)}\left(\dfrac{H \Delta P}{2m L}\right)^s\left[1 - \left(\dfrac{2y}{H}\right)^{s+1}\right] \quad y \geq 0$
$v_z(0) = v_{\max} = \dfrac{H^2 \Delta P}{8\mu L}$	$v_z(0) = v_{\max} = \dfrac{H}{2(s+1)}\left(\dfrac{H \Delta P}{2m L}\right)^s$
$\langle v_z \rangle = \dfrac{2}{3} v_{\max}$	$\langle v_z \rangle = \left(\dfrac{s+1}{s+2}\right) v_{\max}$
$Q = \dfrac{W H^3 \Delta P}{12\mu L}$	$Q = \dfrac{W H^2}{2(s+2)}\left(\dfrac{H \Delta P}{2m L}\right)^s$

$$\text{(E)}^a \, \tau_{yz} = -\eta(\tau)\frac{dv_z}{dy} \qquad \eta(\tau) = \frac{\eta_0}{1 + (\tau/\tau_{1/2})^{\alpha-1}} \qquad \tau = |\tau_{yz}|$$

$$\tau_{yz}(y) = \left(\frac{\Delta P}{L}\right) y$$

$$\tau_w = \tau_{yz}\left(\frac{H}{2}\right) = \frac{H \Delta P}{2L}$$

$$-\dot\gamma_{yz}(y) = \left(\frac{\Delta P}{\eta_0 L}\right) y \left[1 + \left(\frac{\Delta P y}{\tau_{1/2} L}\right)^{\alpha-1}\right]$$

$$\dot\gamma_w = -\dot\gamma_{yz}\left(\frac{H}{2}\right) = \frac{H \Delta P}{2\eta_0 L}\left[1 + \left(\frac{H \Delta P}{2\tau_{1/2} L}\right)^{\alpha-1}\right]$$

$$v_z(y) = \frac{H^2 \Delta P}{8\eta_0 L}\left\{\left[1 - \left(\frac{2y}{H}\right)^2\right] + \left(\frac{2}{1+\alpha}\right)\left(\frac{H \Delta P}{2 L \tau_{1/2}}\right)^{\alpha-1}\left[1 - \left(\frac{2y}{H}\right)^{\alpha+1}\right]\right\}$$

$$v_z(0) = v_{\max} = \frac{H^2 \Delta P}{8\eta_0 L}\left[1 + \left(\frac{2}{1+\alpha}\right)\left(\frac{H \Delta P}{2 L \tau_{1/2}}\right)^{\alpha-1}\right]$$

$$\langle v_z \rangle = \frac{2}{3} v_{\max}\left[1 + \left(\frac{3}{2+\alpha}\right)\left(\frac{H \Delta P}{2 L \tau_{1/2}}\right)^{\alpha-1}\right] \Big/ \left[1 + \left(\frac{2}{1+\alpha}\right)\left(\frac{H \Delta P}{2 L \tau_{1/2}}\right)^{\alpha-1}\right]$$

$$Q = \frac{W H^3 \Delta P}{12\eta_0 L}\left[1 + \left(\frac{3}{2+\alpha}\right)\left(\frac{H \Delta P}{2 L \tau_{1/2}}\right)^{\alpha-1}\right]$$

a ⓝ Newtonian fluid; ⓟ Power Law model fluid; ⓔ Ellis fluid.

TABLE 12.2   Circular-Tube Pressure Flow:

$$\textcircled{N}\,\tau_{rz} = -\mu \frac{dv_z}{dr} \qquad\qquad \textcircled{P}\,\tau_{rz} = -m\left|\frac{dv_z}{dr}\right|^{n-1}\frac{dv_z}{dr}$$

$$\tau_{rz}(r) = \left(\frac{\Delta P}{2L}\right)r \qquad\qquad \tau_{rz}(r) = \left(\frac{\Delta P}{2L}\right)r$$

$$\tau_w = \tau_{rz}(R) = \frac{R\Delta P}{2L} \qquad\qquad \tau_w = \tau_{rz}(R) = \frac{R\Delta P}{2L}$$

$$-\dot{\gamma}_{rz}(r) = \left(\frac{\Delta P}{2\mu L}\right)r \qquad\qquad -\dot{\gamma}_{rz}(r) = \left(\frac{\Delta Pr}{2mL}\right)^s$$

$$\dot{\gamma}_w = -\dot{\gamma}_{rz}(R) = \frac{R\Delta P}{2\mu L} \qquad\qquad \dot{\gamma}_w = -\dot{\gamma}_{rz}(R) = \left(\frac{R\Delta P}{2mL}\right)^s$$

$$v_z(r) = \frac{R^2\Delta P}{4\mu L}\left[1 - \left(\frac{r}{R}\right)^2\right] \qquad v_z(r) = \frac{R}{1+s}\left(\frac{R\Delta P}{2mL}\right)^s\left[1 - \left(\frac{r}{R}\right)^{s+1}\right]$$

$$v_z(0) = v_{\max} = \frac{R^2\Delta P}{4\mu L} \qquad\qquad v_z(0) = v_{\max} = \frac{R}{1+s}\left(\frac{R\Delta P}{2mL}\right)^s$$

$$\langle v_z\rangle = \frac{1}{2}v_{\max} \qquad\qquad \langle v_z\rangle = \left(\frac{s+1}{s+3}\right)v_{\max}$$

$$Q = \frac{\pi R^4\Delta P}{8\mu L} \qquad\qquad Q = \frac{\pi R^3}{s+3}\left(\frac{R\Delta P}{2mL}\right)^s$$

$$\textcircled{E}\,\tau_{rz} = -\eta(\tau)\frac{dv_z}{dr} \qquad \eta(\tau) = \frac{\eta_0}{1 + \left(\tau/\tau_{1/2}\right)^{\alpha-1}} \qquad \tau = |\tau_{rz}|$$

$$\tau_{rz}(r) = \left(\frac{\Delta P}{2L}\right)r$$

$$\tau_w = \tau_{rz}(R) = \frac{R\Delta P}{2L}$$

$$-\dot{\gamma}_{rz}(r) = \left(\frac{\Delta P}{2\eta_0 L}\right)r\left[1 + \left(\frac{\Delta Pr}{2\tau_{1/2}L}\right)^{\alpha-1}\right]$$

$$\dot{\gamma}_w = -\dot{\gamma}_{rz}(R) = \frac{R\Delta P}{2\eta_0 L}\left[1 + \left(\frac{R\Delta P}{2\tau_{1/2}L}\right)^{\alpha-1}\right]$$

$$v_z(r) = \frac{R^2\Delta P}{4\eta_0 L}\left\{\left[1 - \left(\frac{r}{R}\right)^2\right] + \left(\frac{2}{1+\alpha}\right)\left(\frac{R\Delta P}{2L\tau_{1/2}}\right)^{\alpha-1}\left[1 - \left(\frac{r}{R}\right)^{\alpha+1}\right]\right\}$$

$$v_z(0) = v_{\max} = \frac{R^2\Delta P}{4\eta_0 L}\left[1 + \left(\frac{2}{1+\alpha}\right)\left(\frac{R\Delta P}{2L\tau_{1/2}}\right)^{\alpha-1}\right]$$

$$\langle v_z\rangle = \frac{1}{2}v_{\max}\left[1 + \left(\frac{4}{3+\alpha}\right)\left(\frac{R\Delta P}{2L\tau_{1/2}}\right)^{\alpha-1}\right]\Bigg/\left[1 + \left(\frac{2}{1+\alpha}\right)\left(\frac{R\Delta P}{2L\tau_{1/2}}\right)^{\alpha-1}\right]$$

$$Q = \frac{\pi R^4\Delta P}{8\eta_0 L}\left[1 + \left(\frac{4}{3+\alpha}\right)\left(\frac{R\Delta P}{2L\tau_{1/2}}\right)^{\alpha-1}\right]$$
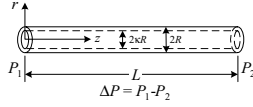
TABLE 12.3   Concentric Annular Pressure Flow:

$$\textcircled{N}^a \quad \tau_{rz} = -\mu \frac{dv_z}{dr}$$

$$\tau_{rz}(r) = \frac{\Delta PR}{2L}\left[\left(\frac{r}{R}\right) - \left(\frac{1-\kappa^2}{2\ln(1/\kappa)}\right)\left(\frac{R}{r}\right)\right]$$

$$-\dot{\gamma}_{rz}(r) = \frac{\Delta PR}{2\mu L}\left[\left(\frac{r}{R}\right) - \left(\frac{1-\kappa^2}{2\ln(1/\kappa)}\right)\left(\frac{R}{r}\right)\right]$$

$$\tau_{w1} = \tau_{rz}(R) = \frac{\Delta PR}{2L}\left[1 - \frac{1-\kappa^2}{2\ln(1/\kappa)}\right]$$

$$\tau_{w2} = \tau_{rz}(\kappa R) = \frac{\Delta PR}{2L}\left[\kappa - \frac{1-\kappa^2}{2\ln(1/\kappa)}\left(\frac{1}{\kappa}\right)\right]$$

$$\dot{\gamma}_{w1}(r) = -\dot{\gamma}_{rz}(R) = \frac{\Delta PR}{2\mu L}\left[1 - \left(\frac{1-\kappa^2}{2\ln(1/\kappa)}\right)\right]$$

$$\dot{\gamma}_{w2}(r) = -\dot{\gamma}_{rz}(\kappa R) = \frac{\Delta PR}{2\mu L}\left[\kappa - \left(\frac{1-\kappa^2}{2\ln(1/\kappa)}\right)\left(\frac{1}{\kappa}\right)\right]$$

$$v_z(r) = \frac{\Delta PR^2}{4\mu L}\left[1 - \left(\frac{r}{R}\right)^2 + \left(\frac{1-\kappa^2}{2\ln(1/\kappa)}\right)\ln\left(\frac{r}{R}\right)\right]$$

$$v_z(\lambda R) = v_{\max} = \frac{\Delta PR^2}{4\mu L}\left\{1 - (\lambda^2)\left[1 - \ln(\lambda^2)\right]\right\} \quad \lambda^2 = \frac{1-\kappa^2}{2\ln(1/\kappa)}$$

$$\langle v_z \rangle = \frac{\Delta PR^2}{8\mu L}\left[(1+\kappa^2) - \left(\frac{1-\kappa^2}{2\ln(1/\kappa)}\right)\right]$$

$$Q = \frac{\pi \Delta PR^4}{8\mu L}\left[(1-\kappa^4) - \frac{(1-\kappa^2)^2}{2\ln(1/\kappa)}\right]$$

$$\textcircled{P}^b \quad \tau_{rz} = -m\left|\frac{dv_z}{dr}\right|^{n-1}\left(\frac{dv_z}{dr}\right) \qquad \rho = \frac{r}{R} \qquad s = \frac{1}{n} \qquad \tau_{rz}(\lambda R) = 0$$

$$v_z^{\mathrm{I}}(r) = R\left(\frac{\Delta PR}{2mL}\right)^s \int_\kappa^\rho \left(\frac{\lambda^2}{\rho} - \rho\right)^s d\rho \quad \kappa \le \rho \le \lambda$$

$$v_z^{\mathrm{II}}(r) = R\left(\frac{\Delta PR}{2mL}\right)^s \int_\kappa^\rho \left(\rho - \frac{\lambda^2}{\rho}\right)^s d\rho \quad \lambda \le \rho \le 1$$

λ is evaluated numerically for the preceding equations using the boundary condition.

$$v_z^{\mathrm{I}}(\lambda R) = v_z^{\mathrm{II}}(\lambda R)$$

$$Q = \frac{\pi R^3}{s+2}\left(\frac{R\Delta P}{2mL}\right)^s (1-\kappa)^{s+2} F_1(n,\kappa)$$

$F_1(n,\kappa) = F(n,\beta)$ is given in graphical form in Fig. 12.45, when $\kappa = 1/\beta$.
Very thin annuli ($\kappa \to 1$), $F_1(n,\kappa) \to 1$

TABLE 12.3   (*Continued*)

$$\text{E}^c \ \tau_{rz} = -\eta(\tau)\frac{dv_z}{dr} \qquad \eta(\tau) = \frac{\eta_0}{1 + (\tau/\tau_{1/2})^{\alpha-1}} \qquad \tau = |\tau_{rz}|$$

$$Q = \frac{\tau_{1/2}\pi R^3}{\eta_0}\left\{\frac{\Delta PR}{2\tau_{1/2}}\left[\lambda^4\ln\frac{1}{\kappa} - \lambda^2\left(1-\kappa^2\right) + \frac{1}{4}\left(1-\kappa^4\right)\right]\right.$$

$$\left. + \left(\frac{\Delta PR}{2\tau_{1/2}}\right)^{\alpha}\left(\sum_{i=0}^{\alpha+1}\varepsilon_{i,i\neq(\alpha+3)/2}\lambda^{2i} + F\lambda^{\alpha+3}\right)\right\}$$

$$\varepsilon_i = \binom{\alpha+1}{i}(-1)^i\left(\frac{1+(-1)^{\alpha}\kappa^{\alpha+3-2i}}{\alpha+3-2i}\right)$$

$$F = \binom{\alpha+1}{(\alpha-1)/2}(-1)^{(\alpha-1)/2}\ln\left(\frac{1}{\kappa}\right) \qquad \alpha \text{ odd}$$

$$F = 2\sum_{i=0}^{\alpha+1}\binom{\alpha+1}{i}(-1)^i\left(\frac{1}{2i-\alpha+1}\right) \qquad \alpha \text{ even}$$

$$\text{E} \ \tau_{rz} = -\eta(\tau)\frac{dv_z}{dr} \qquad \eta(\tau) = \frac{\eta_0}{1 + (\tau/\tau_{1/2})^{\alpha-1}} \qquad \tau = |\tau_{rz}|$$

Approximately[d]
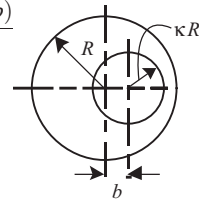
$$Q = \frac{\pi R^4 \Delta P \varepsilon^3}{6\eta_0 L}\left[1 + \frac{3}{\alpha+2}\left(\frac{\Delta P\varepsilon R}{2\tau_{1/2}L}\right)^{\alpha-1}\right]\left(1 - \frac{1}{2}\varepsilon + \frac{1}{60}\varepsilon^2 + \cdots\right)$$

where $\varepsilon = 1 - \kappa$. This approximate solution is valid for $\kappa > 0.6$

TABLE 12.4   Flows in Selected Conduits

Ⓝ Eccentric annulus pressure flow[a]

$$Q = \frac{\pi\Delta P}{8\mu L}\left\{R^4\left(1-\kappa^4\right) - \frac{(R+\kappa R + b)(R+\kappa R - b)(R-\kappa R + b)(R-\kappa R - b)}{\delta - \omega}\right.$$

$$\left. - 4b^2\kappa^2 R^2\left[1 + \frac{\kappa^2 R^4}{(R^2-b^2)} + \frac{\kappa^4 R^8}{\left[(R^2-b^2)^2 - \kappa^2 R^2 b^2\right]^2} + \cdots\right]\right\}$$

where

$$\omega = \frac{1}{2}\ln\frac{F+M}{F-M} \qquad \delta = \frac{1}{2}\ln\frac{F-b+M}{F-b-M}$$

$$F = \frac{R^2 - \kappa R^2 + b^2}{2b} \qquad M = \sqrt{F^2 - R^2}$$

(*Continued*)
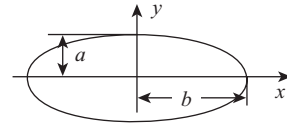
TABLE 12.4   (*Continued*)

Ⓝ Elliptical channel pressure flow[a]

$$v_z(x, y) = \frac{\Delta P a^2 b^2}{2\mu L(a^2 + b^2)} \left(1 - \frac{x^2}{b^2} - \frac{y^2}{a^2}\right)$$

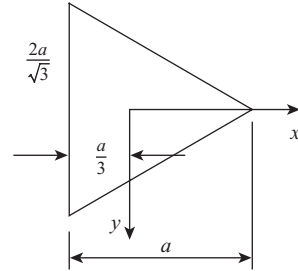$$Q = \frac{\pi \Delta P}{4\mu L} \frac{a^3 b^3}{a^2 + b^2}$$

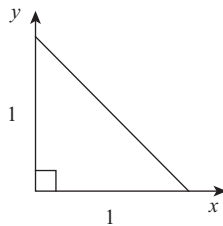Ⓝ Triangular channel pressure flow
1. Equilateral triangle[a]

$$v_z(x, y) = -\frac{\Delta P}{4a\mu L}\left[x^3 - 3xy^2 - a(x^2 + y^2) + \frac{4}{27}a^3 + \cdots\right]$$

$$Q = \frac{\Delta P a^4}{20\sqrt{3}\mu L}$$

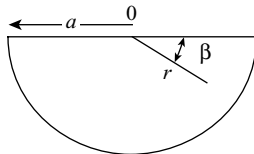$$\left.\frac{Q_{e.t}}{Q_{tube}}\right|_{\text{equal area}} = 0.72552 \qquad \frac{a^2}{\sqrt{3}} = \pi R^2$$

2. Isosceles triangle (right)[b]

$$v_z(x, y) = \frac{16l^2 \Delta P}{\pi^4 \mu L}\left[\sum_{i=1,3}\sum_{j=2,4} \frac{j \sin(i\pi x/l)\sin(j\pi y/l)}{i(j^2 - i^2)(i^2 + j^2)^2} + \sum_{i=2,4}\sum_{j=1,3} \frac{i\sin(i\pi x/l)\sin(j\pi y/l)}{j(i^2 - j^2)(i^2 + j^2)^2}\right]$$
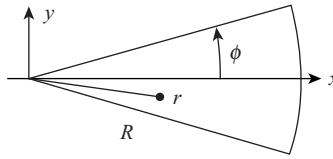
Ⓝ Semicircular channel pressure flow[b]

$$v_z(r, \beta) = \frac{\Delta P}{L\mu}a^4 \sum_{i=1,3,5}\left[\frac{4r^2}{a^4}\frac{1}{i\pi(4 - i^2)} - \frac{4r^i}{a^{i+2}}\frac{1}{i\pi(4 - i^2)}\right]\sin i\beta$$
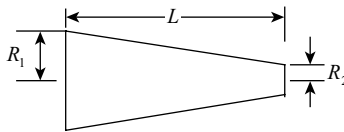
Ⓝ Circular section channel pressure flow[c]

$$v_z(x, y) = \frac{\Delta P}{2\mu L}\left[\frac{x^2 \tan^2\phi - y^2}{1 - \tan^2\phi} + \frac{16R^2(2\phi)^2}{\pi^3}\sum_{i=1,3\dots}^{\infty}(-1)^{(i+1)/2}\left(\frac{r}{R}\right)^{i\pi/2\phi}\frac{\cos(i\pi\phi)/2\phi}{i\left[i^2 - (4\phi/\pi)^2\right]}\right]$$

TABLE 12.4   (*Continued*)

Ⓝ Conical channel pressure flow

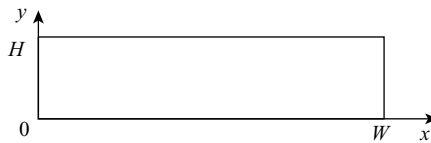$$Q = \frac{3\pi\Delta P}{8\mu L}\left[\frac{R_1^3 R_2^3}{R_1^2 + R_1 R_2 + R_2^2}\right]$$

Ⓟ Conical channel pressure flow[d] (by the lubrication approximation)

$$Q = \frac{n\pi R_1^3}{3n+1}\left(\frac{R_1 \Delta P a_{13}}{2mL}\right)^s$$

where

$$a_{13} = \frac{3n(R_1/R_2 - 1)}{R_1/R_2\left[(R_1/R_2)^{3n}-1\right]}$$

Ⓝ Rectangular channel pressure flow[e]

$$v_z(x,y) = \frac{\Delta P}{\mu L}\left\{\frac{y^2}{2} - \frac{yH}{2} + \frac{4H^2}{\pi^3}\sum_{i=1,3\ldots}^{\infty}\frac{\cosh[(i\pi/2H)(2x-W)]}{i^3\cosh(i\pi W/H)}\sin\left(\frac{i\pi y}{H}\right)\right\}$$

$$Q = \frac{WH^3}{12\mu}\left(\frac{\Delta P}{L}\right)\left[1 - \frac{129H}{\pi^5 W}\sum_{i=1,3\ldots}^{\infty}\frac{1}{i^5}\tanh\left(\frac{i\pi W}{2H}\right)\right] = \frac{WH^3}{12\mu}\left(\frac{\Delta P}{L}\right)\cdot F_p$$

(*Continued*)

TABLE 12.4   (*Continued*)

F_p is given graphically as follows:
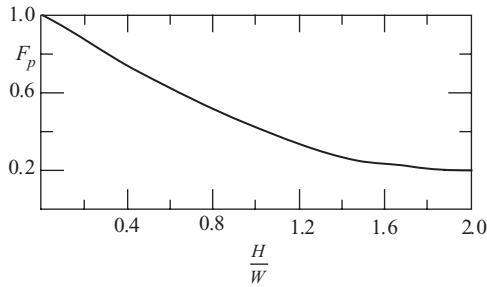
[a] J. Happel and H. Brenner, *Low Reynolds Number Hydrodynamics*, Prentice Hall, Englewood Cliffs, NJ, 1965, Chapter 2.
[b] S. M. Marco and L. S. Han, *Trans. Am. Soc. Mech. Eng.*, **56**, 625 (1955).
[c] E. R. G. Eckert and T. F. Irvine, *Trans. Am. Soc. Mech. Eng.*, **57**, 709 (1956).
[d] J. M. Mckelvey, V. Maire, and F. Haupt, *Chem. Eng.*, 95 (September 1976).
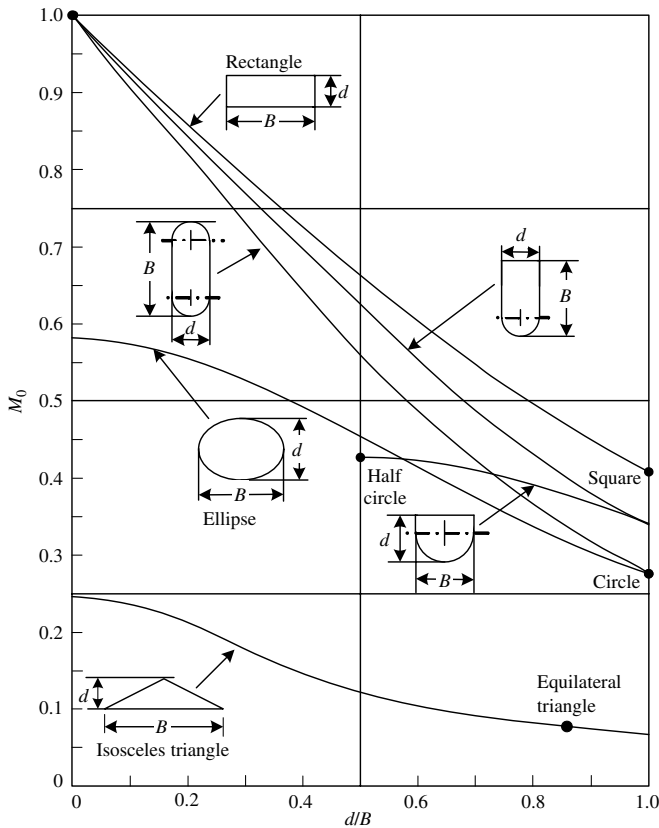[e] M. J. Boussinesq, *J. Math. Pure Appl.*, Ser. 2, **13**, 377 (1868).

Fig. 12.51   Graphical representation of shape factor M_0 used in Eq. 12.6-1 [Reprinted by permission from G. P. Lahti, *Soc. Plast. Eng. J.*, 619 (1963).]

REFERENCES

1. E. B. Bagley, "End Corrections in the Capillary Flow of Polyethylene," *J. Appl. Phys.*, **28**, 624 (1957).

2. C. McLuckie and M. Rogers, "Influence of Elastic Effects of Capillary Flow of Molten Polymers," *J. Appl. Polym. Sci.*, **13**, 1049 (1969).

3. N. Hirai and H. Eyring, "Bulk Viscosity of Polymeric Systems," *J. Polym. Sci.*, **37**, 51 (1959).

4. I. J. Duvdevani and I. Klein, "Analysis of Polymer Melt Flow in Capillaries Including Pressure Effects," *Soc. Plast. Eng. J.*, **23**, 41–45 (1967).

5. P. H. Goldblatt and R. S. Porter, "A Comparison of Equations for the Effect of Pressure on the Viscosity of Amorphous Polymers," *J. Appl. Polym. Sci.*, **20**, 1199 (1976).

6. B. C. Sakiades, "Equilibrium Flow of a General Fluid through a Cylindrical Tube," *AIChE J.*, **8**, 317 (1962).

7. C. D. Han, M. Charles, and W. Philippoff, "Measurements of the Axial Pressure Distribution of Molten Polymers in Flow through a Circular Tube," *Trans. Soc. Rheol.*, **13**, 453 (1969).

8. C. D. Han, "On Silt- and Capillary-Die Rheometry," *Trans. Soc. Rheol.*, **18**, 163 (1974).

9. C. D. Han, *Rheology in Polymer Processing*, Academic Press, New York, 1976, Chapter 5.

10. R. Nahme, *Ing. Arch.*, **11**, 191 (1940).

11. H. C. Brinkman, "Heat Effects in Capillary Flow I," *Appl. Sci. Res.*, **A2**, 120–124 (1951).

12. R. M. Turian and R. B. Bird, "Viscous Heating in the Cone-and-Plate Viscometer. II. Temperature Dependent Viscosity and Thermal Conductivity," *Chem. Eng. Sci.*, **18**, 689 (1963).

13. J. E. Gerrard, R. E. Steidler, and J. K. Appeldoorn, "Viscous Heating in Capillaries," *Ind. Eng. Chem. Fundam.*, **4**, 332 (1965).

14. R. M. Turian, "Viscous Heating in the Cone-and-Plate Viscometer. III," *Chem. Eng. Sci.*, **20**, 771 (1965).

15. R. A. Morrette and C. G. Gogos, "Viscous Dissipation in Capillary Flow of Rigid PVC and PVC Degradation," *Polym. Eng. Sci.*, **8**, 272 (1968).

16. D. E. Marshall, I. Klein, and R. H. Uhl, "Measurement of Screw and Plastic Temperature Profiles in Extruders," *Soc. Plast. Eng. J.*, **20**, 329 (1964).

17. J. Van Leeuwen, "Stock Temperature Measurement in Plastifying Equipment," *Polym. Eng. Sci.*, **7**, 98–109 (1967).

18. H. T. Kim and E. A. Collins, "Temperature Profiles of Polymer Melts in Tube Flow. Conduction and Shear Heating Corrections," *Polym. Eng. Sci.*, **11**, 83 (1971).

19. H. W. Cox and C. W. Macosko, "Viscous Dissipation in Die Flow," *AIChE J.*, **20**, 785 (1974).

20. N. Galili and R. Takserman-Krozer, "Heat Effect in Viscous Flow through a Pipe," *Israeli Tech.*, **9**, 439 (1971).

21. H. P. Schreiber and E. B. Bagley, "Melt Elasticity in Fractionated HDPE," *Polym. Lett.*, **1**, 365 (1963).

22. W. W. Graessley, S. D. Glasscock, and R. L. Crawley, "Die Swell in Molten Polymers," *Trans. Soc. Rheol.*, **14**, 519 (1970).

23. R. I. Tanner, "A Theory of Die Swell," *J. Polym. Sci.*, **A-28**, 2067 (1970).

24. A. S. Lodge, *Elastic Liquids*, Academic Press, New York, 1964, p. 131.

25. S. I. Abdel-Khalik, O. Hassager, and R. B. Bird, "Prediction of Melt Elasticity from Viscosity Data," *Polym. Eng. Sci.*, **14**, 859 (1974).

26. J. D. Ferry, *Viscoelastic Properties of Polymers*, Wiley, New York, 1971; also, S. Middleman, *Fundamentals of Polymer Processing*, McGraw-Hill, New York, 1977, p. 472.

27. J. L. White and J. F. Roman, "Extrudate Swell During the Melt Spinning of Fibers—Influence of Rheological Properties and Take-up Force," *J. Appl. Polym. Sci.*, **20,** 1005 (1976).

28. A. B. Metzner, W. T. Houghton, R. A. Sailor, and J. L. White, "A Method for the Measurement of Normal Stresses in Simple Shearing Flow," *Trans. Soc. Rheol.*, **5**, 133 (1961).

29. R. B. Bird, R. K. Prud'homme, and M. Gottlieb, "Extrudate Swell as Analyzed by Macroscopic Balances," The University of Wisconsin, Rheology Research Center Report RRC-35, 1975.

30. B. Whipple, "Velocity Distributions in Die Swell," Ph.D. Dissertation, Washington University, St. Louis, MO, 1974.

31. H. Giesekus, "Verschiedene Phänomene in Strömungen Viskoelastischer Flüssigkeiten durch Düsen," *Rheol. Acta*, **8**, 411 (1969).

32. H. L. Weissberg, "End Corrections for Slow Viscous Flow through Long Tubes," *Phys. Fluids*, **5**, 1033 (1962).

33. E. B. Bagley and R. M. Birks, "Flow of Polyethylene into a Capillary," *J. Appl. Phys.*, **31**, 556 (1960).

34. T. F. Ballenger and J. L. White, "The Development of the Velocity Field in Polymer Melts into a Reservoir Approaching a Capillary Die," *J. Appl. Polym. Sci.*, **15**, 1849 (1971).

35. P. Lamb and F. N. Cogswell, paper presented at the International Plastics Congress on Processing Polymer Products, Amsterdam, 1966.

36. H. L. LaNieve III, and D. C. Bogue, "Correlation of Capillary Entrance Pressure Drops with Normal Stress Data," *J. Appl. Polym. Sci.*, **12**, 353 (1968).

37. C. D. Han, "Influence of the Die Entry Angle in the Entrance Pressure Drop, Recoverable Elastic Energy and Onset of Flow Instability in Polymer Melt Flow," *J. Appl. Polym. Sci.*, **17**, 1403 (1973).

38. J. L. White and A. Kondo, "Rheological Properties of Polymer Melts and Flow Patterns During Extrusion through a Die Entry Region," *J. Appl. Polym. Sci.*, in press.

39. J. P. Tordella, in *Rheology*, Vol. 4, F. R. Eirich, Ed., Academic Press, New York, 1969, Chapter 3.

40. R. S. Spencer and R. D. Dillon, *J. Colloid Interface Sci.*, **3**, 163 (1940).

41. C. J. S. Petrie and M. M. Denn, "Instabilities in Polymer Processing," *AIChE J.*, **22**, 209 (1976).

42. M. M. Denn, "Extrusion Instabilities and Wall Slip," *Annu. Rev Fluid Mech.*, **33**, 265–287 (2001).

43. F. N. Cogswell and P. Lamb, *Plast. Today*, 33 (1969).

44. G. V. Vinogradov A., Ya. Malkin, Yu. G. Yanovskii, E. K. Borisenkova, B. V. Yarlykov, and G. V. Berezhnaya, "Viscoelastic Properties and Flow of Narrow Distribution PIB and Polyisoprene," *J. Polym. Sci.*, **A2 10**, 1061 (1972).

45. J. L. den Otter, "Mechanisms of Melt Fracture," *Plast. Polym.*, **38**, 155 (1970).

46. Y. Oyanagi, "A Study of Irregular Flow Behavior of HDPE," *Appl. Polym. Symp.*, **20**, 123 (1973).

47. N. Bergem, "Visualization Studies of Polymer Melt Flow Anomalies in Extrusion," *Proc 7th Int. Congr. on Rheology*, Gothenburg, Sweden, 1976, p. 50.

48. L. L. Blyler, Jr., and A. C. Hart, Jr., "Capillary Flow Instability of Ethylene Polymer Melts," *Polym. Eng. Sci.*, **10**, 193 (1970).

49. K. B. Migler, Y. Son, F. Qiao, and K. Flynn, "Extensional Deformation, Cohesive Failure, and Boundary Conditions during Sharkskin Melt Fracture," *J. Rheol*, **46**, 383–400, (2002).

50. M. Seth, S. G. Hatzikiriakos, and T. Clere, "Gross Melt Fracture Elimination: The Role of Surface Energy of Boron Nitride Powders," *Polym. Eng. Sci.*, **42**, 743–752 (2002).

51. F. N. Cogswell, "Stretching Flow Instabilities at the Exits of Extrusion Dies," *J. Non-Newt. Fluid Mech.*, **2**, 37–47 (1977).

52. E. G. Muliawan, S. G. Hatzikiriakos, and M. Sentmanat, "Melt Fracture of Linear PE," *Int. Polym. Process.*, **20**, 60–67 (2005).

53. M. L. Sentmanat, SER-HV AO1, *Universal Testing Platform Instrument Manual*, X-Pansion Instruments 2003.

54. M. L. Sentmanat, ''A Novel Device for Characterizing Polymer Flows in Uniaxial Extension,'' *SPE ANTEC Tech. Papers*, **61**, 992 (2003).

55. M. Sentmanat and S. G. Hatzikiriakos, ''Mechanism of Gross Melt Fracture Elimination in the Extrusion of Polyethylenes in the Presence of Boron Nitride,'' *Rheol. Acta*, **43**, 624–633 (2004).

56. C. G. Gogos, B. Qian, D. B. Todd, and T. R. Veariel, ''Melt Flow Instability Studies of Metallocene Catalyzed LLDPE in Pelletizing Dies,'' *SPE ANTEC Tech. Papers*, **48**, 112–116 (2002).

57. T. R. Veariel, B. Qian, C. G. Gogos, and D. B. Todd, Patent Application #2005-0074609, ExxonMobil Chemical Co, Published April 7, 2005.

58. J. Vlachopoulos and T. W. Chan, ''A Comparison of Melt Fracture Initiation Conditions in Capillaries and Slits,'' *J. Appl. Polym. Sci.*; also, J. Vlachopoulos, M. Horie, and S. Lidorikis, ''An Evaluation of Expressions Predicting Die Swell,'' *Trans. Soc. Rheol.*, **16**, 669 (1972).

59. J. F. Carley, ''Flow of Melts in Crosshead-Slit Dies; Criteria for Die Design,'' *J. Appl. Phys.*, **25**, 1118 (1954).

60. J. R. A. Pearson, ''Non-Newtonian Flow and Die Design. Part IV. Flat Film Die Design,'' *Trans. J. Plast. Inst*., **32**, 239 (1964).

61. J. M. McKelvey and K. Ito, ''Uniformity of Flow from Sheeting Dies,'' *Polym. Eng. Sci.*, **11**, 258 (1971).

62. Y. Sun and M. Gupta, ''Elongational Viscosity on the Flow of a Flat Die,'' *Int. Polym. Process.*, **18**, 353 (2003).

63. D. Sarkar and M. Gupta, ''Further investigation of the effect of elongational viscosity on entrance flow,'' *J. Reinf. Plast. Comp*., **20**, 1473–1484 (2001).

64. C. D. Han, *Multiphase Flow in Polymer Processing*, Academic Press, New York, 1981, Chapter 7.

65. H. Mavridis and R. N. Shroff, ''Multilayer Extrusion: Experiments and Computer Simulation,'' *Polym. Eng. Sci*., **34**, 559–569 (1994).

66. W. J. Schrenk, N. L. Bradley, T. Alfrey, and H. Maack, ''Interfacial Flow Instability in Multilayer Coextrusion,'' *Polym. Eng. Sci.*, **18**, 620–623 (1978); also, W. J. Schrenk and T. Alfrey, ''Co-extruded Multilayer Films and Sheets,'' in *Polymer Blends* Vol. 2, D. R. Paul and N. Seymour, Eds., Academic Press, New York, 1978.

67. J. M. Dealey and K. F. Wissbrun *Melt Rheology and Its Role in Plastics Processing*, Van Nostrand Reinhold, New York (1990).

68. T. C. Yu and C. D. Han, ''Stratified Two-phase Flow of Molten Polymers,'' *J. Appl. Polym. Sci.*, **17**, 1203–1225 (1973).

69. R. Sabia, ''On the Characterization of Non-Newtonian Flow,'' *J. Appl. Polym. Sci.*, **7**, 347–355 (1963).

70. A. I. Leonov, ''On a Class of Constitutive Equations for Viscoelastic Liquids,'' *J. Non-Newt. Fluid Mech.*, **25**, 1–59 (1987).

71. A. G. Fredrickson and R. B. Bird, ''Non-Newtonian Flow in Annuli,'' *Ind. Eng. Chem.*, **50**, 347 (1958).

72. R. A. Worth and J. Parnaby, ''The Design of Dies for Polymer Processing Machinery,'' *Trans. Inst. Chem. Eng*., **52**, 368 (1974).

73. J. R. A. Pearson, ''Non-Newtonian Flow and Die Design. Part I,'' *Trans. J. Plast. Inst*., **30**, 230 (1962).

74. C. Gutfinger, E. Broyer, and Z. Tadmor, ''Analysis of a Cross Head Film Blowing Die with the Flow Analysis Network (FAN) Method,'' *Polym. Eng. Sci*., **15**, 385–386 (1975).

75. O. Yandoff, *Acad. Sci., Paris*, **223**, 192 (1946).

76. R. S. Schechter, "On the Steady Flow of a Non-Newtonian Fluid in Cylinder Ducts," *AIChE J.*, **7**, 445 (1961).

77. J. A. Wheeler and E. H. Wissler, "Steady Flow of Non-Newtonian Fluids in Square Duct," *Trans. Soc. Rheol.*, **10**, 353 (1966).

78. A. E. Green and R. S. Rivlin, "Steady Flow of Non-Newtonian Fluids through Tubes," *Quant. Appl. Math.*, **14**, 299 (1956).

79. J. G. Oldroyd, "Some Steady Flows of the General Elastic-viscous Liquid," *Proc. Roy. Soc.*, **A283**, 115 (1965).

80. H. Giesekus, "Sekundärströmungen in viskoelastischen Flüssigkeiten bei stationärer und periodischer Bewegung," *Rheol. Acta*, **4**, 85-101 (1965).

81. A. G. Dodson, P. Townsend, and K. Walters, "Non-Newtonian Flow in Pipes of Non-Circular Cross Section," *Comp. Fluids.*, **2**, 317–338 (1974).

82. S. Matsuhisa, *Jpn Plast. Age*, **12**, 25 (1974).

83. D. H. Sebastian and R. Rakos, "Interactive Software Package for the Design and Analysis of Extrusion Profile Dies," *Adv. Polym. Tech.*, **5**, 333–339 (1985).

84. J. Sienz., S. D. Bullman, and J. F. T. Pittman, paper presented at the 4th ESAFORM Conference, Liege, Belgium, (2001).

85. I. Szarvasy, J. Sienz, J. F. T. Pittman, and E. Hinton, "Computer Aided Optimisation of Profile Assessment," *Int. Polym. Process.*, **18**, 235 (2003).

86. J. M. Nóbrega, O. S. Carneiro, P. J. Oliveira, and F. T. Pinho, "Flow Balancing in Extrusion Dies for Thermoplastic Profiles, Part I: Automatic Design," *Int. Polym. Process.*, **18**, 298 (2003).

87. J. M. Nóbrega, O. S. Carneiro, F. T. Pinho, and P. J. Oliveira, "Flow Balancing in Extrusion Dies for Thermoplastic Profiles, Part III: Experimental Extrusion," *Int. Polym. Process.*, **19**, 225–235 (2004).

PROBLEMS

12.1 *Bagley Corrections* (a) Given the "raw" capillary flow data for two capillaries, plot both $[\Delta P/(4L/D_o)]$ and $\Delta P/4[L/D_o + N(\Gamma)]$ vs. Γ, showing that the flow curves of the former depend on L/D_o, while the latter is L/D_o independent. (b) Consider the experimental point $L/D_o = 50$ and $\Gamma = 2000$ s^{-1} on Fig. 12.6. What would the magnitude of the error be in evaluating the shear stress at the wall, if the Bagley entrance correction is neglected? Repeat the calculation for $L/D_o = 6$, $\Gamma = 2000$ s^{-1}.

Capillary A		Capillary B	
$L = 0.500$ in ΔP(psi)	$D_0 = 0.0625$ in Γ (s^{-1})	$L = 2.005$ in ΔP(psi)	$D_0 = 0.0501$ in Γ(s^{-1})
125.7	7.68	578.6	14.87
149.2	15.36	844.5	29.73
227.7	38.40	1353.1	74.34
394.7	76.81	1886.4	148.67
610.3	153.61	2645.8	297.34
972.6	384.03	3943.6	743.35
1298.7	768.07	5103.1	1486.71
1688.2	1536.13	6479.9	2973.41

12.2 ***Relative Magnitude of*** ΔP_{ent} ***and*** P_{ex} In the accompanying figure, Han[11] presents capillary flow data on HDPE at 180°C with which a Bagley plot can be constructed for $\Gamma = 327.7$ s^{-1}. (a) Assuming $P_{ex} = 0$, show that for the shear rate $N = 3.3$ and that for $L/D_0 = 4$ and 8, respectively, τ_w^* is 20.21 and 20.46 psi. (b) Taking into account the measured ΔP_{ent} and P_{ex} values, show that $\tau_w^* = (\Delta P - \Delta P_{ent} - P_{ex})D_0/4L$ and that τ_w^* values are in this case 21.19 and 21.42 psi for $L/D_0 = 4$ and 8, respectively. That is, including P_{ex} (which is not readily available experimentally), increases the value of τ_w^* by 5%.
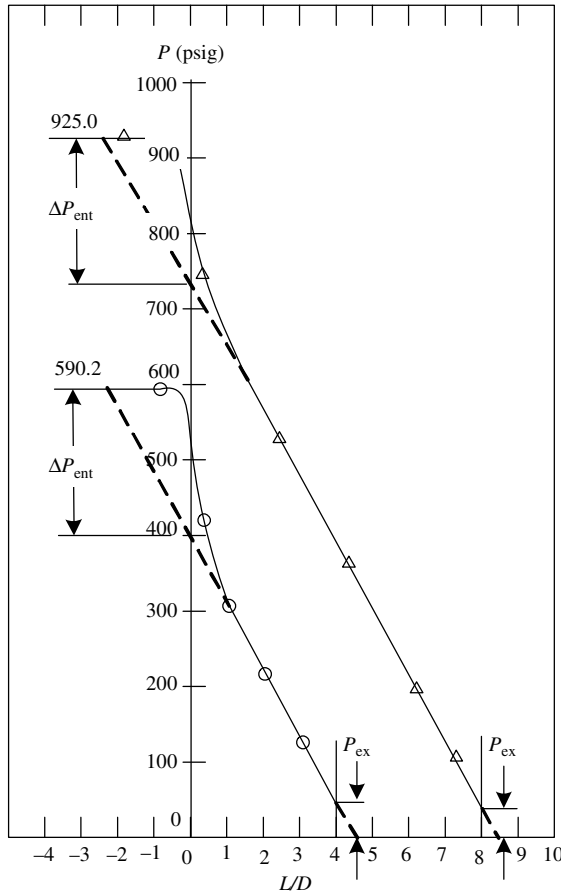
12.3 ***Newtonian and Power Law Fluids Extrudates***   A Newtonian and a Power Law model fluid are extruded from a long horizontal pipe of diameter D_0. Show that in the absence of gravity, the ratio of the extrudate diameter D to the tube diameter is given by 0.87 and $[(2n + 1)/(3n + 1)]^{1/2}$ for the Newtonian and Power Law model, respectively.

12.4 ***Estimation Extrudate Swell of a Polymer***   Tenite 800 LDPE is extruded from a long horizontal pipe of diameter D_0. Using Eqs. 12.2-1 and 12.2-2 and the

11. C. D. Han, "On Silt and Capillary-Die Rheometry," *Trans. Soc. Rheol.*, **18**, 163 (1974).

rheological data on Fig. 3.10, calculate the extrudate swell as a function of shear rate at the wall at 160° and 200°C.

12.5 ***Maximum Flow-Rater Production of Flat Sheets*** Calculate the maximum flow rate per unit width, q_{max}, for producing a smooth fracture-free sheet with a die of 0.05-cm opening for HDPE – Alathon 7040, LDPE – Alathon 1540 at 473 K; PS – Dylene 8, ABS and HIPS at 483 K. Use the Power Law model and the rheological constants below. q_{max} has to be such that $\tau_w \leq \tau_{crit} \approx 10^5 \, \text{N/m}^2$.

Polymers	T (K)	m (N·s^n/m^2)	n
HDPE–Alathon 7040	473	4.68×10^3	0.59
LDPE–Alathon 1540	473	4.31×10^3	0.47
PS–Dylene 8	483	2.83×10^4	0.25
ABS	483	3.93×10^4	0.25
HIPS	483	3.61×10^4	0.19

12.6 ***Die for Extruding a Square Extrudate*** (a) Explain why a die with a square cross section cannot produce an extruded product with a square cross section. (b) What cross section should the die have to produce a square-shaped product?

12.7 ***Design Graphs for Dies of Various Shapes, but the Same Cross-Sectional Area*** (a) Use Eqs. 12.6-1 and 12.6-2 and Fig. E5.1(a) to construct Q vs. ΔP graphs for dies that have the same cross-sectional area and the following shapes: circle, ellipse, rectangle, and a rectangle with two rounded-off sides in the shape of half-circles. Use a Newtonian fluid. (b) How can the equivalent Newtonian fluid concept help you extend these shapes for non-Newtonian fluids?

12.8 ***Design of Profile Extrusion Dies***[12] In designing a die for extruding a product that has thick and thin sections, we must secure equal extrudate velocities in both the thin and thick sections. The design in the accompanying figure shows schematically a die with one thin and one thick section. (a) Show that for such a product design A is not appropriate. (b) Calculate the lengths L_1 and L_2 (for given H_1 and H_2) in design B, which give uniform extrudate velocity at equal entrance pressure. (c) Descuss design C, and prove that if the mandrel can move axially, this die can accommodate, in principle, any polymer melt of different rheological properties.


(a)   (b)   (c)
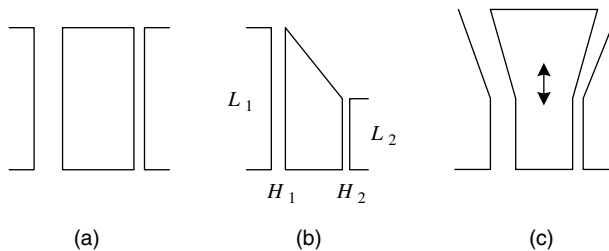
12.9 ***Wire Coating Die*** A wire coating-die, with the wire velocity of V and annular thickness of H, results in a coating thickness h at a given pressure drop. Develop an

12. F. N. Cogswell, "The Scientific Design of Fabrication Processes; Blow Molding," *Plast. Polym.*, October, (1971).

isothermal Newtonian model for calculating the coating thickness for a given pressure drop.

12.10 ***Wire-Coating Pressure Dies: The Lubrication Approximation***   An example of the wire coating pressure die is shown on Fig. 12.46. Past the guider tip the die contracts with a small taper. Consider a cross section of this region to be formed by two nonparallel plates of spacing $H(z)$, that is, disregard the curvature. The bottom plate is moving with the wire velocity V. (a) Use the lubrication approximation to obtain an expression for dP/dz. (b) Does this result support, qualitatively, the velocity field obtained by Tanner shown in the accompanying figure.


(a)

(b)
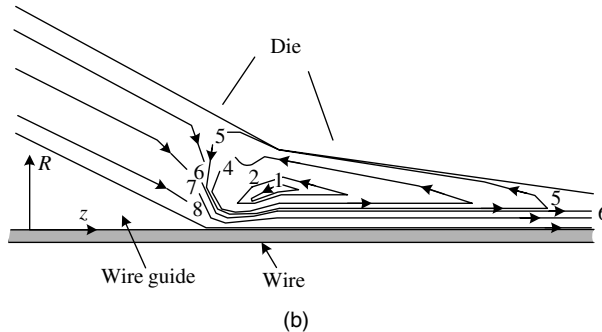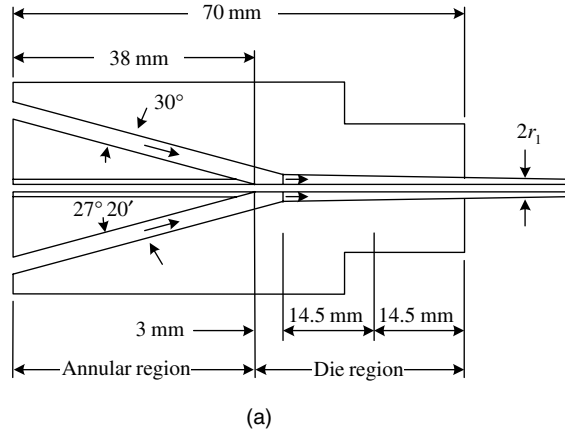
12.11 ***Coextrusion of Flat Sheets***[13]   A sheet die is fed by two extruders that deliver two polymer melts at the same temperature, but each having Power Law constants m_1, n_1 and m_2, n_2. Fluid 1 is the more viscous of the two. The two streams meet in the channel approach region of the die. That is, the die has separate manifolds and restrictors for each of the melts, but a common approach and die-lip region. Let the more viscous fluid occupy the region $0 \leq y \leq K$, where $K < H/2$, the half-thickness. Following a solution approach similar to that of Section 12.3 for evaluating the position of the maximum in the velocity profile, obtain expressions for the velocity profile if the fluids are HDPE–Alathon 7040 and PP–E612 flowing at 210°C (see Appendix A).

---

13. C. D. Han, "On Silt and Capillary-Die Rheometry," *Trans. Soc. Rheol.*, **18**, 163 (1974).

12.12 ***Wire-Coating Coextrusion Die Flow*** In the wire-coating coextrusion process two different polymer melts are brought together into a cross-head block that guides the two melts to flow in a concentric annular manner over a fast-moving wire. Consider the steady and isothermal combined drag and pressure annular flow of two Power Law melts A and B depicted in the accompanying figure, where the velocity maximum occurs in melt A. Following the methodology developed by Han and Rao[14] in Section 12.3, develop the expressions that specify the velocity profiles in both melts and the radial position of the interface, if the magnitudes of the respective volumetric flow rates of the two melts are known.
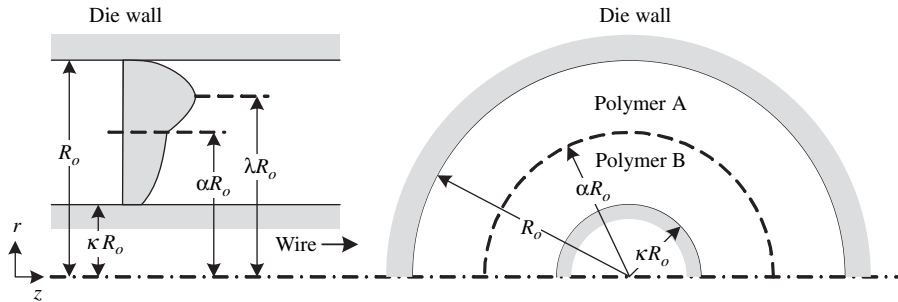
12.13 ***Blown-Film Coextrusion Die Flow*** Consider the stratified concentric steady and isothermal flow of three Power Law melts A, B, and C in the region $0 \leq Z \leq L$ in the accompanying figure. Following Han[15] methodology, formulate the expressions for obtaining the velocity profiles across all three melts, for known values of the three flow rates.
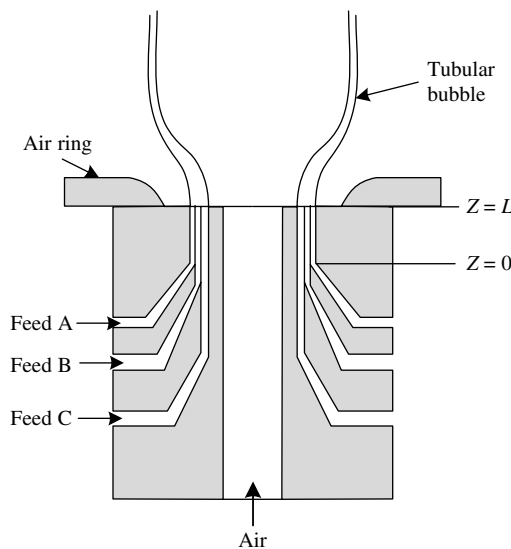

14. C. D. Han, Multiphase Flow in Polymer Processing, Academic Press, New York, 1981, Chapter 7; also, C. D. Han and D. A. Rao, "Studies on Wire coating Extrusion. II. The Rheology of Wire Coating Coextrusion," *Polym. Eng. Sci.* **20**, 128 (1980).

15. C. D. Han, "Multiphase Flow in Polymer Processing," Academic Press, New York, 1981, Chapter 7.

12.14 *Effect of the Power Law Index on the Coat-Hanger Die Design* Utilizing the coat-hanger die design equation for Power Law fluids, developed in Section 12.3, examine whether the design arrived at for the hypothetical $n = 0.5$ polymer melt in Example 12.3 will produce a uniform sheet with the following two polymers: HIPS LX-2400 (ex-Monsanto) m ($T = 443\,\text{K}$) $= 7.6 \times 10^4$ ($\text{N}\cdot\text{s}^n/\text{m}^2$) and $n = 0.20$, and for Nylon Capron TM 8200 (Ex-Allied Chemical Corp.) m ($T = 503\,\text{K}$) $= 1.95 \times 10^3$ ($\text{N}\cdot\text{s}^n/\text{m}^2$) and $n = 0.66$. If not, what design(s) will give a uniform sheet from an $H = 0.05$-cm slit opening?

12.15 *Pressure Drop Estimation in Spiral Dies*[16] Consider a spiral mandrel die similar to the one shown on Fig. 12.43. You are asked to develop a mathematical model for calculating the pressure drop flow rate relationship needed to pump a polymer melt of known rheological properties (represented, for example, by Power Law constants m and n). Neglect any "coupling" between the helical flow inside the grooves and axial flow between the flat cylindrical surfaces. Also neglect the taper between the cylindrical surfaces. Express your results in terms of m, n, Q, number and size of the ports and helical grooves, their helical angle, as well as the cylindrical surface spacing and overall length. Make use of Fig. E5.1(a).

12.16 *Flow in the Parison Die Exit Region* The flow in the diverging exit region of a parison die, shown in the accompanying figure, cannot be easily simulated, both because of the geometrical complexities involved and because the melt response is not known for such nonviscometric flow. Consider the die exit flow as the superposition of annular pressure flow in the z direction and planar extensional flow with stretching in the θ direction. Set up the appropriate equations to hold for small axial increments Δz.
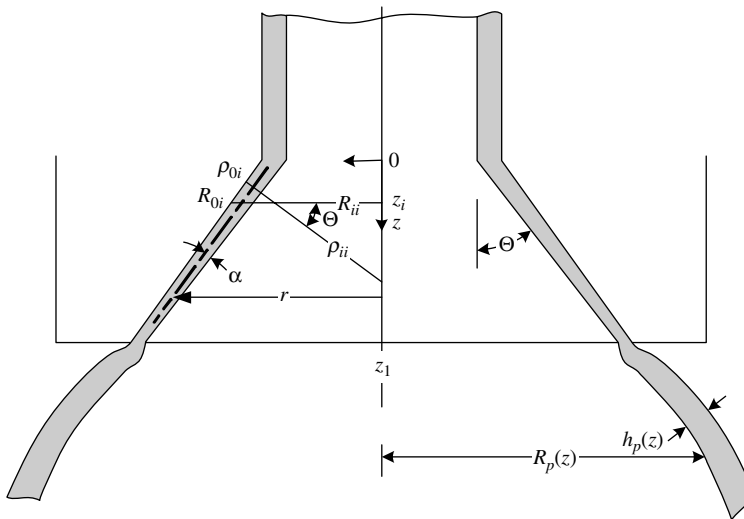
16. B. Proctor, "Flow Analysis in Extrusion Dies," *Soc. Plast. Eng. J.*, **28** (1972).

12.17 ***Estimation of Entrance Pressure–Pressure Losses from the Entrance Flow Field***[17]   Consider the entrance flow pattern observed with polymer melts and solutions in Fig. 12.16(a). The flow can be modeled, for small values of α, as follows: for $|\theta| \leq \alpha/2$ the fluid is flowing in simple extensional flow and for $\alpha/2 \leq |\theta| \leq \pi/2$ the flow is that between two coaxial cylinders of which the inner is moving with axial velocity V. The flow in the outer region is a combined drag–pressure flow and, since it is circulatory, the net flow rate is equal to 0. The velocity V can be calculated at any upstream location knowing α and the capillary flow rate. Use this model for the entrance flow field to get an estimate for the entrance pressure drop.

17. A. E. Everage, Jr., and R. L. Ballman, "An Energy Interpretaion of the flow Patterns in Extrusion through a Die Entry Region," paper presented at the 47th Annual Meeting of the Society of Rheology, New York, 1977.